

EXPERIMENTAL AND ANALYTICAL STUDY OF TWO-PHASE PRESSURE DROPS DURING EVAPORATION IN HORIZONTAL TUBES

THÈSE N° 3337 (2005)

PRÉSENTÉE À LA FACULTÉ SCIENCES ET TECHNIQUES DE L'INGÉNIEUR

Institut des sciences de l'énergie

SECTION DE GÉNIE MÉCANIQUE

ÉCOLE POLYTECHNIQUE FÉDÉRALE DE LAUSANNE

POUR L'OBTENTION DU GRADE DE DOCTEUR ÈS SCIENCES

PAR

Jesus MORENO QUIBEN

DEA - Dynamique des Fluides et des Transferts, Université Pierre et Marie Curie, Paris, France
et de nationalité espagnole

acceptée sur proposition du jury:

Prof. J. Thome, directeur de thèse
Prof. J. Corberan Salvador, rapporteur
Prof. D. Favrat, rapporteur
Prof. P. von Rohr, rapporteur

Lausanne, EPFL
2005

Acknowledgements

This study has been carried out at the Laboratory of Heat and Mass Transfer (LTCM), Swiss Federal Institute of Technology Lausanne (EPFL), under the direction of Prof. John R. Thome. The project has been supported financially by the Fond National Swiss (FNS) contract number 21-57210.99 and by the Air-Conditioning and Refrigeration Technology Institute (ARTI) contract number 605-20040, which are gratefully acknowledged.

I would like to thank Prof. John R. Thome for his advice and for giving me the opportunity and motivation to undertake this work. He was all the time available for fruitful research discussions and his guidance and encouragement during this period were a beneficial contribution to this study. Finally, I appreciate his total confidence and the responsibility granted me throughout this period.

I thank Prof. Daniel Favrat of the Laboratory of Industrial Energy Systems, Swiss Federal Institute of Technology Lausanne (EPFL), Prof. Philipp Rudolf von Rohr of the Laboratory for Transport Processes and Reactions, Swiss Federal Institute of Technology Zürich (ETH) and Prof. José Miguel Corberán of the Institute for Energy Engineering, Universidad Politécnica de Valencia (UPV) for being the examiners of this thesis.

Special thanks to my colleagues of the LTCM for their cooperation and friendship. Among them, my special gratitude to Dr. Leszek Wojtan for his constant helpfulness and productive collaboration.

I also acknowledge our technicians Laurent Chevalley and Alfred Thomas who have skillfully participated to the construction and maintenance of the experimental facility.

Finally, many thanks to Valeria and Soledad for being comprehensive in the time involved in this work.

Abstract

Two-phase flow of gases and liquids or vapors and liquids in pipes, channels, equipment, etc. is frequently encountered in industry and has been studied intensively for many years. The reliable prediction of pressure drop in two-phase flow is thereby an important aim. Because of the complexity of these types of flow, empirical or semiempirical relationships are only of limited reliability and pressure drops predicted using leading methods may differ by up to 100%. In order to improve prediction methods, this work presents an experimental and analytical investigation of two-phase pressure drops during evaporation in horizontal tubes. The goal of the experimental part was to obtain accurate two-phase pressure drop values over a wide range of experimental conditions. The existing LTCM intube refrigerant test loop has been modified and adapted to the new test conditions and measurement methods. Two new test sections have been also implemented into the modified test rig. The new test section consists of two zones: diabatic and adiabatic. This configuration allows tests to be run that obtain experimental two-phase pressure drop values under diabatic and adiabatic conditions simultaneously. The experimental campaign acquired 2543 experimental two-phase pressure drop values. Based on a comprehensive state-of-the-art review and comparison with two-phase frictional pressure drop prediction methods, it is proven that none of these methods were able to accurately, reliably predict the present experimental values. In the second part of this work, an analytical study was undertaken in order to develop a new two-phase frictional prediction method. It has been shown in the literature that the so called "phenomenological approach" tends to provide more accurate and realistic predictions as the interfacial structure between the phases is taken into account. Based on that, a phenomenological flow pattern approach was chosen in the present study. The recent Wojtan-Ursenbacher-Thome [155] map was chosen to provide the corresponding interfacial structure. The new model treats each flow regime (i.e. interfacial structure) separately and then ensures a smooth transition in between, being in agreement with the experimental observations. Another important feature of the proposed model is that it matches the correct limits at $x = 0$ (single-phase liquid flow) and $x = 1$ (single-phase gas flow). Based on a statistically comparison, it is concluded that the new two-phase frictional pressure drop model based on flow pattern map successfully predicts the new experimental data. The present work completes the fourth basic step in LTCM's flow pattern based work on two-phase flow and heat transfer inside horizontal round tubes: (i) generalized flow pattern map, (ii) flow boiling heat transfer model, (iii) convective condensation model and (iv) two-phase frictional pressure drop model.

Résumé

Les écoulements biphasiques liquide/gaz ou liquide/vapeur en tubes, canaux ou dans différentes géométries sont un problème fréquemment rencontré dans les applications industrielles et ont été largement étudiés ces dernières années. De par leur importance pratique, la prédiction des pertes de charges des écoulements biphasiques doit être précise. La complexité de ces types d'écoulements fait que les relations empiriques ou semi-empiriques usuelles sont peu précises et leurs prédictions peuvent différer parfois de 100%. Ce travail présente une investigation expérimentale et analytique des pertes de charges biphasiques durant l'évaporation en tubes horizontaux en vue d'en améliorer les méthodes de prédiction. La campagne expérimentale a permis d'obtenir une base de données élargie et fiable de pertes de charges biphasiques. Une boucle de test existante au LTCM pour l'étude des réfrigérants dans des tubes a été modifiée et adaptée aux nouvelles conditions de test et méthodes de mesures. Deux nouvelles sections de tests ont été implantées dans la boucle modifiée. Elles sont composées de deux zones : l'une adiabatique et l'autre non adiabatique. Cette configuration permet d'étudier simultanément les pertes de charges biphasiques en zone adiabatique et en zone non adiabatique. La campagne expérimentale a permis d'obtenir 2543 valeurs de pertes de charges biphasiques. Une étude bibliographique approfondie et une comparaison avec différentes méthodes de prédiction de pertes de charges biphasiques ont montré qu'aucune de ces méthodes ne permettait une prédiction précise et fiable des ces résultats expérimentaux. Dans la seconde partie de ce travail, une étude analytique a été réalisée afin de développer une nouvelle méthode de prédiction des pertes de charges biphasiques par frottement. Une approche phénoménologique a été adoptée dans cette étude car il a été démontré dans la littérature qu'elle permet des prédictions plus réalistes et plus précises en prenant en compte la structure de l'interface entre les phases. Cette structure de l'interface entre les phases a été obtenue en se basant sur la carte d'écoulement de Wojtan-Ursenbacher-Thome [155]. Ainsi le nouveau modèle traite chaque type d'écoulement séparément et assure également des transitions correctes, en accord avec les observations expérimentales. Une autre innovation importante de ce nouveau modèle est qu'il prend correctement en compte les deux limites à $x = 0$ (écoulement monophasique liquide) et $x = 1$ (écoulement monophasique gazeux). Une étude statistique a permis de conclure que ce nouveau modèle basé sur les cartes d'écoulements prédit avec succès les résultats expérimentaux. Ainsi cette étude complète la démarche en 4 étapes du LTCM concernant les écoulements biphasiques et les transferts de chaleur internes dans des tubes horizontaux circulaires: (i) carte d'écoulement non adiabatique généralisée, (ii) modèle de transfert de chaleur en ébullition, (iii) modèle de transfert de chaleur en condensation et (iv) modèle de pertes de charges biphasiques.

Contents

Acknowledgements	3
Abstract	5
Résumé	7
1 Introduction	19
2 Fundamental Definitions in Two-Phase Flow	21
2.1 Two-phase flow	21
2.2 Vapor quality	21
2.3 Void fraction	22
2.4 Velocities	23
2.5 Definition of non-dimensional numbers	24
2.6 Basic equations of two-phase flow	27
2.6.1 Conservation of mass	28
2.6.2 Conservation of momentum	29
2.6.3 Conservation of energy	31
3 Overview of Flow Pattern Maps	35
3.1 Flow patterns in horizontal flow	35
3.2 Flow pattern maps in horizontal flow	37
3.2.1 Baker flow pattern map	37
3.2.2 Mandhane et al. flow pattern map	38
3.2.3 Taitel and Dukler flow pattern map	39
3.2.4 Hashizume flow pattern map	41
3.2.5 Kattan-Thome-Favrat flow pattern map	42

3.2.6	Thome and El Hajal flow pattern map	46
3.2.7	Wojtan-Ursenbacher-Thome flow pattern map	48
3.3	Conclusions	51
4	Two-Phase Pressure Drop Models	53
4.1	Two-phase pressure drops	53
4.2	Empirical methods	54
4.2.1	Lockhart-Martinelli [90]	54
4.2.2	Bankoff [9]	56
4.2.3	Cicchitti et al. [34]	57
4.2.4	Thom [129]	57
4.2.5	Pierre [107]	57
4.2.6	Baroczy [11]	59
4.2.7	Chawla [27]	59
4.2.8	Chisholm [31]	62
4.2.9	Friedel [46]	64
4.2.10	Grønnerud [53]	65
4.2.11	Müller-Steinhagen and Heck [97]	66
4.3	Analytical methods	66
4.4	Phenomenological methods	67
4.4.1	Bandel [8]	67
4.4.2	Beattie and Whalley [14]	67
4.4.3	Hashizume et al. [61]	68
4.4.4	Olujić [104]	70
4.4.5	ARS Model [58]	73
4.5	Conclusions	74
5	Description of Experimental Test Facility	75
5.1	General description	75
5.2	Refrigerant circuit	76
5.3	Hot water circuit	78
5.4	Test sections	78
5.5	Experimental procedure and data acquisition	80

<i>CONTENTS</i>	11
5.6 Measurements	80
5.6.1 Pressure drop	80
5.6.2 Refrigerant temperature	81
5.6.3 Heat Flux	81
5.6.4 Vapor quality	81
5.7 Accuracy of measurements	82
5.7.1 Pressure drop measurement accuracy	82
5.7.2 Heat flux measurement accuracy	82
5.7.3 Vapor quality measurement accuracy	83
5.8 Conclusions	83
6 Experimental Results	85
6.1 Reduction of experimental data	85
6.2 Two-phase pressure drop measurements	89
6.2.1 Some comparisons for different experimental parameters	89
6.2.2 Results for R134a	92
6.2.3 Result for R22	93
6.2.4 Result for R410A	99
6.3 Conclusions	107
7 New Two-Phase Frictional Pressure Drop Model Based on Flow Pattern Map	109
7.1 Comparison to existing methods	109
7.2 New two-phase pressure drop model	116
7.2.1 Introduction	116
7.2.2 Segregation of experimental data	116
7.2.3 Model development	119
7.2.4 Comparisons of experimental to predicted values	125
7.3 Conclusions	135
8 Conclusions	137
A Fluid Physical Properties	139
B Liquid-Vapor Interfaces	141

Bibliography **142**

Nomenclature **155**

Curriculum Vitae **159**

List of Figures

2.1	Cross-sectional void fraction (ϵ).	22
2.2	Idealized model for multiphase-flow in an inclined channel.	28
3.1	Two-phase flow patterns in horizontal flow.	36
3.2	Flow patterns during evaporation in a horizontal tube ([35]).	37
3.3	Baker (1954) flow pattern map for horizontal flow in a tube.	38
3.4	Mandhane (1974) flow pattern map for horizontal flow in a tube.	39
3.5	Taitel and Dukler (1976) flow pattern map for horizontal flow in a tube.	40
3.6	Hashizume (1983) flow pattern map for horizontal flow in a tube.	42
3.7	Kattan (1998) flow pattern map (solid lines) evaluated for refrigerant R-410A at $T_{sat} = 5^{\circ}C$ in 13.84 mm internal diameter tube.	43
3.8	Cross-sectional and peripheral fractions in a circular tube.	45
3.9	Stratified angle in two-phase flow.	47
3.10	Thome-El Hajal (2002) flow pattern map or refrigerant R-22 at $T_{sat} = 5^{\circ}C$ and $q_{flux} = 7.5 kW/m^2$ in 13.84 mm internal diameter tube.	48
3.11	Flow pattern map for R-22 at $T_{sat} = 5^{\circ}C$ in a 13.84 mm internal diameter tube at $G = 100 kg/m^2s$ and $q = 2.1 kW/m^2$.	49
4.1	Lockhart-Martinelli correlation.	55
4.2	Multipliers r_2 , r_3 , and r_4 for boiling flow of water and steam (Thom 1964).	58
4.3	Two-phase frictional pressure drop correlation (Baroczy 1965).	60
4.4	Mass velocity correction vs property index (Baroczy 1965).	61
4.5	Linear interpolation for transient flow (Hashizume 1985).	71
4.6	Schematic representation of gas-liquid flow with a small liquid holdup ϵ_L in straight smooth tubes (ARS 1989).	73
5.1	Overall view of the modified test facility including the new two-zone test section.	76

5.2	Schematic of the refrigerant circuit.	77
5.3	Schematic of the hot water circuit ([75]).	78
5.4	New two-zone test section.	79
6.1	Total, frictional and momentum pressure drops vs. vapor quality at different experimental conditions ($d = 13.8\text{ mm}$).	87
6.2	Total, frictional and momentum pressure drops vs. vapor quality at different experimental conditions ($d = 8\text{ mm}$).	88
6.3	Adiabatic vs. diabatic test section results for R410A.	89
6.4	Frictional pressure gradients vs. vapor quality for R22 and R410A.	90
6.5	Comparison of the frictional pressure gradients for R134a,R22 and R410A at two set of experimental conditions.	90
6.6	Frictional pressure gradients vs. vapor quality for different mass velocities.	91
6.7	Frictional pressure gradients vs. vapor quality at different heat fluxes.	91
6.8	Frictional pressure gradients vs. vapor quality for R134a at different experimental conditions ($d = 13.8\text{ mm}$).	92
6.9	Frictional pressure gradients vs. vapor quality for R22 at different experimental conditions ($d = 13.8\text{ mm}$) – (I).	93
6.10	Frictional pressure gradients vs. vapor quality for R22 at different experimental conditions ($d = 13.8\text{ mm}$) – (II).	94
6.11	Frictional pressure gradients vs. vapor quality for R22 at different experimental conditions ($d = 13.8\text{ mm}$) – (III).	95
6.12	Frictional pressure gradients vs. vapor quality for R22 at different experimental conditions ($d = 13.8\text{ mm}$) – (IV).	96
6.13	Frictional pressure gradients vs. vapor quality for R22 at different experimental conditions ($d = 8\text{ mm}$) – (I).	97
6.14	Frictional pressure gradients vs. vapor quality for R22 at different experimental conditions ($d = 8\text{ mm}$) – (II).	98
6.15	Frictional pressure gradients vs. vapor quality for R410A at different experimental conditions ($d = 13.8\text{ mm}$) – (I).	99
6.16	Frictional pressure gradients vs. vapor quality for R410A at different experimental conditions ($d = 13.8\text{ mm}$) – (II).	100
6.17	Frictional pressure gradients vs. vapor quality for R410A at different experimental conditions ($d = 13.8\text{ mm}$) – (III).	101
6.18	Frictional pressure gradients vs. vapor quality for R410A at different experimental conditions ($d = 13.8\text{ mm}$) – (IV).	102
6.19	Frictional pressure gradients vs. vapor quality for R410A at different experimental conditions ($d = 8\text{ mm}$) – (I).	103

6.20	Frictional pressure gradients vs. vapor quality for R410A at different experimental conditions ($d = 8\text{ mm}$) – (II).	104
6.21	Frictional pressure gradients vs. vapor quality for R410A at different experimental conditions ($d = 8\text{ mm}$) – (III).	105
6.22	Frictional pressure gradients vs. vapor quality for R410A at different experimental conditions ($d = 8\text{ mm}$) – (IV).	106
7.1	Frictional pressure gradients vs. three prediction methods for R22 at different experimental conditions.	111
7.2	Frictional pressure gradients vs. three prediction methods for R410A at different experimental conditions.	112
7.3	Comparisons of experimental to predicted values using Friedel correlation for the entire database: a) 67.33% are predicted within $\pm 30\%$, b) 51.81% are predicted within $\pm 20\%$.	113
7.4	Comparisons of experimental to predicted values using Grönnerud correlation for the entire database: a) 46.15% are predicted within $\pm 30\%$, b) 40.45% are predicted within $\pm 20\%$.	114
7.5	Comparisons of experimental to predicted values using Müller-Steinhagen and Heck correlation for the entire database: a) 75.79% are predicted within $\pm 30\%$, b) 49.64% are predicted within $\pm 20\%$.	115
7.6	Flow pattern maps for R-22, $T_{sat} = 5^\circ\text{C}$, $D = 13.84\text{ mm}$ at $G = 300\text{ kg/m}^2\text{s}$ and heat fluxes: a) 7.5 kW/m^2 , b) 17.5 kW/m^2 , c) 37.5 kW/m^2 , d) 57.5 kW/m^2 .	117
7.7	Flow pattern maps for R-410A, $T_{sat} = 5^\circ\text{C}$, $D = 8.00\text{ mm}$ at $G = 400\text{ kg/m}^2\text{s}$ and initial heat fluxes: a) 37.5 kW/m^2 , b) 57.5 kW/m^2 .	117
7.8	Flow pattern maps for R-410A, $T_{sat} = 5^\circ\text{C}$, $D = 13.84\text{ mm}$ at $G = 300\text{ kg/m}^2\text{s}$ and initial heat fluxes: a) 7.5 kW/m^2 , b) 17.5 kW/m^2 , c) 37.5 kW/m^2 , d) 57.5 kW/m^2 .	118
7.9	Simplified annular flow configuration.	119
7.10	Simplified stratified flow configuration.	121
7.11	Dryout zone during evaporation in horizontal tube.	123
7.12	Comparisons of experimental to predicted values for the entire database: a) 82.30% are predicted within $\pm 30\%$, b) 64.71% are predicted within $\pm 20\%$.	126
7.13	Comparisons of experimental to predicted values for R22 and both tested diameters: a) 82.67% are predicted within $\pm 30\%$, b) 60.26% are predicted within $\pm 20\%$.	127
7.14	Comparisons of experimental to predicted values for R410A and both tested diameters: a) 83.02% are predicted within $\pm 30\%$, b) 69.46% are predicted within $\pm 20\%$.	127
7.15	Comparisons of experimental to predicted values for $d = 8\text{ mm}$ and both tested fluids: a) 82.06% are predicted within $\pm 30\%$, b) 67.64% are predicted within $\pm 20\%$.	128

7.16	Comparisons of experimental to predicted values for $d = 13\text{ mm}$ and both tested diameters: a) 82.24% are predicted within $\pm 30\%$, b) 62.86% are predicted within $\pm 20\%$	128
7.17	Comparisons of experimental to predicted values for the entire database segregated by flow regime: a) annular, b) Slug+Intermittent, c) SW, d) Slug+SW.	129
7.18	Experimental and predicted values vs. vapor quality for R134a at different experimental conditions.	130
7.19	Experimental and predicted values vs. vapor quality for R22 at different experimental conditions and $d = 13.8\text{ mm}$	131
7.20	Experimental and predicted values vs. vapor quality for R22 at different experimental conditions and $d = 8\text{ mm}$	132
7.21	Experimental and predicted values vs. vapor quality for R410A at different experimental conditions and $d = 13.8\text{ mm}$	133
7.22	Experimental and predicted values vs. vapor quality for R410A at different experimental conditions and $d = 8\text{ mm}$	134
B.1	Perturbed vapor-liquid interface.	141

List of Tables

4.1	Values of C to fit the empirical curves of Lockhart and Martinelli.	56
5.1	Experimental conditions for in-tube evaporation tests.	75
5.2	Main properties and geometrical dimensions of the implemented test sections.	79
7.1	Segregated experimental values by flow regime using Wojtan et al. flow pattern map, where S = stratified flow, SW = stratified-wavy flow, I = intermittent flow, A = annular flow, M = mist flow and D represents the transition zone between annular and mist flow.	118
7.2	Compilation of percentages of the database within an specific range for the new proposed model and three existing methods.	125
A.1	Physical properties for fluids used during the experimental campaign at three different saturation temperatures.	139

Chapter 1

Introduction

Liquid-vapor phase-change processes play a very important role in many technological applications. The virtually isothermal heat transfer associated with boiling and condensation processes makes their inclusion in power and refrigeration cycles very advantageous from a thermodynamic efficiency viewpoint. In addition boiling and condensation can achieve large heat transfer rates with small temperatures differences. Processes associated with phase-change phenomena are among the most complex transport processes encountered in engineering applications. These processes include all the complexity of single-phase convective transport (non-linearities, transition to turbulence, instabilities) and additional elements resulting from the motion of the vapor-liquid interface, non-equilibrium effects and interactions between the phases.

Two-phase flow of gases and liquids or vapors and liquids in pipes, channels, equipment, etc. is frequently encountered in industry and has been studied intensively for many years. The reliable prediction of pressure drop in two-phase flows is thereby an important aim. Because of the complexity mentioned above, empirical or semiempirical relationships are only of limited applicability. Yet, pressure drops predicted using leading methods differ by up to 100% according to Ould Didi, Kattan and Thome [105] and Moreno Quibén and Thome [93]. Hence, increasingly, attempts are being made to develop prediction methods which are based on physical models and which can be correlated with the measured results. The mathematical content is kept as small as possible in order to keep the application practical.

Kattan, Thome and Favrat [76, 77, 78] proposed a new physically based (based on a simplified interfacial two-phase structure) flow pattern oriented model to predict heat transfer coefficients during evaporation in horizontal tubes. The new heat transfer model was a significant step ahead, improving significantly the predictive accuracy. In addition, in the previously mentioned study by Ould Didi et al. it is shown that classifying the flow by local flow pattern and then using the best two-phase pressure drop prediction method for that particular flow pattern results in a significant improvement in accuracy.

Based on that, the idea is to extend this physically based approach to the development of a two-phase pressure drop prediction method. Hence, in order to develop this approach an experimental and analytical study was undertaken. The main experimental objectives of this study are to: (i) accurately and reliably measure two-phase pressure drops over a wide range of experimental conditions and (ii) be able to obtain experimental two-phase pressure drop values in the different flow regimes by a consequent design of the test sections. The analytical objective of this study is then the development of a flow pattern based pressure drop model that respects the two-phase flow

structure of the various flow regimes as much as possible while maintaining a degree of simplicity.

The present work will complete the fourth basic step in LTCM's flow pattern based work on two-phase flow and heat transfer inside horizontal round tubes: (i) generalized flow pattern map, (ii) flow boiling heat transfer model (iii) convective condensation model and (iv) two-phase frictional pressure drop model.

The expected result from this project is a much better two-phase pressure drop prediction method and therefore a more accurate design method that better simulates experimental trends and the effects of the principal variables on the process.

The manuscript is organized as follows:

- Chapter 1 - Introduction: Background and purpose of the present study.
- Chapter 2 - Fundamentals: Definition of the main variables and basic equations used in two-phase flow and two-phase pressure drop analysis.
- Chapter 3 - Overview of flow pattern maps: Presentation of the state-of-the-art of existing flow pattern maps.
- Chapter 4 - Two-phase pressure drop models: State-of-the-art of two-phase pressure drop models.
- Chapter 5 - Description of experiments: Test facility and data collection methods are described.
- Chapter 6 - Experimental results: Results of the two-phase pressure drop measurements are presented and analyzed.
- Chapter 7 - New two-phase pressure drop flow pattern based model: Presentation of a new flow pattern based, two-phase frictional pressure drop model.
- Chapter 8 - Conclusions: General conclusions of this present study are summarized.

Chapter 2

Fundamental Definitions in Two-Phase Flow

This chapter introduces the primary variables used throughout this work and derives some simple relationships between them for the case of one-dimensional flow. To distinguish between gas and liquid the subscripts ' L ' for liquid and ' G ' for vapor will be used. Basic equations for two-phase flows are also introduced at the end of the chapter.

2.1 Two-phase flow

Classical thermodynamics tell us that a phase is a macroscopic state of matter which is homogeneous in chemical composition and physical structure; e.g. a gas, a liquid or solid of a pure component. Two-phase flow is the simplest case of multiphase flow in which two phases are present for a pure component.

In internal convective vaporization and condensation processes, the vapor and liquid are in simultaneous motion inside the pipe. The resulting two-phase flow is generally more complicated physically than single-flow. In addition to the usual inertia, viscous, and pressure forces present in single-phase flow, two-phase flows are also affected by interfacial tension forces, the wetting characteristics of the liquid on the tube wall, and the exchange of momentum between the liquid and vapor phases in the flow.

2.2 Vapor quality

The vapor quality (x) is defined to be the ratio of the vapor mass flow rate (\dot{M}_G [$kg\ s^{-1}$]) divided by the total mass flow rate ($\dot{M}_G + \dot{M}_L$):

$$x = \frac{\dot{M}_G}{\dot{M}_G + \dot{M}_L} \quad (2.1)$$

When phase change does not take place in the channel, one needs to measure the mass flow rate of each phase, and the quality is then determined for the entire channel. In case there is a phase

change in the channel, e.g. if the channel is heated and boiling takes place, then the quality will increase (inverse for condensation) downstream with the flow.

Since often there is not thermal equilibrium between the phases, one cannot calculate the quality merely by knowing the inlet quality and the heat flux from the wall. Unfortunately, it is very difficult to measure or calculate with precision the quality of the liquid-vapor mixture flowing in a channel where a change of phase takes place. A fictitious quality, the so called thermodynamic equilibrium quality can be calculated by assuming that both phases are saturated, i.e., that their temperatures are equal to the saturation temperature corresponding to their common pressure. The so-called thermodynamic equilibrium quality can be calculated as:

$$x = \frac{h(z) - h_L}{h_{LG}} \quad (2.2)$$

where $h_L [J kg^{-1}]$ is the enthalpy of the saturated liquid, $h_{LG} [J kg^{-1}]$ is the latent heat of vaporization, and $h(z) [J kg^{-1}]$ is the enthalpy at a cross section z , which can be calculated from:

$$h(z) = h_{inlet} + \frac{1}{\dot{M}} \int_0^z q'(z) dz \quad (2.3)$$

where h_{inlet} is the enthalpy of the fluid at the inlet and $q'(z) [W m^{-1}]$ is the heat input per unit length of channel.

2.3 Void fraction

In two-phase flow, void fraction is one of the most important parameters to be defined. It defines the cross-sectional area occupied by each phase. As it determines mean velocities of the liquid and the vapor, it represents a fundamental parameter in the calculation of pressure drop, flow pattern transitions and heat transfer coefficients.

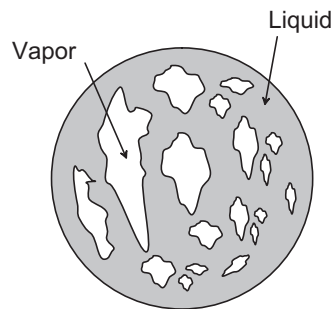


Figure 2.1: Cross-sectional void fraction (ϵ).

The void fraction of the vapor is defined as:

$$\epsilon = \frac{A_G}{A_G + A_L} \quad (2.4)$$

where A_G is the sum of areas occupied by voids and A_L is the sum of areas occupied by the liquid. The total cross-sectional area of the channel is called A .

2.4 Velocities

In two-phase flow there are a number of velocities that can be defined. Also, in general, the phases will not have the same velocity and there will be a relative velocity between them.

True average velocities

The true average velocities (also called actual velocities) of the phases u_G and u_L are the velocities by which the phases actually travel. The cross sectional average true velocities are determined by the volumetric flow rates \dot{Q}_G and \dot{Q}_L [m^3s^{-1}] of the vapor and liquid divided by the cross-sectional areas occupied by the respective phases:

$$u_G = \frac{\dot{Q}_G}{A_G} = \frac{\dot{Q}_G}{\epsilon A} \quad (2.5)$$

$$u_L = \frac{\dot{Q}_L}{A_L} = \frac{\dot{Q}_L}{(1 - \epsilon)A} \quad (2.6)$$

From the equation of continuity it is possible to define liquid and vapor true mean velocities referred to their own cross sectional areas and their own mass flow rates as follows:

$$u_G = \frac{x}{\epsilon} \frac{\dot{M}}{\rho_G A} = \frac{G}{\rho_G} \frac{x}{\epsilon} \quad (2.7)$$

$$u_L = \frac{1 - x}{1 - \epsilon} \frac{\dot{M}}{\rho_L A} = \frac{G}{\rho_L} \frac{1 - x}{1 - \epsilon} \quad (2.8)$$

Superficial velocities

The superficial velocities (also called volumetric fluxes) of the phases j_G and j_L are defined as the volumetric flow rate of the phase through the total cross-sectional area of the two-phase flow. It might also be expressed as the phase velocity if it would flow alone in the entire cross section. Thus:

$$j_G = \frac{\dot{Q}_G}{A} = \frac{G}{\rho_G} x = \epsilon u_G \quad (2.9)$$

$$j_L = \frac{\dot{Q}_L}{A} = \frac{G}{\rho_L} (1 - x) = (1 - \epsilon) u_L \quad (2.10)$$

The total superficial velocity is defined as:

$$j = j_G + j_L \quad (2.11)$$

Drift velocities

The drift velocities of the phases V_{Gj} and V_{Lj} are defined as the true average velocity of the phase in relation to the total superficial velocity, namely:

$$V_{Gj} = u_G - j \quad (2.12)$$

$$V_{Lj} = u_L - j \quad (2.13)$$

The drift fluxes of the phases j_{Gj} and j_{Lj} are defined as follows:

$$j_{Gj} = \epsilon V_{Gj} = \epsilon(u_G - j) \quad (2.14)$$

$$j_{Lj} = \epsilon V_{Lj} = (1 - \epsilon)(u_L - j) \quad (2.15)$$

It follows, from equations (2.14), (2.15) and (2.11) that:

$$j_{Gj} + j_{Lj} = 0 \quad (2.16)$$

Mass velocity

The mass velocity (G) is defined to be the ratio of the mass flow rate (\dot{M}) divided by the cross-sectional area of the flow channel:

$$G = \frac{\dot{M}}{A} \quad (2.17)$$

Considering the continuity law, the mass velocity is the expression of the mean flow velocity multiplied by the mean density. The mass velocity has units of $[kg/m^2s]$.

2.5 Definition of non-dimensional numbers

The principal non-dimensional numbers used in the present study are defined below. Different definitions of main non-dimensional numbers, particularly for the Reynolds and Froude number, can be found in the literature. In order to be coherent in this work, the corresponding used here definitions are introduced.

Reynolds number

The Reynolds number represents the ratio of the inertial forces to the viscous forces. For the particular case of forced convection inside a tubular channel, the liquid Reynolds number for a single-phase in a channel can be expressed in the following form:

$$Re_L = \frac{\rho_L u_L D_h}{\mu_L} \quad (2.18)$$

where D_h is the hydraulic diameter defined as the ratio of the cross-sectional A to the wetted perimeter P_L and is calculated as follows:

$$D_h = \frac{4A}{P_L} \quad (2.19)$$

In the particular case of circular tubes, $D_h = D$.

Considering one-dimensional flow and using the definition of the true mean velocity from equation (2.6), the liquid Reynolds number in a two-phase flow can be expressed as:

$$Re_L = \frac{GD_h}{\mu_L} \frac{1-x}{1-\epsilon} \quad (2.20)$$

where D_h for the liquid phase is expressed in the following form:

$$D_h = \frac{4A_L}{P_L} = \frac{4(1-\epsilon)A}{P_L} \quad (2.21)$$

Substituting equation (2.21) into (2.20) the liquid Reynolds number is defined as:

$$Re_L = \frac{4G(1-x)A}{\mu_L P_L} \quad (2.22)$$

The same approach will be used for the vapor Reynolds number which is defined as:

$$Re_G = \frac{GD_h}{\mu_G} \frac{x}{\epsilon} \quad (2.23)$$

where the D_h for the vapor phase is expressed as:

$$D_h = \frac{4A_G}{P_L} = \frac{4A\epsilon}{P_L} \quad (2.24)$$

Finally, substituting equation (2.24) into (2.23), the vapor Reynolds number is expressed as:

$$Re_G = \frac{4GxA}{\mu_G P_L} \quad (2.25)$$

Kattan et al. ([76],[77],[78]) and Wojtan [153] assumed that the hydraulic diameter D_h for the vapor phase is equal to the tube diameter D like in single-phase flow. As the void fraction increased very rapidly with increasing the vapor quality, this assumption seems to be reasonable. Assuming this assumption, the vapor Reynolds number, equation (2.23), can be expressed as:

$$Re_G = \frac{GD}{\mu_G} \frac{x}{\epsilon} \quad (2.26)$$

Nusselt number

The Nusselt number expresses the ratio of convective to conduction temperature gradient. In internal forced convection, the reference length is the tube diameter:

$$Nu = \frac{hD}{\lambda} \quad (2.27)$$

where h is the heat transfer coefficient, D is the tube diameter, λ is the thermal conductivity.

Liquid Froude number

The Froude number represents the ratio of the inertia forces to the gravitational forces. The general expression is:

$$Fr = \frac{u^2}{gL} \quad (2.28)$$

Wojtan [153], based on existing flow boiling correlations that use a different Froude number definition, uses the following form of the liquid Froude number:

$$Fr_L = \frac{G^2}{\rho_L g D} \quad (2.29)$$

In order to be coherent with the mentioned previous work, the same expression will be used throughout this work.

Liquid Weber number

The liquid Weber number expresses the ratio of inertia to surface tension forces. As for the Nusselt number, the reference length is the tube diameter.

It is expressed for liquid phase as:

$$We_L = \frac{\rho_L u_L^2 D}{\sigma} \quad (2.30)$$

Prandtl number

The Prandtl number is the ratio between the momentum diffusivity and the thermal diffusivity.

It is expressed for a liquid as:

$$Pr_L = \frac{c_{pL} \mu_L}{\lambda_L} \quad (2.31)$$

The same expression for a vapor is:

$$Pr_G = \frac{c_{pG}\mu_G}{\lambda_G} \quad (2.32)$$

Martinelli parameter

The Martinelli parameter [90] is defined as the ratio between the theoretical pressure gradients which would occur if either fluid were flowing alone in the pipe with the original flow rate of each phase. The Martinelli parameter X_{tt} is calculated as:

$$X_{tt}^2 = \frac{(\Delta p_F/\Delta L)_{L0}}{(\Delta p_F/\Delta L)_{G0}} \quad (2.33)$$

X_{tt}^2 is void fraction independent and is a measure of the degree to which the two-phase mixture is closer to being a liquid, i.e. $X_{tt}^2 \gg 1$, or to being a gas, i.e. $X_{tt}^2 \ll 1$. The subscript tt is sometimes used and signifies that both phases are turbulent.

Modelling the pressure drop of each phase with its superficial velocity and friction factors in the classical form:

$$f_L = C_L Re_L^{-n} \quad (2.34)$$

$$f_G = C_G Re_G^{-m} \quad (2.35)$$

and assuming the same friction model for both phases (both turbulent or both laminar) which means that $m = n$ and $C_L = C_G$, equation (2.33) reduces to:

$$X_{tt} = \left(\frac{1-x}{x}\right)^{(-n+2)/2} \left(\frac{\mu_L}{\mu_G}\right)^{n/2} \left(\frac{\rho_G}{\rho_L}\right)^{1/2} \quad (2.36)$$

Based on equation (2.34) Lockhart and Martinelli [90] and then Taitel and Dukler [126] used $n = m = 0.2$ and $C_L = C_G = 0.046$ for a smooth pipe. Steiner [137], Kattan [75] and Zürcher [162] used $n = m = 0.25$ and $C_L = C_G = 0.3146$ for a smooth pipe. In this work the same expression as Steiner, Kattan and Zürcher will be used:

$$X_{tt} = \left(\frac{1-x}{x}\right)^{0.875} \left(\frac{\mu_L}{\mu_G}\right)^{0.125} \left(\frac{\rho_G}{\rho_L}\right)^{0.5} \quad (2.37)$$

2.6 Basic equations of two-phase flow

Developments of the full governing equations for three-dimensional, time-varying two-phase flow can be found in Ishii [67], Bouré [20] and Delhaye [37]. The form of the governing equations can be simplified by invoking time and/or space averaging. The averaging processes make the equations more tractable but, at the same time, useful information about the flow is lost at each simplifying step. In the present context, for sake of simplicity, the flow is considered to be steady

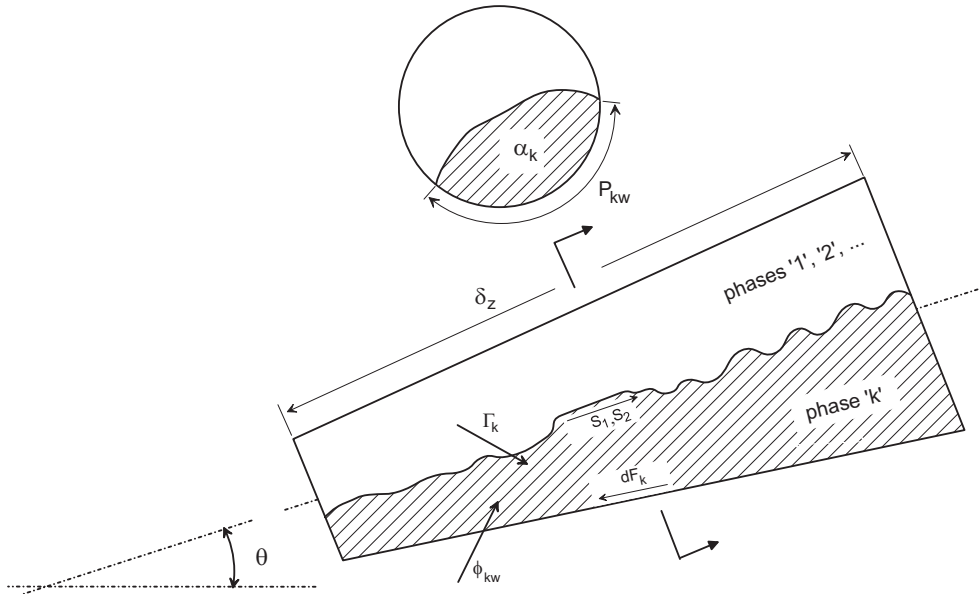


Figure 2.2: Idealized model for multiphase-flow in an inclined channel.

and one-dimensional in the sense that all dependent variables are idealized as being constant over any section of the tube, varying only in the axial direction.

To facilitate development of a one-dimensional analysis of multi-phase flow, we will consider the system shown in Fig. (2.2). A stratified flow is chosen to allow the equations to be derived for the general case where each phase is in contact with the channel wall as well as having a common interface. It is further assumed that the pressure across any phase normal to the channel is uniform. Mean values of velocity and density of each phase are assumed to exist across any phase normal to the flow.

2.6.1 Conservation of mass

The equation expressing the conservation of mass in the absence of any removal or addition of fluid through the channel walls for phase k is:

$$\frac{\partial}{\partial t}(A\epsilon_k\rho_k) + \frac{\partial}{\partial z}(A\epsilon_k\rho_k u_k) = \Gamma_k \quad (2.38)$$

where ϵ_k is the void fraction of phase k , ρ_k is the density of phase k , u_k is the true average velocity of phase k and Γ_k is the mass transfer (mass flow rate \dot{M} per unit length) to phase k from the various interphase mass transfer, where:

$$\sum_k \Gamma_k = 0 \quad (2.39)$$

For the particular case of steady state two-phase gas(G)/liquid(L) flow in a constant area channel this reduces to two expressions:

$$\begin{aligned}\frac{d}{dz}(A_G \rho_G u_G) &= \Gamma_G \\ \frac{d}{dz}(A_L \rho_L u_L) &= \Gamma_L\end{aligned}\quad (2.40)$$

and

$$\Gamma_G = -\Gamma_L = \frac{d\dot{M}_G}{dz} = -\frac{d\dot{M}_L}{dz}\quad (2.41)$$

2.6.2 Conservation of momentum

The rate of creation of momentum of phase k plus the rate of inflow of momentum is balanced against the sum of the forces acting on that phase plus the momentum generation due to mass transfer, as follows:

$$\begin{aligned}& \boxed{\frac{\partial}{\partial t}(\dot{M}_k \delta z) + \left(\dot{M}_k u_k + \delta z \frac{\partial}{\partial z}(\dot{M}_k u_k) \right) - \dot{M}_k u_k}_{1} = \\ & \boxed{\left[A \epsilon_k p - \left(A \epsilon_k p + \delta z \frac{\partial}{\partial z}(A \epsilon_k p) \right) + \left\{ p \left(-\delta z \frac{\partial}{\partial z}(A \epsilon_k) \right) \right\} \right]}_{2} - \\ & \boxed{A \epsilon_k \rho_k \delta z g \sin \theta}_{3} - \boxed{\tau_{kw} P_{kw} \delta z}_{4} + \boxed{\sum_1^n \tau_{knz} P_{kn} \delta z}_{5} + \boxed{u_k \Gamma_k}_{6}\end{aligned}\quad (2.42)$$

A brief discussion of the terms in this equation is given below:

- the terms in box 1 represent the rate of creation of momentum plus the rate of inflow of momentum within the control element.
- the terms in box 2 represent the pressure forces in the control element.
- the term in box 3 represents the gravitational forces.
- the term in box 4 represents the wall shear force (dF_k), where τ_{kw} is the wall shear stress between the phase k and the channel wall and P_{kw} is the contact perimeter between the wall and phase k .
- the term in box 5 represents the sum of the interfacial shear forces (S_1, S_2, \dots), where where τ_{knz} is the z component of the interfacial shear stress between phase k and phase n and P_{kn} is the contact perimeter between phase k and phase n .
- the term in box 6 represents the rate of generation of momentum of phase k due to mass transfer assuming that that the mass transferred across the interface is accelerated to the mean velocity of the receiving phase.

Rearranging terms, equation (2.42) can be written as:

$$-A\epsilon_k \frac{\partial p}{\partial z} - \tau_{kw} P_{kw} \delta z + \sum_1^n \tau_{knz} P_{kn} \delta z - A\epsilon_k \rho_k \delta z g \sin\theta + u_k \Gamma_k = \frac{\partial}{\partial t} (\dot{M}_k \delta z) + \delta z \frac{\partial}{\partial z} (\dot{M}_k u_k) \quad (2.43)$$

Thus for a steady-state two-phase gas(_G)/liquid(_L) flow in a constant area channel, we have for the gas phase

$$-A_G dp - \tau_{Gw} P_{Gw} dz + \tau_{GL} P_{GL} dz - A_G \rho_G dz g \sin\theta + u_G \Gamma_G = \dot{M}_G du_G \quad (2.44)$$

and for the liquid phase

$$-A_L dp - \tau_{Lw} P_{Lw} dz + \tau_{LG} P_{LG} dz - A_L \rho_L dz g \sin\theta + u_L \Gamma_L = \dot{M}_L du_L \quad (2.45)$$

Adding equations (2.44) and (2.45) and using the conservation of momentum across the interface

$$\tau_{GL} P_{GL} dz + u_G \Gamma_G = \tau_{LG} P_{LG} dz + u_L \Gamma_L \quad (2.46)$$

we obtain the following equation which represents the basic differential equation for this simplified approach

$$-A dp + \tau_{Gw} P_{Gw} dz - \tau_{Lw} P_{Lw} dz - g \sin\theta [A_L \rho_L + A_G \rho_G] = d(\dot{M}_L u_L + \dot{M}_G u_G) \quad (2.47)$$

The net frictional force acting on each phase may be expressed in terms of the ones occupied by each phase

$$(dF_G + S) = -\tau_{Gw} P_{Gw} dz - \tau_{GL} P_{GL} dz = -A_G \left(\frac{dp}{dz} F \right)_G dz \quad (2.48)$$

$$(dF_L - S) = -\tau_{Lw} P_{Lw} dz + \tau_{GL} P_{GL} dz = -A_L \left(\frac{dp}{dz} F \right)_L dz \quad (2.49)$$

Adding equations (2.48) and (2.49), we obtain the expression for the total net frictional force

$$(dF_G + dF_L) = -\tau_{Gw} P_{Gw} dz - \tau_{Lw} P_{Lw} dz = -A \left(\frac{dp}{dz} F \right) dz \quad (2.50)$$

where the term $\left(\frac{dp}{dz} F \right)$ represents the part of the overall pressure gradient required to overcome friction.

Substitution of equation (2.50) into equation (2.47) and rearrangement yields

$$\left(\frac{dp}{dz} \right) = \left(\frac{dp}{dz} F \right) + \left(\frac{dp}{dz} a \right) + \left(\frac{dp}{dz} z \right) \quad (2.51)$$

where the term $\left(\frac{dp}{dz}a\right)$ reflects the change in kinetic energy of the flow and can be expressed, using relationships introduced in this chapter, as:

$$-\left(\frac{dp}{dz}a\right) = \frac{1}{A} \frac{d}{dz} (\dot{M}_G u_G + \dot{M}_L u_L) = G^2 \frac{d}{dz} \left[\frac{x^2}{\epsilon \rho_G} + \frac{(1-x)^2}{(1-\epsilon) \rho_L} \right] \quad (2.52)$$

and the term $\left(\frac{dp}{dz}z\right)$ reflects the change in static head and can be expressed as:

$$-\left(\frac{dp}{dz}z\right) = g \sin\theta \left[\frac{A_G}{A} \rho_G + \frac{A_L}{A} \rho_L \right] = g \sin\theta [\epsilon \rho_G + (1-\epsilon) \rho_L] \quad (2.53)$$

The above derivation introduces the use of the momentum equation to relate the total pressure gradient in terms of its three separate components: friction, acceleration and static head. It should be explained at this point that the frictional component has been derived in terms of the total wall shear force ($dF_G + dF_L$).

2.6.3 Conservation of energy

The rate of increase of total energy for phase k (internal plus kinetic energy) within the control element plus the rate at which total energy is convected into the control element is balanced against the rate at which heat is added to phase k plus the rate at which work is done on phase k plus the rate at which energy is transferred across the interface to the control element. The equation expressing the differential energy balance is:

$$\begin{aligned} & \boxed{\frac{\partial}{\partial t} \left[\epsilon_k \rho_k \left(e_k + \frac{u_k^2}{2} \right) A \delta z \right] + \dot{M}_k \left(e_k + \frac{u_k^2}{2} \right) \delta z - \left[\dot{M}_k \left(e_k + \frac{u_k^2}{2} \right) - \delta z \frac{\partial}{\partial z} \dot{M}_k \left(e_k + \frac{u_k^2}{2} \right) \right]}_1 = \\ & \boxed{\phi_{kw} P_{kw} \delta z + \sum_1^n \phi_{kn} P_{kn} \delta z + \dot{\phi}_k A \epsilon_k \delta z}_2 + \boxed{\left[\frac{\dot{M}_k p}{\rho_k} - \left(\frac{\dot{M}_k p}{\rho_k} + \delta z \frac{\partial}{\partial z} \left(\frac{\dot{M}_k p}{\rho_k} \right) \right) \right]}_3 - \\ & \boxed{\dot{M}_k g \sin\theta \delta z - p A \delta z \frac{\partial \epsilon_k}{\partial t}}_4 + \boxed{\Gamma_k \frac{\delta z p}{\rho_k} + u_k \sum_1^n \tau_{kn} p_{kn} \delta z}_5 + \boxed{\Gamma_k \delta z \left(e_k + \frac{u_k^2}{2} \right)}_6 \quad (2.54) \end{aligned}$$

A brief discussion of terms in this equation is given below:

- the terms in box 1 represent the rate of increase of total energy plus the rate at which energy enters within the control element in the absence of the addition or subtraction of mass through the channel walls.
- the terms in box 2 represent the rate at which heat enters phase k within the control volume, namely: the heat flow via the channel wall over the perimeter P_{kw} , the heat flow via the various interfaces with the other n phases and the internal heat generation for phase k within the control element itself.
- the terms in box 3 represent the work done by pressure forces.

- the terms in box 4 represent the work done by body forces.
- the terms in box 5 represent the work done by shear and pressure forces at the interface with other phases.
- the term in box 6 represents the rate at which energy is added to phase k by virtue of mass transfer across the interface.

Rearranging terms, equation (2.54) may be written as:

$$\begin{aligned} \frac{\partial}{\partial t} A \epsilon_k \rho_k \left(e_k + \frac{u_k^2}{2} \right) + \frac{\partial}{\partial z} \dot{M}_k \left(i_k + \frac{u_k^2}{2} \right) = \\ - \dot{M}_k g \sin \theta + \phi_{wk} P_{wk} + \sum_1^n \phi_{kn} P_{kn} + \dot{\phi}_k A \epsilon_k - \\ p A \frac{\partial \epsilon_k}{\partial t} + \Gamma_k \left(i_k + \frac{u_k^2}{2} \right) + u_k \sum_1^n \tau_{kn} P_{kn} \end{aligned} \quad (2.55)$$

where i_k represents the enthalpy of phase k per unit of mass

$$i_k = u_k + \frac{p}{\rho_k} \quad (2.56)$$

For the particular case of steady-state, two-phase gas(_G)/liquid(_L) flow in a constant area channel with no internal heat generation ($\dot{\phi}_k$), equation (2.55) reduces to the following expressions for the vapor and liquid phases:

$$\begin{aligned} d \left[\dot{M}_G \left(i_G + \frac{u_G^2}{2} \right) \right] + \dot{M}_G g \sin \theta \delta z = \\ \phi_{wG} P_{wG} \delta z + \phi_{GL} P_{GL} \delta z + u_G \tau_{GL} P_{GL} \delta z + \Gamma_G \delta z \left(i_G + \frac{u_G^2}{2} \right) \end{aligned} \quad (2.57)$$

$$\begin{aligned} d \left[\dot{M}_L \left(i_L + \frac{u_L^2}{2} \right) \right] + \dot{M}_L g \sin \theta \delta z = \\ \phi_{wL} P_{wL} \delta z + \phi_{LG} P_{LG} \delta z + u_L \tau_{LG} P_{LG} \delta z + \Gamma_L \delta z \left(i_L + \frac{u_L^2}{2} \right) \end{aligned} \quad (2.58)$$

Adding equations (2.57) and (2.58) and taking into account the conservation of energy across the interface, the results gives:

$$\Gamma_G \left(i_G + \frac{u_G^2}{2} \right) + \phi_{GL} P_{GL} + u_G \tau_{GL} P_{GL} = \Gamma_L \left(i_L + \frac{u_L^2}{2} \right) + \phi_{LG} P_{LG} + u_L \tau_{LG} P_{LG} \quad (2.59)$$

We can now obtain the following differential equation for this simplified approach:

$$\frac{d}{dz} [\dot{M}_G i_G + \dot{M}_L i_L] + \frac{d}{dz} \left[\frac{\dot{M}_G u_G^2}{2} + \frac{\dot{M}_L u_L^2}{2} \right] + (\dot{M}_G + \dot{M}_L) g \sin \theta = Q_{wL} \quad (2.60)$$

where the term Q_{wL} ($= \phi_{wL} P_{wL} + \phi_{wG} P_{wG}$) represents the heat transferred to the fluid across the channel length per unit of wall.

Using relationships introduced in this chapter, equation (2.60) may be written

$$\begin{aligned} -\frac{dp}{dz} \left[\frac{x}{\rho_G} + \frac{(1-x)}{\rho_L} \right] &= \left\{ \frac{dE}{dz} - \frac{Q_{wL}}{(\dot{M}_G + \dot{M}_L)} \right\} + \\ &+ \left\{ p \frac{d}{dz} \left[\frac{x}{\rho_G} + \frac{(1-x)}{\rho_L} \right] + \frac{G^2}{2} \frac{d}{dz} \left[\frac{x^3}{\rho_G^2 \epsilon^2} + \frac{(1-x)^3}{\rho_L^2 (1-\epsilon)^2} \right] \right\} + g \sin \theta \end{aligned} \quad (2.61)$$

where $E = x e_G + (1-x) e_L$ is the flow-weighted mixture internal energy per unit of mass.

The above equation shows that the total pressure gradient can be expressed in terms of a frictional dissipation term (first bracketed term), an accelerational term (second bracketed term) and a static head term (final term).

It should be pointed out that the frictional dissipation term $\left(\frac{dE}{dz} - \frac{Q_{wL}}{\dot{M}_G + \dot{M}_L} \right)$ includes the dissipation of mechanical energy not only within the fluid due to friction at the channel walls but also at the interface due to the relative motion of the phases.

Chapter 3

Overview of Flow Pattern Maps

For two-phase flow, the respective distribution of the liquid and vapor phases is an important factor of their description. Their respective distribution take on some commonly observed flow structures, which are defined as **two-phase flow patterns** or **flow regimes**, and they present particular identifying characteristics. In fact, pressure drops and heat transfer coefficients are closely related to the local flow structure of the fluid, and thus two-phase flow pattern prediction is an important aspect of modelling evaporation and condensation. Hence, in order to obtain local flow pattern based models, a reliable **flow pattern map** to identify what type of flow pattern exists at the local flow conditions is needed. Analogous to predicting the transition from laminar to turbulent flow in single-phase flows, two-phase flow pattern maps are used for predicting the transition from one type of two-phase flow pattern to another.

In this chapter, first the geometric characteristics of flow patterns inside horizontal tubes will be described. Second, several widely quoted, older flow pattern maps for horizontal flows will be presented. Finally, a recent flow pattern map and corresponding flow regime transition equations specifically for diabatic flows and in particular for evaporation in horizontal tubes will be presented.

3.1 Flow patterns in horizontal flow

Flow patterns for co-current flow of gas and liquid in a horizontal tube are strongly influenced by gravity that acts to stratify the liquid to the bottom of the tube and the gas to the top. The liquid and gas phases distribute themselves into several recognizable flow structures. These are referred to as flow patterns or flow regimes and they are shown in Fig. (3.1) and can be described as follows:

- **Bubbly flow.** The gas bubbles are dispersed in the liquid with a high concentration of bubbles in the upper half of the tube due to their buoyancy. When shear forces are dominant, the bubbles tend to disperse uniformly in the tube. For horizontal flows, this regime only occurs at high mass flow rates.
- **Stratified flow.** At low liquid and gas velocities, complete separation of the two phases occurs. The gas goes to the top and the liquid to the bottom of the tube. Both phases are separated by an undisturbed flat interface. Therefore, the liquid and gas are fully stratified in this regime.

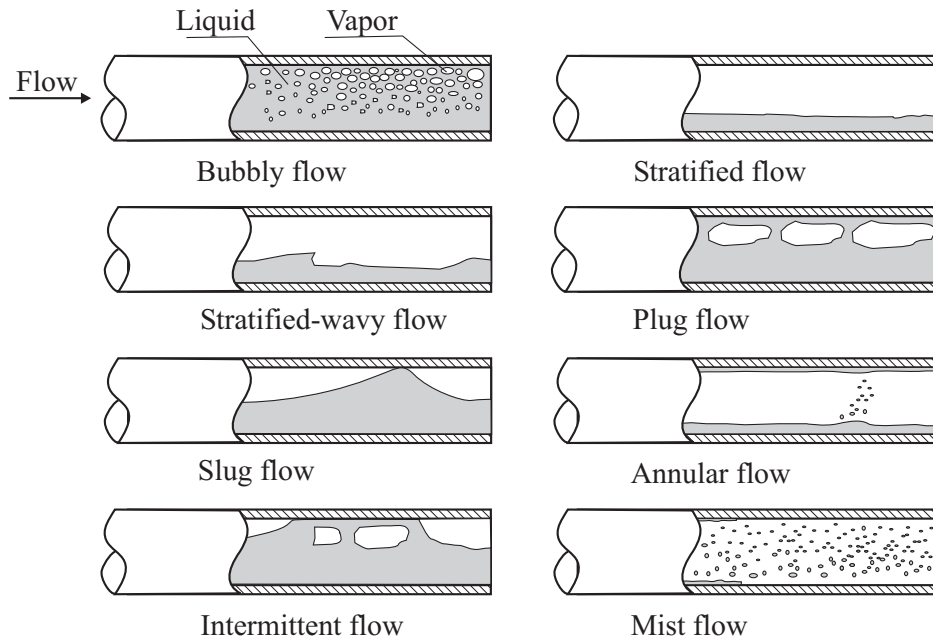


Figure 3.1: Two-phase flow patterns in horizontal flow.

- **Stratified-wavy flow.** Increasing the gas velocity in a stratified flow, waves are formed on the interface and travel in the direction of the flow. The amplitude of the waves is notable and depends on the relative velocity of the two phases; however, their crests do not reach the top of the tube. The waves climb up the sides of the tube, leaving behind thin films of liquid on the wall.
- **Intermittent flow.** Further increasing the gas velocity, these interfacial waves become large enough to wash the top of the tube. This regime is characterized by large amplitude waves intermittently washing the top of the tube with smaller amplitude waves in between. Large amplitude waves often contain entrained bubbles. The top wall is nearly continuously wetted by the large amplitude waves and the thin liquid films left behind. Intermittent flow is also a composite of the plug and slug flow regimes. These subcategories are characterized as follows:
 - **Plug flow.** This regimen has liquid plugs that are separated by elongated bubbles. The diameters of the elongated bubbles are much smaller than the tube such that the liquid phase is continuous along the bottom of the tube below the elongated bubbles.
 - **Slug flow.** At higher gas velocities, the diameters of elongated bubbles become similar in size to the channel height. The liquid slugs separating such elongated bubbles can also be described as large amplitude waves.
- **Annular flow.** At even larger gas flow rates, the liquid forms a continuous film around the perimeter of the tube. The interface between the liquid annulus and the vapor core is disturbed by small amplitude waves and droplets may be dispersed in the gas core. At high gas fractions, the top of the tube with its thinner film becomes dry first, so that the annular film covers only part of the tube perimeter and thus this is then classified as stratified-wavy flow.

- **Mist flow.** At very high velocities most of the liquid is entrained as spray by the gas. The spray appears to be produced by the high velocity gas ripping the annular liquid film off from the wall.

3.2 Flow pattern maps in horizontal flow

The analysis of single-phase flow is made easier if one can establish that the flow is either laminar or turbulent and whether any separation or secondary flow effect occurs. This information is equally important in the study of gas-liquid flow. However, perhaps of greater importance in the latter case is the topology or geometry of the flow, i.e. the corresponding flow patterns or flow regimes. Fig. (3.2) shows a schematic representation of a horizontal tubular channel heated by a uniform low heat flux and fed with liquid just below the saturation temperature.

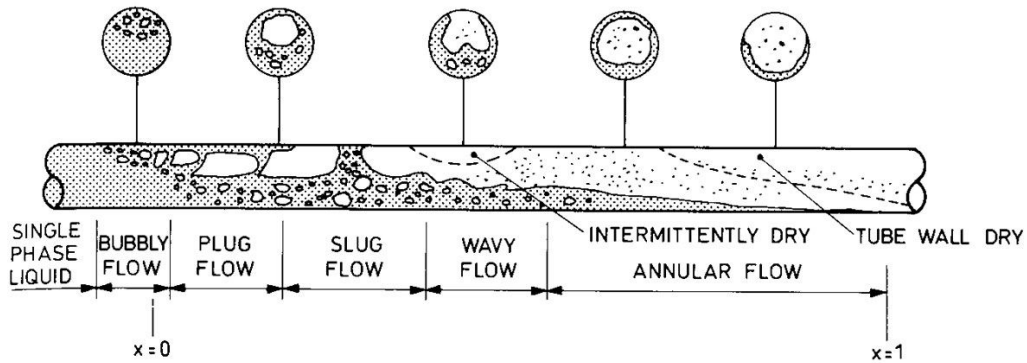


Figure 3.2: Flow patterns during evaporation in a horizontal tube ([35]).

To predict the local flow pattern in a tube, a **flow pattern map** is used. These are an attempt, on a two-dimensional graph, to separate the space into areas corresponding to the various flow regimes. It should be pointed out that the flow pattern is also influence by a number of secondary variables but it is not possible to represent their influence using only a two-dimensional plot. One should be aware that transition curves on flow pattern maps should be considered as transition zones analogous to that between laminar and turbulent flows.

3.2.1 Baker flow pattern map

The first to recognize the importance of the flow pattern as a starting point for the calculation of pressure drop, void fraction, and heat and mass transfer was Baker [7] in 1954. He published the earliest flow pattern map for horizontal flow, presented in Fig. (3.3).

To utilize this map, first the mass velocities of the liquid G_L and vapor G_G must be determined. Then the gas-phase parameter λ and the liquid-phase parameter ψ are calculated as follows:

$$\lambda = \left(\frac{\rho_G}{\rho_{air}} \frac{\rho_L}{\rho_{water}} \right)^{1/2} \quad (3.1)$$

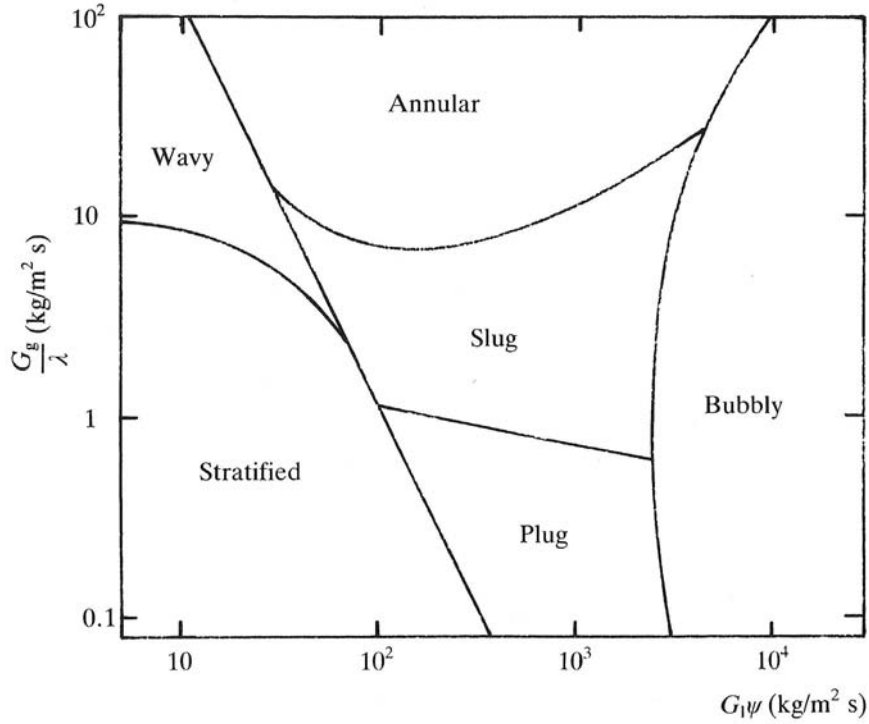


Figure 3.3: Baker (1954) flow pattern map for horizontal flow in a tube.

$$\psi = \left(\frac{\sigma_{water}}{\sigma} \right) \left[\left(\frac{\mu_L}{\mu_{water}} \right) \left(\frac{\rho_{water}}{\rho_L} \right)^2 \right]^{1/3} \quad (3.2)$$

where ρ_G , ρ_L , μ_L and σ are the properties of the fluid and ρ_{water} , ρ_{air} , μ_{water} and σ_{water} are the reference properties of air and water at standard atmospheric pressure and room temperature. This map was developed based on air-water data. Note that λ and ψ are standard dimensionless parameters that should take into account the variation in the properties of the fluid.

3.2.2 Mandhane et al. flow pattern map

In the interest of simplicity, Mandhane et al. [91] in 1974 proposed a basic flow pattern map based on air-water data, and then attempt to apply physical property corrections. While this was certainly not a new approach, previous workers did not have access to the amount of data that were available for this study. The proposed flow pattern map is shown in Fig. (3.4). It should be noted that the transition between adjacent flow patterns do not occur suddenly but over a range of flow rates. Thus, in this figure, transitions between flow patterns are shown as broad bands instead of lines.

The transition boundaries indicated were located on the basis of a $\log V_{SL}$ vs. $\log V_{SG}$ plot of the 1178 observations for the air-water system, where $V_{SL}(j_L)$ and $V_{SG}(j_G)$ are respectively the liquid and vapor superficial velocities. One of the mayor improvements of this approach was that they showed that the effect of tube diameter was adequately taken into account by using the superficial velocities, V_{SL} and V_{SG} , as the coordinate axes.

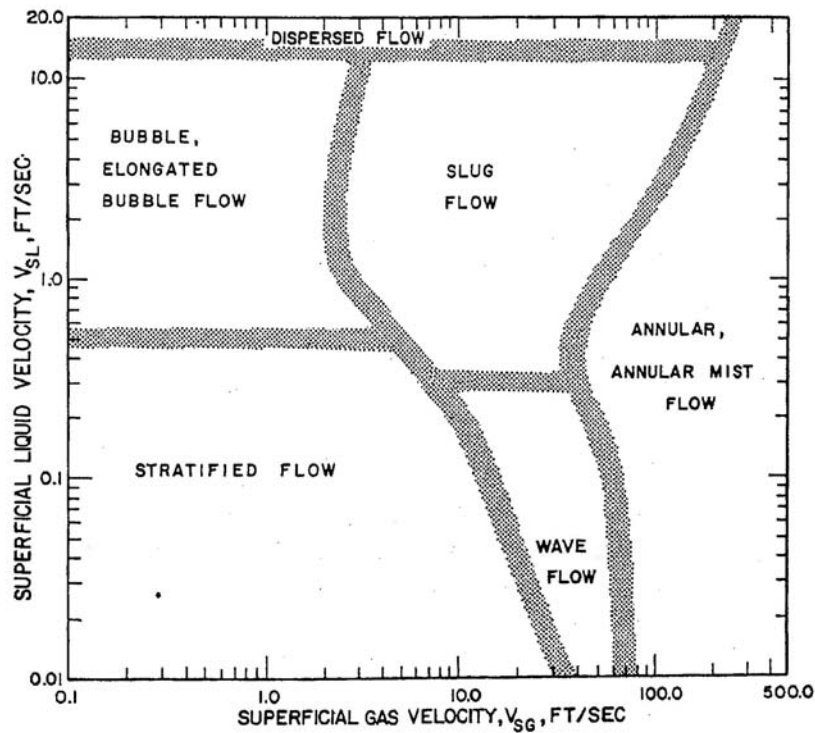


Figure 3.4: Mandhane (1974) flow pattern map for horizontal flow in a tube.

As pointed out, the Mandhane et al. flow pattern map was developed using air-water data. In order to take into account the variation in the properties of the fluid, they proposed two dimensionless parameters. These factors are applied to the flow pattern boundaries rather than to the axes of the map following the procedure well described in their paper. The proposed map, and the physical property correction procedure were then compared with a huge data bank.

3.2.3 Taitel and Dukler flow pattern map

Taitel and Dukler [125] proposed in 1976 a flow pattern map for horizontal flow in tubes. This map is shown in Fig. (3.5) and is based on their analytical analysis of the flow transition mechanisms together with empirical selection of several parameters. The proposed map has a better scientific basis than many of the previous attempts and thus extrapolates better than the others maps. The map uses the Martinelli parameter X , the gas Froude number Fr_G and the parameters T and K and is composed of three graphs.

The Martinelli parameter is:

$$X = \left[\frac{(dp/dz)_L}{(dp/dz)_G} \right]^{1/2} \quad (3.3)$$

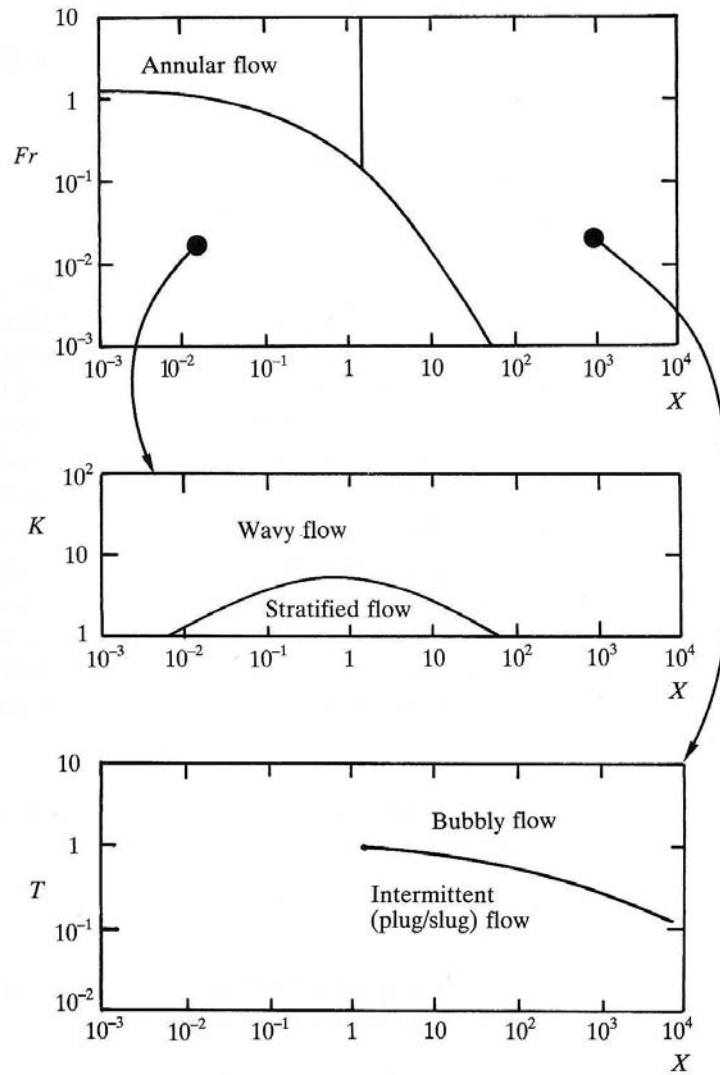


Figure 3.5: Taitel and Dukler (1976) flow pattern map for horizontal flow in a tube.

The gas-phase Froude number is:

$$Fr_G = \frac{G_G}{[\rho_G(\rho_L - \rho_G)Dg]^{1/2}} \quad (3.4)$$

Their parameter T is:

$$T = \left[\frac{|(dp/dz)_L|}{g(\rho_L - \rho_G)} \right]^{1/2} \quad (3.5)$$

Their parameter K is:

$$K = Fr_G Re_L^{1/2} \quad (3.6)$$

where the liquid-phase and vapor-phase Reynolds numbers are:

$$Re_L = \frac{G_L D}{\mu_L} \quad (3.7)$$

$$Re_G = \frac{G_G D}{\mu_G} \quad (3.8)$$

The pressure gradient of the flow for phase k (where k is either L or G) is:

$$(dp/dz)_k = -\frac{2f_k G_k^2}{\rho_k D} \quad (3.9)$$

For $Re_k \leq 2000$, the laminar flow friction factor is used:

$$f_k = \frac{16}{Re_k} \quad (3.10)$$

For $Re_k > 2000$, the turbulent flow friction factor equation is used:

$$f_k = \frac{0.079}{Re_k^{1/4}} \quad (3.11)$$

To implement the map, one first determines the Martinelli parameter X and Fr_G . Using these two parameters on the top graph, if their coordinates fall in the annular flow regime, then the flow pattern is annular. If the coordinates of X and Fr_G fall in the lower left zone of the top of the graph, then K is calculated. Using K and X in the middle graph, the flow regime is identified as either stratified-wavy or fully stratified. If the coordinates of X and Fr_G fall in the right zone on the top graph, then T is calculated. Using T and X in the bottom graph, the flow regime is identified as either bubbly flow or intermittent (plug or slug) flow.

3.2.4 Hashizume flow pattern map

Hashizume [59] in 1983 performed flow pattern observation experiments for refrigerant two-phase flow in a horizontal tube. He showed that the flow pattern boundaries of refrigerant two-phase flows differ considerably from those of Baker map, which was based on air-water data. He concluded that the flow patterns of refrigerant two-phase flows can be presented on a revised Baker map, where the property correction factor on surface tension was modified. The revised Baker map is shown in Fig. (3.6).

The modified property correction factor proposed is:

$$\psi' = \left(\frac{\sigma_{water}}{\sigma}\right)^{1/4} \left[\left(\frac{\mu_L}{\mu_{water}}\right) \left(\frac{\rho_{water}}{\rho_L}\right)^2 \right]^{1/3} \quad (3.12)$$

Because the correction term (σ_{water}/σ) for the air-water system is nearly unity, the modified Baker map with Eq. (3.12) is practically identical to the original Baker map for air-water system.

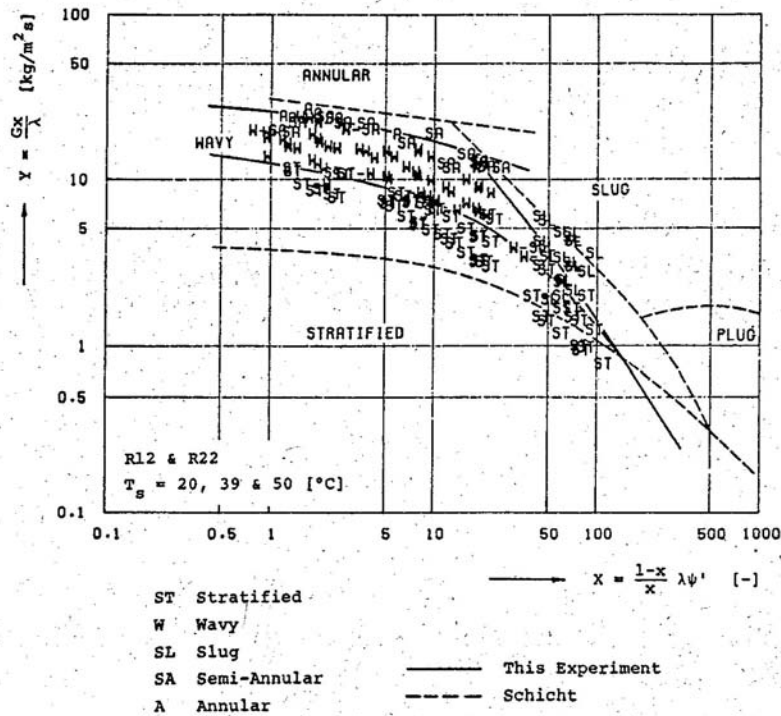


Figure 3.6: Hashizume (1983) flow pattern map for horizontal flow in a tube.

In fact, Hashizume was one of the first to propose a flow pattern map based on observations for refrigerants instead of air-water as in most of previous work.

3.2.5 Kattan-Thome-Favrat flow pattern map

These above flow patterns maps were all developed for adiabatic two-phase flows but are often extrapolated for use with the diabatic process of evaporation. As with any extrapolation, this may or may not produce reliable results. Important factors influencing the flow during evaporation, which may have an effect on transition between flow regimes, are nucleate boiling, evaporation of liquid films and the accelerational of the flow due to the phase change. It is desirable to define for this type of flow a flow pattern map that includes the influences of heat flux and dryout on the flow pattern transition boundaries and one one which is also easier to implement than the frequently used $\log - \log$ format. As a first step in this direction Kattan, Thome and Favrat [76, 77, 78] proposed a modification of the Steiner [122] map, which is itself a modified Taitel-Dukler map, and included a method for predicting the onset of dryout at the top of the tube in evaporating annular flows. This flow pattern map will be presented here and the corresponding flow regime transition boundaries are depicted in Fig. (3.7) (bubbly flow occurs at very high velocities and is not shown). This map provides the transition boundaries (calculated from their underlying transitions equations) on a linear-linear graph with mass velocity plotted versus gas or vapor fraction for the particular fluid and flow channel, which is much easier to use than the $\log - \log$ format of other maps.

For the sake of simplicity, the transition between stratified and stratified-wavy flow will be designated as "S-SW", between stratified-wavy and intermittent/annular as "SW-I/A", between

intermittent and annular as "I-A", between annular and mist flow "A-M" and between intermittent and bubbly flow as "I-B".

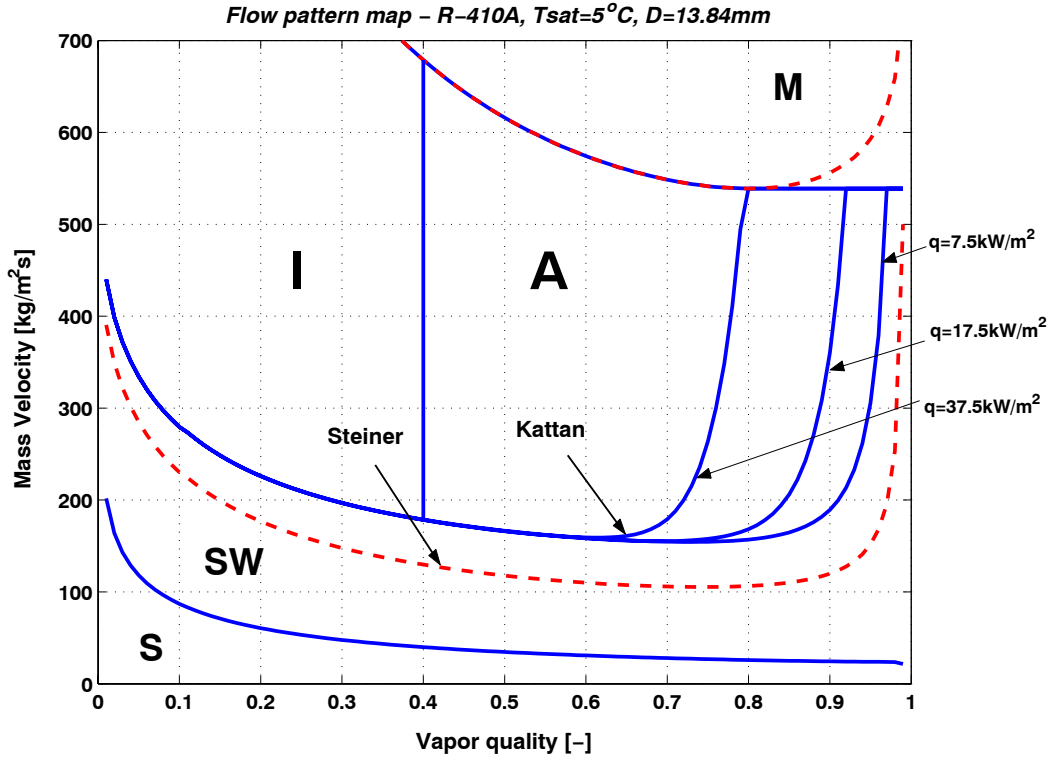


Figure 3.7: Kattan (1998) flow pattern map (solid lines) evaluated for refrigerant R-410A at $T_{sat} = 5^\circ C$ in 13.84 mm internal diameter tube.

The transition "S-SW" is given by the expression:

$$G_{strat} = \left\{ \frac{(226.3)^2 A_{LD} A_{GD}^2 \rho_G (\rho_L - \rho_G) \mu_L g}{x^2 (1-x) \pi^3} \right\}^{1/3} \quad (3.13)$$

The transition "S-I/A" is:

$$G_{wavy} = \left\{ \frac{16 A_{GD}^3 g D \rho_L \rho_G}{x^2 \pi^2 (1 - (2h_{LD} - 1)^2)^{0.5}} \left[\frac{\pi^2}{25 h_{LD}^2} (1-x)^{-F_1(q)} \left(\frac{We}{Fr} \right)_L^{-F_2(q)} + 1 \right] \right\}^{0.5} + 50 \quad (3.14)$$

The high vapor quality portion of this curve depends on the ratio of the Froude number (Fr_L) to the Weber number (We_L), where Fr_L is the ratio of the inertia to the surface tension forces while We_L is the ratio of inertia to gravity forces. The transition "A-M" is given by the following expression:

$$G_{mist} = \left\{ \frac{7680 A_{GD}^2 g D \rho_L \rho_G}{x^2 \pi^2 \xi_{Ph}} \left(\frac{Fr}{We} \right)_L \right\}^{0.5} \quad (3.15)$$

Evaluating the above expression for the minimum mass velocity of the mist transition gives the value of x_{min} , and when $x > x_{min}$:

$$G_{mist} = G_{min} \quad (3.16)$$

The transition threshold into bubbly flow (not shown in Fig. (3.7)) is given by:

$$G_{bubbly} = \left\{ \frac{256 A_{GD} A_{LD}^2 D^{1.25} \rho_L (\rho_L - \rho_G) g}{0.3164 (1-x)^{1.75} \pi^2 P_i D \mu_L^{0.25}} \right\}^{1/1.75} \quad (3.17)$$

In the above equations, the ratio of We to Fr is

$$\left(\frac{We}{Fr} \right)_L = \frac{g D^2 \rho_L}{\sigma} \quad (3.18)$$

and the friction factor is

$$\xi_{Ph} = \left[1.138 + 2 \log \left(\frac{\pi}{1.5 A_{LD}} \right) \right]^{-2} \quad (3.19)$$

The non-dimensional empirical exponents $F_1(q)$ and $F_2(q)$ in the "S-SW" boundary equation include the effect of heat flux on the onset of dryout of the annular film, i.e. the transition from annular flow into annular flow with partial dryout around the upper perimeter of the tube, the latter is classified as stratified-wavy flow by the map. They are given as:

$$F_1(q) = 646.0 \left(\frac{q}{q_{crit}} \right)^2 + 64.8 \left(\frac{q}{q_{crit}} \right) \quad (3.20)$$

$$F_2(q) = 18.8 \left(\frac{q}{q_{crit}} \right) + 1.023 \quad (3.21)$$

The Kutateladze [85] correlation for the heat flux at the departure from nucleate boiling, q_{crit} , is used to normalize the local heat flux:

$$q_{crit} = 0.131 \rho_G^{1/2} h_{LG} [g(\rho_L - \rho_G)\sigma]^{1/4} \quad (3.22)$$

The transition "I-A" is assumed to occur at a fixed value of the Martinelli parameter, X_{tt} equal to 0.34. Solving for x in Eq. (2.37), the threshold line intermittent-to-annular flow transition at x_{IA} is:

$$x_{IA} = \left\{ \left[0.2914 \left(\frac{\rho_G}{\rho_L} \right)^{-1/1.75} \left(\frac{\mu_L}{\mu_G} \right)^{-1/7} \right] + 1 \right\}^{-1} \quad (3.23)$$

Fig. (3.8) defines the geometrical dimensions of the flow where P_L is the wetted perimeter of the tube, P_G is the dry perimeter in contact with only vapor, h_L is the height of the completely stratified liquid layer, and P_i is the length of the phase interface. Similarly A_L and A_G are the corresponding

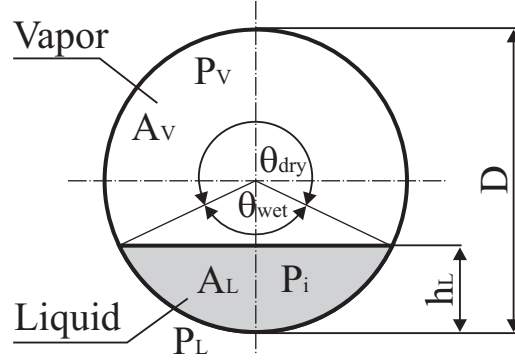


Figure 3.8: Cross-sectional and peripheral fractions in a circular tube.

cross-sectional areas. Normalizing with the tube internal diameter, D , six dimensionless variables are obtained:

$$h_{LD} = \frac{h_L}{D}; \quad P_{LD} = \frac{P_L}{D}; \quad P_{GD} = \frac{P_G}{D}; \quad P_{iD} = \frac{P_i}{D}; \quad A_{LD} = \frac{A_L}{D^2}; \quad A_{GD} = \frac{A_G}{D^2}; \quad (3.24)$$

The dimensionless peripheral and cross-sectional area variables that are required for analysis can be derived from the geometry for a given liquid height h_L or for a reference liquid level h_{LD} .

For $h_{LD} \leq 0.5$:

$$P_{LD} = (8(h_{LD})^{0.5} - 2(h_{LD}(1 - h_{LD}))^{0.5}) / 3 \quad (3.25)$$

$$P_{GD} = \pi - P_{LD} \quad (3.26)$$

$$A_{LD} = (12(h_{LD}(1 - h_{LD}))^{0.5} + 8(h_{LD})^{0.5}) h_{LD} / 15 \quad (3.27)$$

$$A_{GD} = \frac{\pi}{4} - A_{LD} \quad (3.28)$$

For $h_{LD} > 0.5$:

$$P_{GD} = (8(h_{LD})^{0.5} - 2(h_{LD}(1 - h_{LD}))^{0.5}) / 3 \quad (3.29)$$

$$P_{LD} = \pi - P_{GD} \quad (3.30)$$

$$A_{GD} = (12(h_{LD}(1 - h_{LD}))^{0.5} + 8(h_{LD})^{0.5}) h_{LD} / 15 \quad (3.31)$$

$$A_{LD} = \frac{\pi}{4} - A_{GD} \quad (3.32)$$

For $0 \leq h_{LD} \leq 1$:

$$P_{iD} = 2(h_{LD}(1 - h_{LD}))^{0.5} \quad (3.33)$$

Since h_L is unknown, an iterative method utilizing the following equation is necessary to calculate the reference liquid level h_{LD} :

$$X_{tt}^2 = \left[\left(\frac{P_{GD} + P_{iD}}{\pi} \right)^{1/4} \left(\frac{\pi^2}{64A_{GD}^2} \right) \left(\frac{P_{GD} + P_{iD}}{A_{GD}} + \frac{P_{iD}}{A_{LD}} \right) \right] \left(\frac{\pi}{P_{LD}} \right)^{1/4} \left(\frac{64A_{LD}^3}{\pi^2 P_{LD}} \right) \quad (3.34)$$

Once the reference liquid level h_{LD} is known, the dimensionless variables are calculated from Eqs. (3.25) to (3.33) and the transition curves for the flow pattern map are determined with Eqs. (3.13) to (3.23).

An improved version of this map was proposed by Zürcher et al. [165] (1999), Zürcher [166] (2000) and Zürcher et al. [163] (2002), respectively. This improved version of Kattan flow pattern map respects their ammonia flow pattern observations but is in fact quite complex to implement. It used the Taitel and Dukler [125] (1976) void fraction model for fully stratified flows, the Rouhani-Axelsson [110] (1970) void fraction model for intermittent and annular flows and interpolates between these two for stratified-wavy flows. Also, it includes a dissipation function in the "SW-A/I" transition curve. The entire set of equations of this improved flow pattern map must be iteratively solved to find the transition curves, which is physically logical but difficult to implement for general practice.

3.2.6 Thome and El Hajal flow pattern map

An easier to implement version of the above maps was proposed by Thome and El Hajal [131]. In the previously presented flow pattern maps, the dimensionless variables A_{LD} , A_{GD} , h_{LD} and P_{iD} were calculated following an iterative procedure using the stratified flow void fraction model of Taitel-Dukler [125]. On the other hand, the flow pattern based heat transfer model of Kattan et al. [78] uses the Steiner [122] version of the Rouhani-Axelsson [110] drift flux model for horizontal tubes to predict the void fraction ϵ :

$$\epsilon = \frac{x}{\rho_G} \left[(1 + 0.12(1 - x)) \left(\frac{x}{\rho_G} + \frac{(1 - x)}{\rho_L} \right) + \frac{1.18(1 - x)[g\sigma(\rho_L - \rho_G)]^{0.25}}{G^2 \rho_L^{0.5}} \right]^{-1} \quad (3.35)$$

This drift flux void fraction model is easy to apply and gives the void fraction as an explicit function of total mass flux, which the method of Taitel-Dukler does not. Therefore, it makes sense to use the same void fraction model in both the flow pattern map and the flow boiling heat transfer model, for which the Rouhani-Axelsson model is a better choice as a general method. This was latter proven experimentally by making 238 void fraction measurements for R-22 and R-410A in Wojtan et al. [154].

Then, knowing the cross-sectional area of the tube, the values A_{LD} and A_{GD} are determinable as:

$$A_{LD} = \frac{A(1 - \epsilon)}{D^2} \quad (3.36)$$

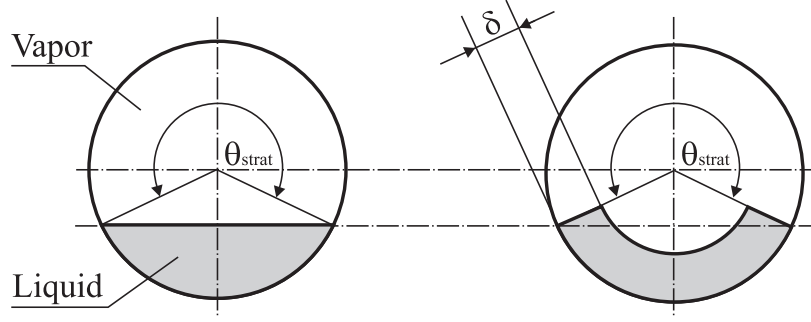


Figure 3.9: Stratified angle in two-phase flow.

$$A_{GD} = \frac{A\epsilon}{D^2} \quad (3.37)$$

The dimensionless liquid height h_{LD} and the dimensionless length of the liquid interface P_{iD} can be expressed as a function of stratified angle θ_{strat} :

$$h_{LD} = 0.5 \left(1 - \cos \left(\frac{2\pi - \theta_{strat}}{2} \right) \right) \quad (3.38)$$

$$P_{iD} = \sin \left(\frac{2\pi - \theta_{strat}}{2} \right) \quad (3.39)$$

Avoiding any iteration, the stratified angle θ_{strat} can be calculated from an approximate expression, evaluated in terms of void fraction, proposed by Biberg [16] as follows:

$$\theta_{strat} = 2\pi - 2 \left\{ \begin{array}{l} \pi(1 - \epsilon) + \left(\frac{3\pi}{2}\right)^{1/3} [1 - 2(1 - \epsilon) + (1 - \epsilon)^{1/3} - \epsilon^{1/3}] \\ -\frac{1}{200}(1 - \epsilon)\epsilon[1 - 2(1 - \epsilon)[1 + 4((1 - \epsilon)^2 + \epsilon^2)] \end{array} \right\} \quad (3.40)$$

The transition curve "SW-I/A" is determined using the updated expression of Zürcher et al. [165] for G_{wavy} , where G_{wavy} is in kg/m^2s :

$$G_{wavy} = \left\{ \frac{16A_{GD}^3 g D \rho_L \rho_G}{x^2 \pi^2 (1 - (2h_{LD} - 1)^2)^{0.5}} \left[\frac{\pi^2}{25h_{LD}^2} (1 - x)^{-F_1(q)} \left(\frac{We}{Fr} \right)_L^{-F_2(q)} 1 \right] \right\}^{0.5} + 50 - 75 e^{-\left(\frac{x^2 - 0.97}{x(1-x)}\right)^2} \quad (3.41)$$

Similarly, the transition curve from "S-SW" is determined using the other expression of Zürcher et al. [165] for G_{strat} , where G_{strat} is in kg/m^2s :

$$G_{strat} = \left\{ \frac{(226.3)^2 A_{LD} A_{GD}^2 \rho_G (\rho_L - \rho_G) \mu_L g}{x^2 (1 - x) \pi^3} \right\}^{1/3} + 20x \quad (3.42)$$

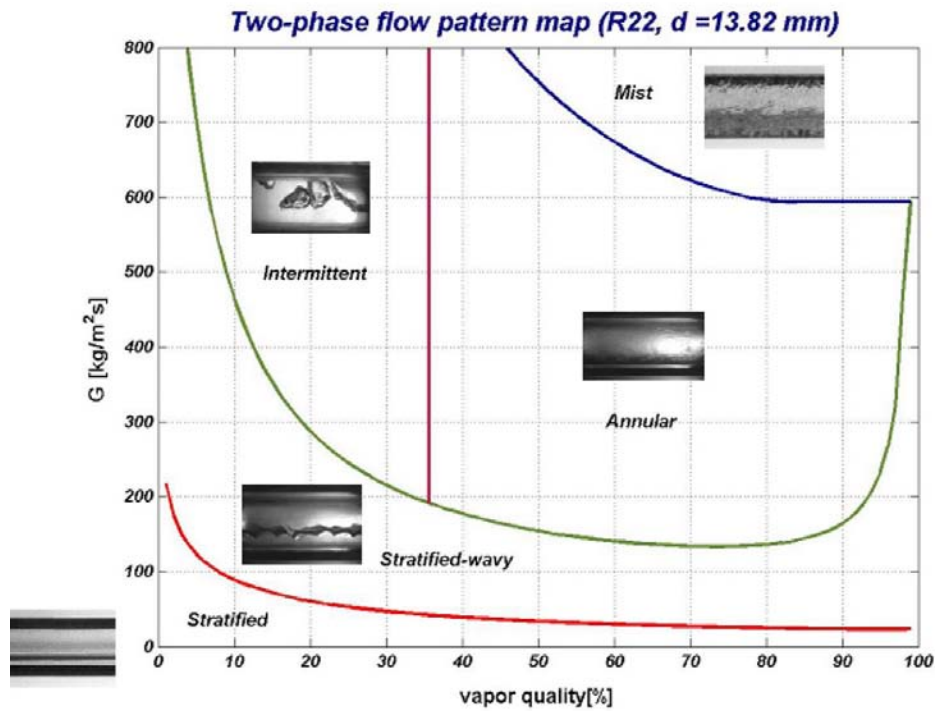


Figure 3.10: Thome-El Hajal (2002) flow pattern map for refrigerant R-22 at $T_{sat} = 5^{\circ}C$ and $q_{flux} = 7.5 kW/m^2$ in 13.84 mm internal diameter tube.

The non-dimensional empirical exponents $F_1(q)$ and $F_2(q)$ were added to the G_{wavy} expression to include the effect of heat flux on the onset of dryout of the annular film, i.e. the transition from annular flow into annular flow with partial dryout. These parameters are determined as:

$$F_1(q) = 646.0 \left(\frac{q/2}{q_{crit}} \right)^2 + 64.8 \left(\frac{q/2}{q_{crit}} \right) \quad (3.43)$$

$$F_2(q) = 18.8 \left(\frac{q/2}{q_{crit}} \right)^2 + 1.023 \quad (3.44)$$

where again the Kutateladze correlation Eq. (3.22) for the critical heat flux q_{crit} was used to normalize the local heat transfer.

The "A-M", "I-A" and "I-B" transition boundaries have not been changed and it is recommended to use them in the same form proposed by Kattan et al. [76].

3.2.7 Wojtan-Ursenbacher-Thome flow pattern map

Based on information obtained from dynamic void fraction measurements and observations of the cross-sectional locus of the liquid-vapor interface, a more recent version of the Kattan et al. flow map has been proposed by Wojtan et al. [155], and also includes the effect of heat flux on the transition to mist flow.

This new map is illustrated in Fig. (3.11) where **S**= stratified flow, **SW**= stratified-wavy flow, **I**= intermittent flow, **A**= annular flow, **M**= mist flow and **D** represents the transition zone between annular and mist flow.

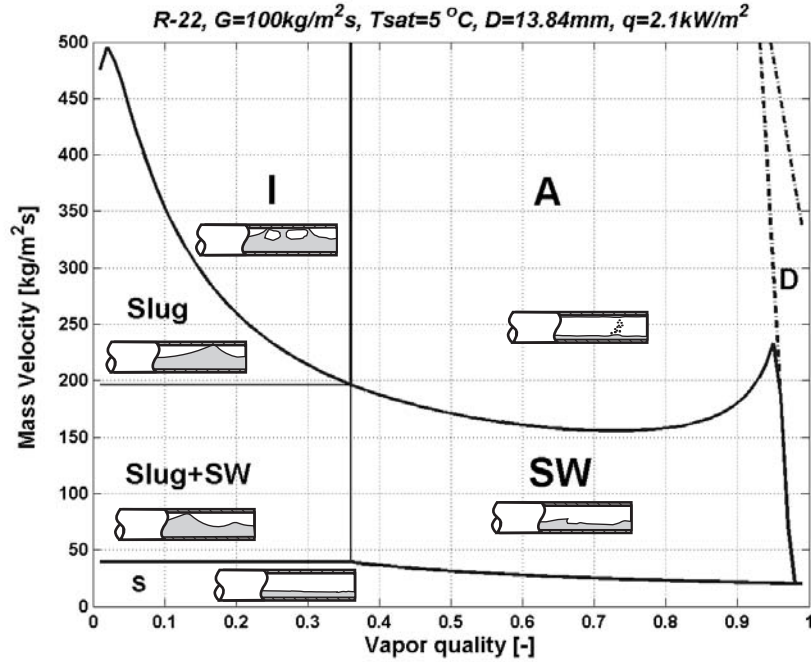


Figure 3.11: Flow pattern map for R-22 at $T_{sat} = 5^\circ C$ in a 13.84 mm internal diameter tube at $G = 100\text{ kg/m}^2\text{ s}$ and $q = 2.1\text{ kW/m}^2$.

The implementation procedure for the updated version is as follows:

1. First, the geometrical parameters ϵ , A_{LD} , A_{VD} , θ_{strat} , h_{LD} and P_{id} are calculated from the following equations:

$$\epsilon = \frac{x}{\rho_G} \left[(1 + 0.12(1-x)) \left(\frac{x}{\rho_G} + \frac{(1-x)}{\rho_L} \right) + \frac{1.18(1-x)[g\sigma(\rho_L - \rho_G)]^{0.25}}{G^2 \rho_L^{0.5}} \right]^{-1} \quad (3.45)$$

$$A_{LD} = \frac{A(1-\epsilon)}{D^2} \quad (3.46)$$

$$A_{GD} = \frac{A\epsilon}{D^2} \quad (3.47)$$

$$\theta_{strat} = 2\pi - 2 \left\{ \begin{array}{l} \pi(1-\epsilon) + \left(\frac{3\pi}{2}\right)^{1/3} [1 - 2(1-\epsilon) + (1-\epsilon)^{1/3} - \epsilon^{1/3}] \\ -\frac{1}{200}(1-\epsilon)\epsilon[1 - 2(1-\epsilon)[1 + 4((1-\epsilon)^2 + \epsilon^2)] \end{array} \right\} \quad (3.48)$$

$$h_{LD} = 0.5 \left(1 - \cos \left(\frac{2\pi - \theta_{strat}}{2} \right) \right) \quad (3.49)$$

$$P_{iD} = \sin\left(\frac{2\pi - \theta_{strat}}{2}\right) \quad (3.50)$$

2. The **S-SW** transition is calculated from:

$$G_{strat} = \left\{ \frac{226.3^2 A_{LD} A_{GD}^2 \rho_G (\rho_L - \rho_G) g \mu_L}{x^2 (1-x) \pi^3} \right\}^{1/3} \quad (3.51)$$

where $G_{strat} = G_{strat}(x_{IA})$ at $x < x_{IA}$.

The flow is stratified whenever $G < G_{strat}$.

3. The **SW-I/A** boundary is calculated from the following equation:

$$G_{wavy} = \left\{ \frac{16 A_{GD}^3 g D \rho_L \rho_G}{x^2 \pi^2 (1 - (2h_{LD} - 1)^2)^{0.5}} \left[\frac{\pi^2}{25 h_{LD}^2} \left(\frac{We}{Fr} \right)_L^{-1} + 1 \right] \right\}^{0.5} + 50 \quad (3.52)$$

The stratified-wavy region lies above the stratified region and is then subdivided into three zones:

- $G > G_{wavy}(x_{IA})$ gives the SLUG zone;
- $G_{strat} < G < G_{wavy}(x_{IA})$ and $x < x_{IA}$ give the SLUG/STRATIFIED-WAVY zone;
- $x \geq x_{IA}$ gives the STRATIFIED-WAVY zone.

4. The **I-A** transition is calculated from the equation below and is extended down to its intersection with G_{strat} :

$$x_{IA} = \left\{ \left[0.34^{1/0.875} \left(\frac{\rho_G}{\rho_L} \right)^{-1/1.75} \left(\frac{\mu_G}{\mu_L} \right)^{1/7} \right] + 1 \right\}^{-1} \quad (3.53)$$

5. The **A-D** boundary is calculated from:

$$G_{dryout} = \left[\frac{\frac{1}{0.235} \left(\ln \left(\frac{0.58}{x} \right) + 0.52 \right) \left(\frac{D}{\rho_G \sigma} \right)^{-0.17}}{\left(\frac{1}{g D \rho_G (\rho_L - \rho_G)} \right)^{-0.37} \left(\frac{\rho_G}{\rho_L} \right)^{-0.25} \left(\frac{q}{q_{crit}} \right)^{-0.70}} \right]^{0.926} \quad (3.54)$$

6. The **D-M** is calculated from:

$$G_{mist} = \left[\frac{\frac{1}{0.0058} \left(\ln \left(\frac{0.61}{x} \right) + 0.57 \right) \left(\frac{D}{\rho_G \sigma} \right)^{-0.38}}{\left(\frac{1}{g D \rho_G (\rho_L - \rho_G)} \right)^{-0.15} \left(\frac{\rho_G}{\rho_L} \right)^{0.09} \left(\frac{q}{q_{crit}} \right)^{-0.27}} \right]^{0.943} \quad (3.55)$$

The following conditions are then applied to define the transitions in the high quality range:

If $G_{strat} \geq G_{dryout}$, then $G_{dryout} = G_{strat}$

If $G_{wavy} \geq G_{dryout}$, then $G_{dryout} = G_{wavy}$

The maximum values of x to use in Eqs. (3.54) and (3.55) are 0.99

This updated version provides a more accurate prediction of different flow regimes (in particular the onset and completion of dryout around the tube perimeter) and does not require any iterative calculations. Therefore, it can be easily used for flow regime identification.

3.3 Conclusions

Many flow pattern maps are available for predicting adiabatic two-phase flow regimes in horizontal tubes, but most of them were developed based on air-water data and just few were specifically developed for refrigerants. In order to overcome this difficulty, some empirical factors were introduced to extrapolate one of these air-water maps to refrigerants. Another important characteristic is that most maps were developed for adiabatic conditions and then extrapolated to diabatic conditions. As it has been pointed out previously, the extrapolation procedure may not always produce reliable results.

The original Kattan-Thome-Favrat flow pattern map and their respective updates, were developed specifically for refrigerants under diabatic and adiabatic conditions, overcoming thus the two drawbacks previously mentioned. Furthermore, the Wojtan-Ursenbacher-Thome version of the original Kattan-Thome-Favrat flow pattern map includes the influences of heat flux and dryout on the flow pattern transition boundaries providing a much more accurate prediction of the flow regimes. Finally this map avoids any iterative calculations and thus can be easily used for flow regime identification.

Chapter 4

Two-Phase Pressure Drop Models

Despite numerous theoretical and experimental investigations, no general models are available that reliably predict two-phase pressure drops. A reason for this is that two-phase flow includes all the complexities of single-phase like non-linearities, transition to turbulence and instabilities plus additional two-phase characteristics like motion and deformation of the interface, non-equilibrium effects and interactions between phases. The prediction of this important design parameter is made by one of three approaches: **empirical** correlations, **analytical** models or **phenomenological** models. In this chapter these different approaches are examined and principal advantages and disadvantages presented. Also in this chapter leading existing methods are presented and critically reviewed.

4.1 Two-phase pressure drops

The total pressure drop of a fluid is the sum of the variation of potential energy of the fluid, kinetic energy of the fluid and that due to friction on the channel walls. Thus, the total pressure drop Δp_{total} is the sum of the static pressure drop (elevation head) Δp_{static} , the momentum pressure drop (acceleration) Δp_{mom} , and the frictional pressure drop Δp_{frict} :

$$\Delta p_{total} = \Delta p_{static} + \Delta p_{mom} + \Delta p_{frict} \quad (4.1)$$

For a horizontal tube, there is no change in static head so $\Delta p_{static} = 0$. The momentum pressure drop reflects the change in kinetic energy of the flow and is given by:

$$\Delta p_{mom} = G^2 \left\{ \left[\frac{(1-x)^2}{\rho_L(1-\epsilon)} + \frac{x^2}{\rho_G\epsilon} \right]_{out} - \left[\frac{(1-x)^2}{\rho_L(1-\epsilon)} + \frac{x^2}{\rho_G\epsilon} \right]_{in} \right\} \quad (4.2)$$

where G is the total mass velocity of liquid plus vapor and x is the vapor quality.

The momentum pressure drop reflects the change in kinetic energy of the flow and is calculable, for evaporating flows in horizontal tubes, by input of the inlet and outlet vapor qualities and void fractions. When measuring two-phase pressure drop for evaporation in horizontal tubes, the frictional pressure is obtainable by subtracting the momentum pressure drop from the measured total pressure drop from the measured total pressure drop since the static pressure drop is zero.

4.2 Empirical methods

This is a commonly used approach in modelling two-phase pressure drop. The main reason in following this approach is that minimum knowledge of the system characteristics is required. Thus, empirical models are easy to implement and often they provide good accuracy in the range of the database available for the correlations development. As a consequence, one of principal disadvantages of this approach is that they are limited by the range of their underlying database. Another important disadvantage of the empirical approach is that no single correlation is able to provide an acceptable accuracy for general sense.

Below, the most quoted empirical methods are presented and critically reviewed.

4.2.1 Lockhart-Martinelli [90]

This work will be considered first because of its extensive historical use and the continued references to it in the literature. In this treatment they postulated that two-phase flow could be divided into four flow regimes: (1) liquid and gas both turbulent (tt), (2) liquid turbulent and gas viscous (tv), (3) liquid viscous and gas turbulent (vt), (4) liquid and gas both viscous (vv).

The changeover points were selected to be consistent with single-phase flow and to give the best correlation of the experimental data. There are two basic postulates on which the analysis is based: (1) The static pressure drop for liquid and gaseous phases must be equal regardless of the flow pattern; (2) The volume occupied by the liquid plus the gas at any instant (position) must equal the total volume of the pipe. These postulates imply that the flow pattern does not change along the tube length. In effect they eliminate those flows which have large pressure fluctuations, such slug and intermittent flows, and those with radial pressure gradients, such as stratified and stratified-wavy flows.

In the final correlation, the two-phase frictional pressure drop based on a two-phase multiplier for the liquid-phase, or the vapor-phase, respectively, is:

$$\Delta p_{frict} = \phi_L^2 \Delta p_L \quad (4.3)$$

$$\Delta p_{frict} = \phi_G^2 \Delta p_G \quad (4.4)$$

where the terms Δp_L and Δp_G represent the frictional two-phase pressure drop that would exist if the the flow as a liquid or gas, respectively, were assumed to flow alone in the entire cross-section of the channel, and are calculated as:

$$\Delta p_L = 4f_L \left(\frac{L}{D} \right) G^2 (1-x)^2 \left(\frac{1}{2\rho_L} \right) \quad (4.5)$$

$$\Delta p_G = 4f_G \left(\frac{L}{D} \right) G^2 x^2 \left(\frac{1}{2\rho_G} \right) \quad (4.6)$$

The single-phase friction factors of the liquid f_L and vapor f_G and Reynolds numbers are calculated using the classical definition with their respective physical properties:

$$f_L = \frac{0.079}{Re_L^{0.25}} \quad \text{where} \quad Re_L = \frac{G(1-x)D}{\mu_L} \quad (4.7)$$

$$f_G = \frac{0.079}{Re_G^{0.25}} \quad \text{where} \quad Re_G = \frac{GxD}{\mu_G} \quad (4.8)$$

Then, Martinelli and his co-workers argued that the two-phase friction multipliers ϕ_L^2 and ϕ_G^2 could be correlated uniquely as a function of Martinelli parameter X , which represents the ratio between the theoretical pressure gradients which would occur if either fluid were flowing alone in the pipe with the original flow rate of each phase and is calculated with Eq. (2.33), accounting for the flow regime of each phase. This was verified using their experimental data.

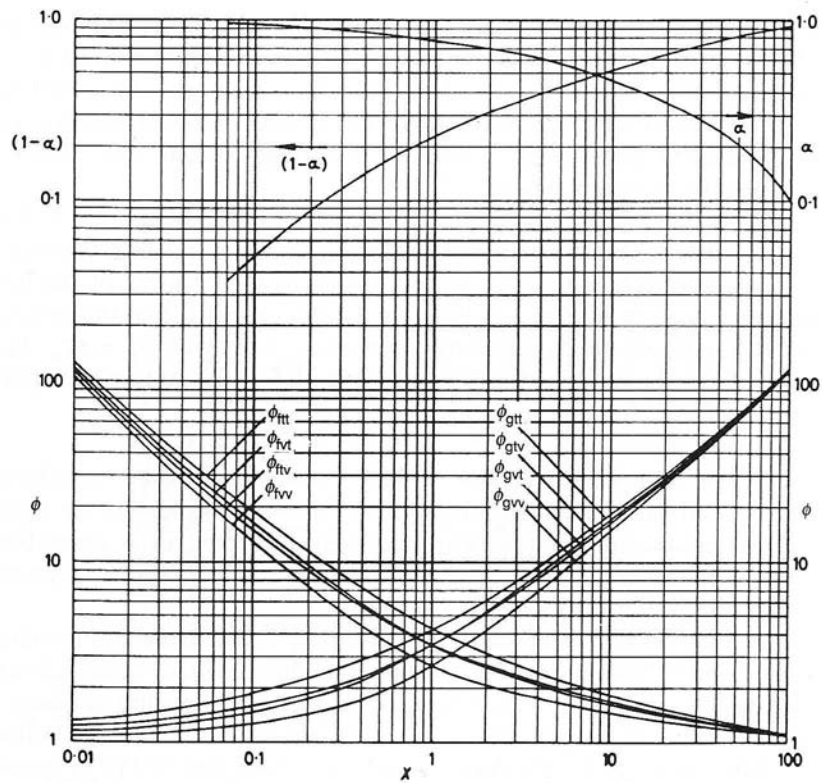


Figure 4.1: Lockhart-Martinelli correlation.

The resulting graphical correlation is shown in Fig. (4.1) where ϕ (note: not ϕ^2) is plotted against X . All flow regimes were correlated in this manner and the corresponding ϕ_L^2 and ϕ_G^2 can be related to the parameter X by relationships of the form

$$\phi_L^2 = 1 + \frac{C}{X} + \frac{1}{X^2} \quad (4.9)$$

$$\phi_G^2 = 1 + CX + X^2 \quad (4.10)$$

The curves in Fig. (4.1) are well represented by Eqs. (4.9) and (4.10) when C takes the following values:

liquid	gas		C
turbulent	turbulent	(tt)	20
viscous	turbulent	(vt)	12
turbulent	viscous	(tv)	10
viscous	viscous	(vv)	5

Table 4.1: Values of C to fit the empirical curves of Lockhart and Martinelli.

To use this method to calculate the two-phase frictional pressure drop, it is only necessary to calculate the frictional pressure drop for each phase flowing alone in the channel and then use Fig. (4.1) or alternatively Eqs. (4.9) and (4.10). The correlation was developed for horizontal two-phase flow of two-component systems at low pressures (close to atmospheric) and its application to situations outside this range of conditions is not recommended.

4.2.2 Bankoff [9]

Bankoff made an extension of the homogeneous two-phase model by including some two-dimensional effects. He derived expressions for the axial variation of velocity and void fraction in a tube. The assumption was that the axial variation could be determined using a power law function. His two-phase frictional pressure gradient is

$$\left(\frac{dp}{dz}\right)_{fric} = \left(\frac{dp}{dz}\right)_{L0} \phi_{Bf}^{7/4} \quad (4.11)$$

The liquid frictional pressure gradient is

$$\left(\frac{dp}{dz}\right)_{L0} = f_{L0} \frac{2G^2}{D\rho_L} \quad (4.12)$$

and the liquid friction factor f_{L0} is calculated as follows:

$$f_{L0} = \frac{0.079}{Re_{L0}^{0.25}} \quad \text{where} \quad Re_{L0} = \frac{GD}{\mu_L} \quad (4.13)$$

His two-phase multiplier is

$$\phi_{Bf} = \frac{1}{1-x} \left[1 - \gamma \left(1 - \frac{\rho_G}{\rho_L}\right)\right]^{\frac{3}{7}} \left[1 + x \left(\frac{\rho_L}{\rho_G} - 1\right)\right] \quad (4.14)$$

where

$$\gamma = \frac{0.71 + 2.35 \left(\frac{\rho_G}{\rho_L} \right)}{1 + \left(\frac{1-x}{x} \right) \left(\frac{\rho_G}{\rho_L} \right)} \quad (4.15)$$

This method was derived using data for steam-water mixtures and is applicable to vapor qualities from $0 < x < 1$.

4.2.3 Cicchitti et al. [34]

Cicchitti et al. developed a simple correlation for steam-water systems. The experimental test conditions from which this correlation was developed were far from the normal evaporation situation in an ordinary evaporator. Despite this, their correlation has proven to work reasonably well for other systems and is therefore included in this work. Their correlation for predicting frictional pressure drop is as follows:

$$\left(\frac{dp}{dz} \right)_{frict} = \frac{0.092}{D^{1.2}} G^{1.8} [\mu_L - x(\mu_L - \mu_G)]^{0.2} [\nu_L + x(\nu_G - \nu_L)] \quad (4.16)$$

where ν_G and ν_L are the specific volumes of gas and liquid, respectively.

4.2.4 Thom [129]

Thom proposed a simplified scheme for the calculation of pressure drop during forced circulation of a two-phase flow of boiling water and steam. He gave curves from which frictional, accelerational, and gravitational two-phase pressure drops could be estimated from the outlet vapor quality and the operating pressure. These curves were derived using an extensive set of experimental data for steam-water pressure drops on heated and unheated horizontal and vertical tubes.

The pressure drop is given by the following expression:

$$\begin{aligned} \Delta p_{total} &= \Delta p_{static} + \Delta p_{mom} + \Delta p_{frict} = \\ &G^2 \left(\frac{1}{\rho_L} \right) r_2 + 4f_{L0} \left(\frac{L}{D} \right) G^2 \left(\frac{1}{2\rho_L} \right) r_3 + \rho_L g L r_4 \end{aligned} \quad (4.17)$$

where the values r_2 , r_3 and r_4 are determined from curves in Fig. (4.2) and the friction factor f_{L0} is obtained with Eq. (4.13).

4.2.5 Pierre [107]

Pierre measured both heat transfer and pressure drop for refrigerants evaporating in horizontal tubes. He derived an equation that would predict both the frictional pressure drop and accelerational pressure drop. From an energy equation Pierre derived the following expression for the total pressure drop:

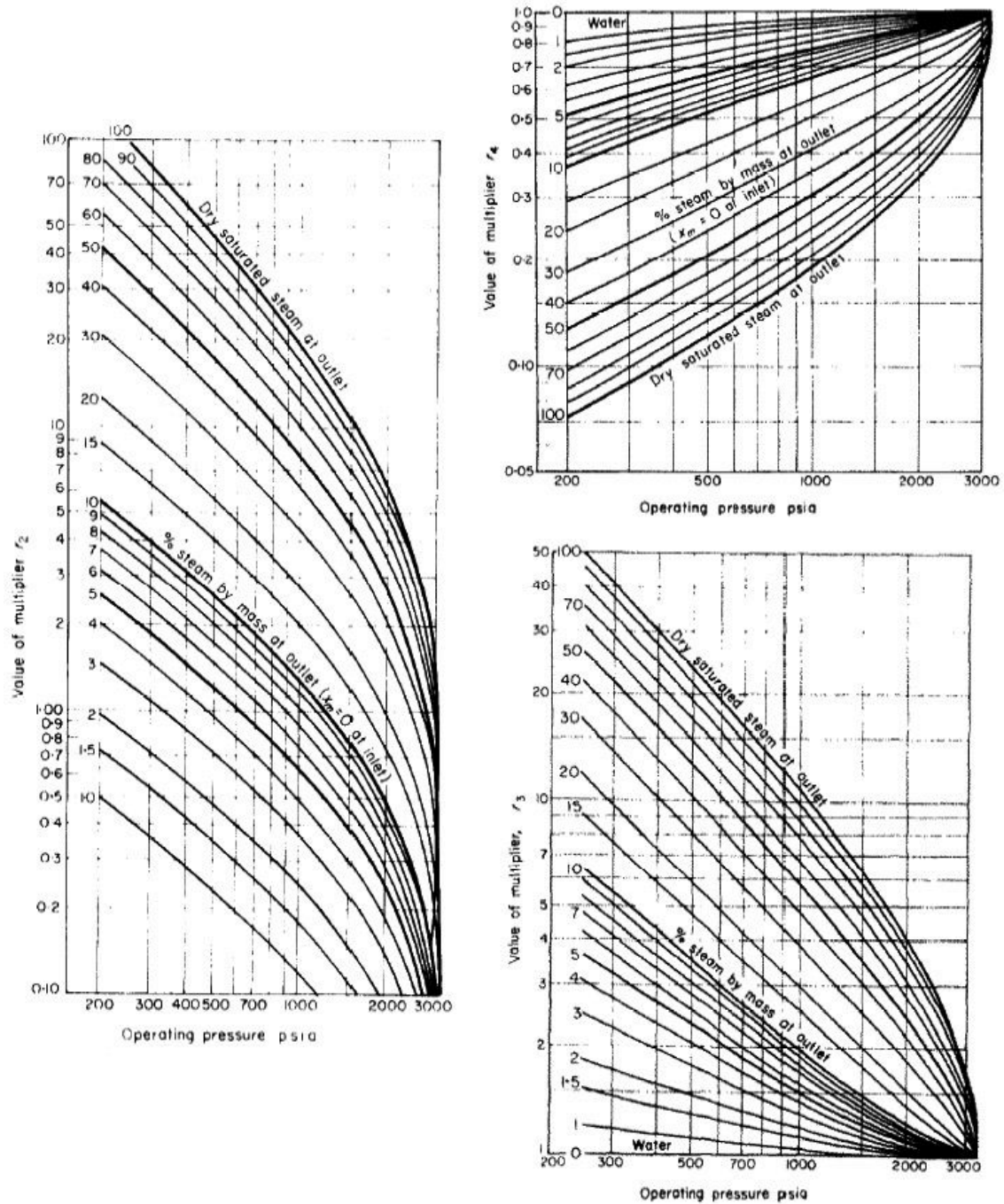


Figure 4.2: Multipliers r_2 , r_3 , and r_4 for boiling flow of water and steam (Thom 1964).

$$\Delta p_{total} = \Delta p_{frict} + \Delta p_{mom} = \left[f_{BP} + \frac{(x_{out} - x_{in})D}{xL} \right] \frac{G^2 x \nu_G L}{D} \quad (4.18)$$

The two-phase friction factor for pure refrigerant f_{BP} , valid for the case when $Re/K_f > 1$, is expressed as:

$$f_{BP} = 0.0185(K_f/Re_{L0})^{0.25} \quad (4.19)$$

where, Re_{L0} is the all liquid Reynolds number calculated using Eq. (4.13) and K_f is the Pierre boiling number defined as follows

$$K_f = \frac{\Delta x h_{LG}}{Lg} \quad (4.20)$$

4.2.6 Baroczy [11]

Baroczy described a systematic correlation for the prediction of two-phase frictional pressure drop for both single component flow and two-component flow. The correlation considered fluid properties, vapor quality and mass velocity.

The method of calculation employs two separate sets of curves. The first of these plots, Fig. (4.3), is a plot of the two-phase frictional multiplier ϕ_{fo}^2 as a function of a physical properties index $[(\mu_f/\mu_g)^{0.2}(v_f/v_g)]$ with vapor quality x as a parameter for a reference mass velocity of $1356 \text{ kg/m}^2\text{s}$.

The second, Fig. (4.4), is a plot of a correction factor Ω expressed as a function of the same physical property index for mass velocities of $339, 678, 2712$, and $4068 \text{ kg/m}^2\text{s}$ with vapor quality as a parameter. This plot serves to correct the value of ϕ_{fo}^2 obtained from Fig. (4.3) to the appropriate value of mass velocity. Thus,

$$\left(\frac{dp}{dz} \right)_{frict} = \frac{2f_{fo}G^2\nu_f}{D} \phi_{fo(G=1356)}^2 \Omega \quad (4.21)$$

where $\nu_f(\nu_L)$ and $\nu_g(\nu_G)$ are the respective vapor and liquid specific volumes and f_{fo} is obtained with Eq. (4.13).

The correlation was based on data for steam, water-air, and mercury-nitrogen for a wide range of vapor qualities and mass velocities. His method was tested against a wide range of systems including both liquid metals and refrigerants with satisfactory agreement between the measured and calculated values. This correlation has the disadvantage of being graphic in nature.

4.2.7 Chawla [27]

Chawla suggested the following method based on the vapor pressure gradient:

$$\left(\frac{dp}{dz} \right)_{frict} = \left(\frac{dp}{dz} \right)_{G0} \phi_{Chaw} \quad (4.22)$$

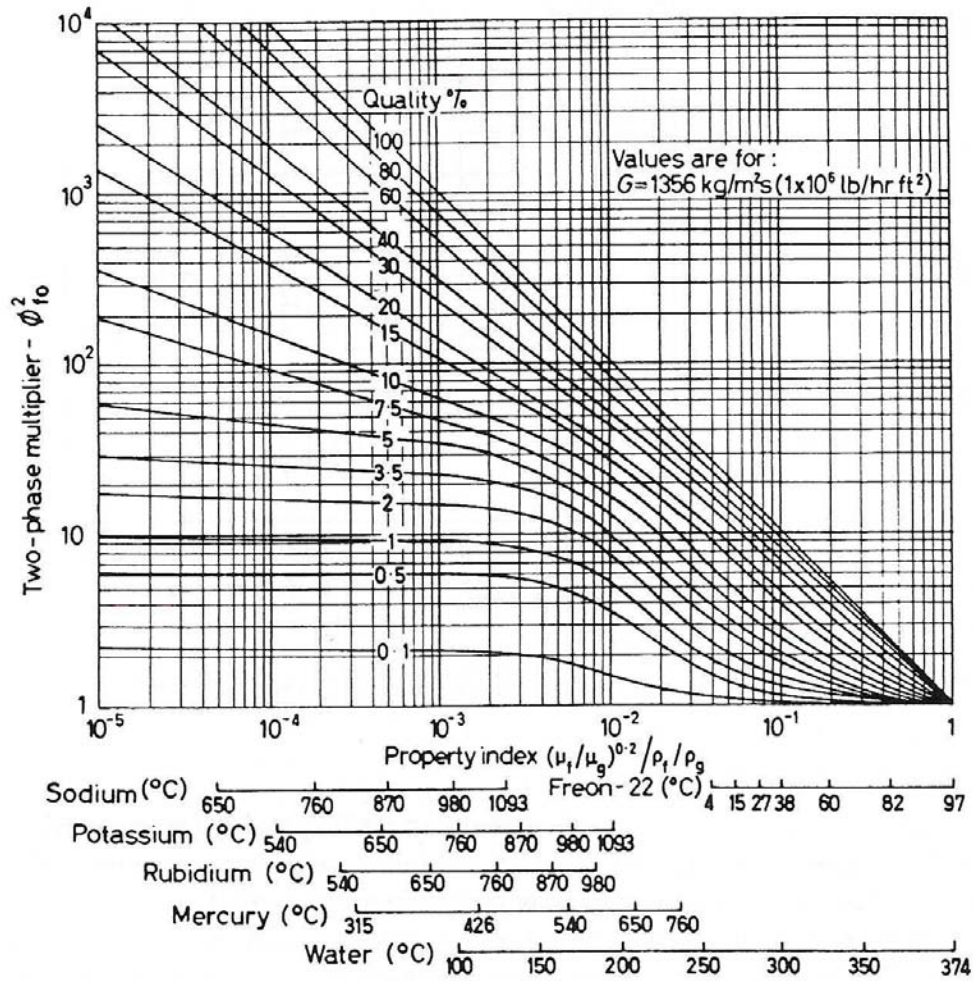


Figure 4.3: Two-phase frictional pressure drop correlation (Baroczy 1965).

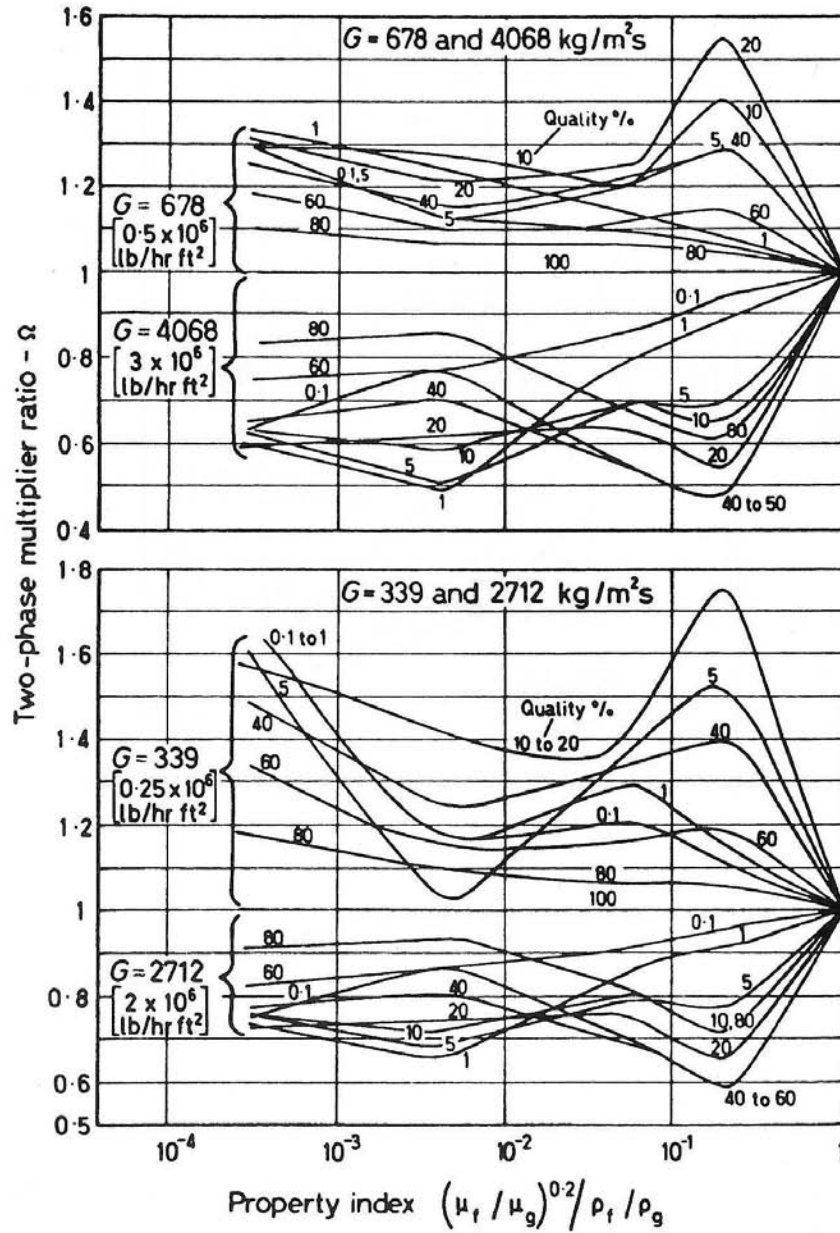


Figure 4.4: Mass velocity correction vs property index (Baroczy 1965).

The vapor frictional pressure gradient is calculated from:

$$\left(\frac{dp}{dz}\right)_{G0} = f_{G0} \frac{2G^2}{D\rho_G} \quad (4.23)$$

where the vapor friction factor f_{G0} is obtained as follows:

$$f_{G0} = \frac{0.079}{Re_{G0}^{0.25}} \quad \text{where} \quad Re_{G0} = \frac{GD}{\mu_G} \quad (4.24)$$

His two-phase multiplier is

$$\phi_{Chaw} = x^{1.75} \left[1 + S \left(\frac{1-x}{x} \frac{\rho_G}{\rho_L} \right) \right]^{2.375} \quad (4.25)$$

and his slip ratio S is:

$$S = \frac{u_G}{u_L} = \frac{1}{9.1 \left[\frac{1-x}{x} (Re_{G0} Fr_H)^{-0.167} \left(\frac{\rho_L}{\rho_G} \right)^{-0.9} \left(\frac{\mu_L}{\mu_G} \right)^{-0.5} \right]} \quad (4.26)$$

where $Re_{G0} = GD/\mu_G$ and Fr_H is determining using the following expression:

$$Fr_H = \frac{G^2}{gD\rho_h^2} \quad (4.27)$$

using the following expression to determine the homogeneous density ρ_h

$$\rho_h = \left(\frac{x}{\rho_G} + \frac{1-x}{\rho_L} \right)^{-1} \quad (4.28)$$

His method is valid for vapor qualities from $0 < x < 1$. Due to fact that this model uses the vapor phase as the starting point, it works reasonably well for high vapor qualities in the annular flow regime.

4.2.8 Chisholm [31]

Chisholm transformed the graphical procedure of Baroczy [11] to enable a more convenient application to the case evaporating turbulent flow of two-phase mixtures in smooth tubes. His two-phase frictional pressure gradient is given as

$$\Delta p_{frict} = \phi_{Ch}^2 \Delta p_{L0} \quad (4.29)$$

The frictional pressure drops for the liquid and vapor phases are calculated as follows:

$$\Delta p_{L0} = 4f_{L0} \left(\frac{L}{D} \right) G^2 \left(\frac{1}{2\rho_L} \right) \quad (4.30)$$

$$\Delta p_{G0} = 4f_{G0} \left(\frac{L}{D} \right) G^2 \left(\frac{1}{2\rho_G} \right) \quad (4.31)$$

The friction factors are obtained for turbulent flows as:

$$f_{L0} = \frac{0.079}{Re_{L0}^{0.25}} \quad \text{where} \quad Re_{L0} = \frac{GD}{\mu_L} \quad (4.32)$$

$$f_{G0} = \frac{0.079}{Re_{G0}^{0.25}} \quad \text{where} \quad Re_{G0} = \frac{GD}{\mu_G} \quad (4.33)$$

while for laminar flows ($Re < 2000$) the corresponding friction factors are calculated with the following expression:

$$f = \frac{16}{Re} \quad (4.34)$$

The flow is considered here fully turbulent at $Re \geq 2000$ to avoid an undefined transition flow interval interval in his method.

The parameter Y is obtained from the ratio of the frictional pressure drops as follows:

$$Y^2 = \frac{\Delta p_G}{\Delta p_L} \quad (4.35)$$

Then, his two-phase multiplier is determined as:

$$\phi_{Ch}^2 = 1 + (Y^2 - 1)[Bx^{(2-n)/2}(1-x)^{(2-n)/2} + x^{2-n}] \quad (4.36)$$

where n is the exponent from the friction factor expression of Blasius ($n = 0.25$).

Finally, Chisholm's parameter B is then determined following the procedure described below:

For $0 < Y < 9.5$, B is calculated as:

$$\begin{aligned} B &= \frac{55}{G^{1/2}} & \text{for} & \quad G \geq 1900 \text{ kg/m}^2\text{s} \\ B &= \frac{2400}{G} & \text{for} & \quad 500 < G < 1900 \text{ kg/m}^2\text{s} \\ B &= 4.8 & \text{for} & \quad G \leq 500 \text{ kg/m}^2\text{s} \end{aligned} \quad (4.37)$$

For $9.5 < Y < 28$, B is calculated as:

$$\begin{aligned}
B &= \frac{520}{YG^{1/2}} & \text{for } G \leq 600 \text{ kg/m}^2\text{s} \\
B &= \frac{21}{Y} & \text{for } G > 600 \text{ kg/m}^2\text{s}
\end{aligned}
\tag{4.38}$$

For $Y > 28$, B is calculated as:

$$B = \frac{1500}{Y^2 G^{1/2}} \tag{4.39}$$

Once the value of B is determined, the two-phase multiplier can be calculated and therefore the frictional pressure drop can be determined.

It is important to note that, while the procedures developed for smooth tubes gave satisfactory agreement with steam/water mixtures in vertical channels, these procedures considerably underestimated experimental air-water flow data in horizontal tubes when the mass velocity was below $700 \text{ kg/m}^2\text{s}$.

4.2.9 Friedel [46]

One of the most accurate two-phase pressure drop correlations is said to be that of Friedel. It was obtained by optimizing an equation for ϕ_{fo}^2 using a large data base of two-phase drop measurements.

This method is for vapor qualities from $0 \leq x < 1$ and utilizes a two-phase multiplier as:

$$\Delta p_{frict} = \Delta p_{L0} \phi_{fo}^2 \tag{4.40}$$

where Δp_{L0} is determined from Eq. (4.30) and the corresponding values of liquid friction factor and liquid Reynolds numbers are obtained from Eq. (4.32). His two-phase multiplier is correlated as:

$$\phi_{fo}^2 = E + \frac{3.24FH}{Fr_H^{0.045} W e_L^{0.035}} \tag{4.41}$$

where Fr_H , E , F and H are as follows:

$$Fr_H = \frac{G^2}{gD\rho_h^2} \tag{4.42}$$

$$E = (1-x)^2 + x^2 \frac{\rho_L f_{G0}}{\rho_G f_{L0}} \tag{4.43}$$

$$F = x^{0.78} (1-x)^{0.224} \tag{4.44}$$

$$H = \left(\frac{\rho_L}{\rho_G} \right)^{0.91} \left(\frac{\mu_G}{\mu_L} \right)^{0.19} \left(1 - \frac{\mu_G}{\mu_L} \right)^{0.7} \quad (4.45)$$

His liquid Weber We_L is defined as:

$$We_L = \frac{G^2 D}{\sigma \rho_h} \quad (4.46)$$

and his definition of the homogeneous density ρ_h is:

$$\rho_h = \left(\frac{x}{\rho_G} + \frac{1-x}{\rho_L} \right)^{-1} \quad (4.47)$$

The correlation is applicable to vertical upflow and to horizontal flow. This method is known to work well when the ratio $\mu_L/\mu_G < 1000$, which is the case for most working fluids and operating conditions.

4.2.10 Grönnerud [53]

This method was developed specifically for refrigerants and is as follows:

$$\Delta p_{frict} = \phi_{gd} \Delta p_{L0} \quad (4.48)$$

and his two-phase multiplier is

$$\phi_{gd} = 1 + \left(\frac{dp}{dz} \right)_{Fr} \left[\frac{\left(\frac{\rho_L}{\rho_G} \right)}{\left(\frac{\mu_L}{\mu_G} \right)^{0.25}} - 1 \right] \quad (4.49)$$

where Eq. (4.30) is used for Δp_{L0} . His frictional pressure gradient depends on the Froude number and is given as:

$$\left(\frac{dp}{dz} \right)_{Fr} = f_{Fr} [x + 4(x^{1.8} - x^{10} f_{Fr}^{0.5})] \quad (4.50)$$

When applying this expression, if the liquid Froude number $Fr_L \geq 1$, then the friction factor $f_{Fr} = 1.0$, or if $Fr_L \leq 1$, then:

$$f_{Fr} = Fr_L^{0.3} + 0.0055 \left(\ln \frac{1}{Fr_L} \right)^2 \quad (4.51)$$

where

$$Fr_L = \frac{G^2}{g D \rho_L^2} \quad (4.52)$$

The correlation of Grönnerud is applicable to vapor qualities from $0 \leq x < 1$.

In a recent experimental study, Moreno Quibén and Thome [93] compared experimental results from three different refrigerants and a wide range of operating conditions to three leading existing methods (Friedel, Grönnerud, Müller-Steinhagen and Heck) recommended by Ould Didi, Kattan and Thome [105]. Moreno Quibén and Thome showed that while all three provided a reasonable agreement at one of the mass velocities studied, they either significantly overpredicted or underpredicted the data at the other mass velocities. Also, the methods did not reliably capture the variation in two-phase frictional pressure drop versus vapor quality. Despite these drawbacks, the Grönnerud method was found to provide the most accurate predictions.

4.2.11 Müller-Steinhagen and Heck [97]

This method [97] proposed a two-phase frictional pressure gradient correlation that is in essence a clever empirical interpolation between all liquid flow and all vapor flow:

$$\left(\frac{dp}{dz}\right)_{frict} = F(1-x)^{1/3} + Bx^3 \quad (4.53)$$

where the factor F is

$$F = A + 2(B - A)x \quad (4.54)$$

The factors A and B are the frictional pressure gradients for all liquid $(dp/dz)_{L0}$ and all vapor $(dp/dz)_{G0}$ flow and are defined as:

$$\left(\frac{dp}{dz}\right)_{L0} = f_{L0} \frac{2G^2}{D\rho_L} \quad (4.55)$$

$$\left(\frac{dp}{dz}\right)_{G0} = f_{G0} \frac{2G^2}{D\rho_G} \quad (4.56)$$

The friction factors are obtained with Eqs. (4.32) and (4.33).

This new correlation for the prediction of frictional pressure drop for two-phase flow in pipes is simple and more convenient to use than other methods. To determine their reliabilities, the authors checked the present correlation, as well as fourteen correlations from the literature, against an extensive data bank with measurements of frictional pressure drop in pipes. They found that the best agreement between predicted and measured values was obtained by the correlation of Bandel [8] which, however, is quite complex to implement and use. The correlation suggested in their paper still predicted the frictional pressure drop with reasonable accuracy. It includes single-phase liquid and gas pressure drops and predicts correctly the influence of flow parameters.

4.3 Analytical methods

Two-phase pressure drop models developed following this approach are general models since no empirical information is used in their development. Besides this obvious positive aspect, the corre-

sponding mathematical models are very complex and often iterative and numerical procedures are required resulting in time consuming calculations.

Several two-phase pressure drop models developed following this approach can be found in literature. Nevertheless the complete set of equations describing these models, as well as the complex resolutions procedures, will not be given in this section due to their size.

4.4 Phenomenological methods

Two-phase pressure drop models developed following a phenomenological approach are theoretical based methods as the interfacial structure is taken into account. Thus, they are not blind to the different flow regimes resulting in general applicability models. Despite this obvious advantage, an important drawback of this approach is that some empiricism is still required in order to close these models and be able to solve for the two-phase frictional pressure gradient. Another important aspect is that no general flow pattern based model is yet available. In fact, they are only available for individual flow patterns or flow structures. This observation precludes one of the major difficulty in following this approach, that is they need a very reliable flow pattern map in order to be able predict the different interfacial structures.

In what follows in this section, the existing two-phase pressure drop models developed pursuing this approach are presented and critically reviewed.

4.4.1 Bandel [8]

Bandel assumed that the pressure drop is dependent only upon three different flow regimes, the annular flow regime, the stratified flow regime and the transitional flow regime. He derived an iterative procedure to calculate the frictional pressure drop for the annular flow regime and the stratified flow regime. In these iterative procedures conditions for the different flow regimes were set up, and from these conditions the flow regime was determined. If the flow is within the transitional region, the pressure drop is determined via an interpolation from the results of the annular and the stratified flow calculations.

The complete set of equations will not be given here due to their complexity and length but the calculating procedure is given in a simple form in the paper by Müller-Steinhagen and Heck [97].

4.4.2 Beattie and Whalley [14]

Beattie and Whalley proposed a theoretically based flow pattern dependent calculation method. In fact, they adapted an existing mixing-length theory model of two-phase pressure drop (Beattie [13]) to give a simple calculation method, of the same form as that used for single-phase flow, in which flow pattern influences are partially allowed for in an implicit manner and therefore need not be explicitly taken into account when using the method. They postulated that if it is assumed that coefficients appearing in mixing-length theory are the same as those in the single-phase application of the theory, loss of generality occurs. However the familiar Colebrook-White equation relating friction factor f , Reynolds number Re , and surface roughness/diameter ratio k/D :

$$\frac{1}{\sqrt{f}} = 3.48 - 4 \log \left[\frac{2k}{D} + \frac{9.35}{Re\sqrt{f}} \right] \quad (4.57)$$

remains valid for many two-phase situations provided flow pattern effects are considered in the definition of the friction factor and Reynolds number. For Re and f they used the same definitions as in the homogeneous model:

$$\left(\frac{dp}{dz} \right)_{frict} = \frac{2fG^2}{\bar{\rho}D} \quad (4.58)$$

$$Re = \frac{GD}{\mu} \quad (4.59)$$

and $\bar{\rho}$ is the homogeneous density given by:

$$\bar{\rho} = \left(\frac{x}{\rho_G} + \frac{1-x}{\rho_L} \right)^{-1} \quad (4.60)$$

They proposed the following hybrid definition for the viscosity μ , allows flow pattern influences to be taken into account

$$\mu = \mu_L(1 - \beta)(1 + 2.5\beta) + \mu_G\beta \quad (4.61)$$

where β is the homogeneous void fraction defined as:

$$\beta = \frac{\rho_L x}{\rho_L x + \rho_G(1 - x)} \quad (4.62)$$

A special feature of this model is the use of Eq. (4.57) for all values of Re , even for those where single-phase behaviour would suggest its replacement by a laminar flow relation. This is because turbulent-like characteristics can extend to very low Reynolds numbers in two-phase flows. This is not surprising because even in the absence of turbulence, Reynolds stresses can be expected in two-phase flows due to the interaction of gas-liquid interfaces with the flow field. The authors compared their method to an extensive adiabatic round tube data bank and it showed to be, despite its simplicity, as good as most alternative, more complex methods.

4.4.3 Hashizume et al. [61]

Based on experimental two-phase flow refrigerant data in a horizontal pipe, Hashizume [60] proposed a modified version of Baker flow pattern map. The boundaries for the flow transitions in their modified version were approximated by the following correlations:

$$\text{Stratified to wavy: } Y = [(13.6X^{-0.1776})^{-1} + (972X^{-1.429})^{-1}]^{-1} \quad (4.63)$$

$$\text{Wavy to slug: } Y = 972X^{-1.429} \quad (4.64)$$

$$\text{Wavy to annular: } Y = 28.05X^{-0.1436} \quad (4.65)$$

Here, X, Y, λ and ψ' are

$$X = \frac{(1-x)}{x} \lambda \psi' \quad (4.66)$$

$$Y = \frac{Gx}{\lambda} \quad (4.67)$$

$$\lambda = \left[\left(\frac{\rho_G}{\rho_{AA}} \right) \left(\frac{\rho_L}{\rho_{WA}} \right) \right]^{1/2} \quad (4.68)$$

$$\psi' = \left(\frac{\sigma_{WA}}{\sigma_L} \right)^{1/4} \left[\left(\frac{\mu_L}{\mu_{WA}} \right) \left(\frac{\rho_{WA}}{\rho_L} \right)^2 \right]^{1/3} \quad (4.69)$$

where σ represents the surface tension and the subscripts AA and WA denote the air and water at ambient conditions, respectively. A graphical version of this modified Baker map was already introduced in Chapter 2.

The authors argued that typical flow patterns in horizontal two-phase flow are annular and stratified. On this basis, simplified models for annular and stratified flow were proposed. Since both configurations consist of a continuous liquid (film) flow and a gas (core) flow, and their both have a free surface as a boundary, their characteristics were supposed to be different from those of single-phase flow. In fact, the corresponding velocity profiles were described with the Prandtl mixing theory. From this analysis, and once the flow pattern configurations were determined using the proposed map, the frictional pressure drop for both types of regimes were determined. The intermediate region, i.e. wavy flow, was interpolated between annular and stratified flow. The proposed simplified models for annular and stratified flows are presented below.

Annular flow

The proposed simplified model for annular flow consisted of a liquid film and a gas core. Entrainment was neglected and the liquid film was assumed to be smooth and have uniform thickness in the circumferential direction. With these assumptions and the mentioned mixing length theory, the following equations were deduced:

$$\frac{1}{4} Re_L = \int_0^{Re^+/2} u^+ dy^+ \quad , \text{ for liquid phase} \quad (4.70)$$

$$\frac{1}{4} Re_L \frac{x}{1-x} \Gamma = \int_{\delta^+}^{Re^+/2} \left(1 - \frac{2y^+}{Re^+} \right) u^+ dy^+ \quad , \text{ for gas phase} \quad (4.71)$$

the two unknowns Re^+ and δ^+ can be solved for given values of $Re_L (= G(1-x)D/\rho_L)$, x and $\Gamma (= \rho_L/\rho_G)$ using an iterative procedure. The frictional Reynolds number Re^+ and dimensionless liquid film thickness δ^+ definitions are:

$$Re^+ = \frac{\rho_L u^* D}{\mu_L} \quad (4.72)$$

$$\delta^+ = \frac{\rho_L u^* \delta}{\rho_L} \quad (4.73)$$

Here, u^* is the friction velocity $u^* = \sqrt{g\delta}$, u^+ is the dimensionless velocity $u^+ = u/u^*$, and y^+ dimensionless distance $y^+ = \rho_L u^* y / \rho_L$.

Once Re^+ value is known from the equations above, the pressure drop can be obtained from the relationship between wall shear stress and pressure drop:

$$\frac{dp}{dz} = \frac{4}{D} \tau_w = \frac{4(Re^+)^2 \mu_L^2}{\rho_L D^3} \quad (4.74)$$

Stratified flow

In the same way as for annular flow, Re^+ and δ^+ can be calculated from Eqs. (4.70) and (4.71) for given values of Re_L , x and Γ .

In the case of stratified flow, flow in the pipe was modeled as flow between two parallel plates. Therefore, the relationship between the distance between the upper and lower plates D_e and the pipe diameter D has to be found. Comparison was made with experimental data on refrigerants in the stratified region, presented in Hashizume [60], to seek a suitable equivalent value with which the analytically obtained pressure drop agreed with experimental data. The following expression was found:

$$\frac{D_e}{D} = [(x^{5.0/\Gamma})^{-2} + (1.22x^{-1.42})^{-2}]^{-0.5} \quad (4.75)$$

Transition flow

The variation of pressure drop versus mass flux under a constant quality showed characteristic slopes on a log log plot. Each of these slopes corresponds to stratified, transient and annular flow. Therefore, the expression below was proposed to calculate pressure drop in the transient region by interpolation between stratified and annular flow

$$\left(\frac{dp}{dL}\right)_{transient} = \left(\frac{dp}{dL}\right)_{SC} \left(\frac{G}{G_{SC}}\right)^{\log[(dp/dL)_{AC}/(dp/dL)_{SC}] \log[G_{AC}/G_{SC}]} \quad (4.76)$$

where the subscripts SC and AC denote the critical values (at fixed vapor quality) for stratified and annular flow. To predict G_{SC} and G_{AC} the modified Baker map is used.

Comparisons of this analysis with existing experimental data on refrigerants showed good agreement.

4.4.4 Olujić [104]

Olujić proposed a general correlation based on the fact that in horizontal two-phase flow two extremely different flow regimes exist: a β region, in which the velocities of the two phases are nearly equal (bubble and plug flow), and an α region, in which the velocity of the gas phase is higher than that of the liquid phase (wavy, slug and annular flow). In his approach, separate

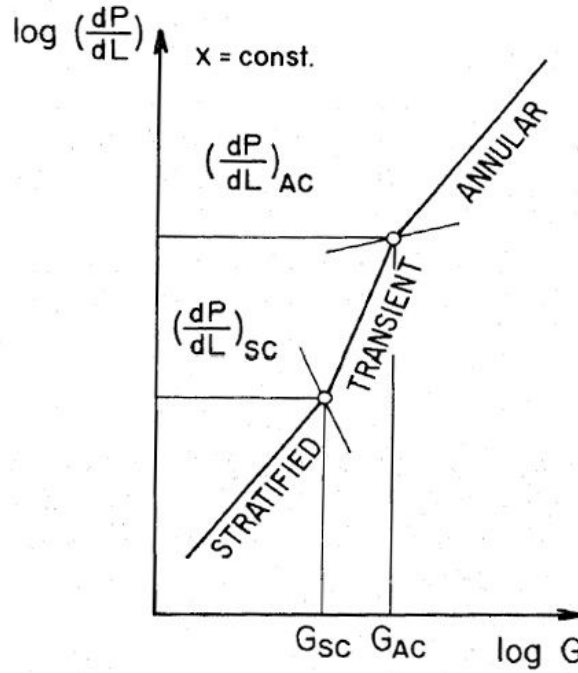


Figure 4.5: Linear interpolation for transient flow (Hashizume 1985).

correlations were developed for the two regions, with the demarcation of the valid range expressed in terms of a relationship for the ratio of phase-volume flow rates, and a dimensionless ratio containing a modified Froude number.

Pressure drop in β -region:

In the range of low quality flow, where the average liquid velocity, u_L , is approximately equal to the average gas velocity, u_G , the simplest approach is to consider the gas-liquid mixture to be a homogeneous flow. However, the simple homogeneous model does not ensure accurate predictions of frictional pressure drop. Hence, he used the following expression:

$$\frac{(dp/dz)_{fric,\beta}}{(dp/dz)_{fric,h}} = [1 - x(R - 1)(K_2 - 1)] \quad (4.77)$$

The homogeneous frictional pressure drop $(dp/dz)_{fric,h}$ is calculated from:

$$(dp/dz)_{fric,h} = f \left(\frac{G^2}{2D\rho_L} \right) [1 + x(R - 1)] \quad (4.78)$$

where R is the density ratio of the phases $R = \rho_L/\rho_G$, and f is the Darcy friction factor for smooth and rough tubes estimated from:

$$f = \left\{ -2 \log \left[\frac{k/D}{3.7} - \frac{5.02}{Re} \log \left(\frac{k/d}{3.7} + \frac{14.5}{Re} \right) \right] \right\} \quad (4.79)$$

Here, k/D = relative roughness; $Re = GD/\mu_{tp}$; and $\mu_{tp} = \mu_L[1 - x(1 - \theta)]$ with $\theta = \mu_L/\mu_G$.

The parameter K_2 in Eq. (4.77) is determined from

$$K_2 = 1.2 \frac{(7 + 8n)(7 + 15n)}{(7 + 9n)(7 + 16n)} \quad (4.80)$$

where n is calculated using

$$n = (0.617/\beta)[1 + (1 + 0.907\beta)^{1/2}] \quad (4.81)$$

and β is the volume-flow ratio of the phases

$$\beta = \frac{\rho_G \dot{M}_G}{\rho_L \dot{M}_L} \quad (4.82)$$

Pressure drop in α -region:

In the range $u_G \gg u_L$, the frictional pressure drop, as well as the void fraction, is affected by the momentum exchange between the phases. For this region the proposed correlation is:

$$(dp/dz)_{fric,\alpha} = (dp/dz)_{SG} \left[1 + \frac{(1-x)}{xR\epsilon_T} \right]^{19/8} \quad (4.83)$$

where the superficial frictional gas pressure drop $(dp/dz)_{SG}$ is calculated as follows:

$$(dp/dz)_{SG} = f \left[\frac{(Gx)^2}{2D\rho_G} \right] \quad (4.84)$$

where the parameter ϵ_T is determined from the following equations:

$$\epsilon_T = (\epsilon_1^{-3} + \epsilon_2^{-3})^{-1/3} \quad (4.85)$$

$$\epsilon_1 = 0.77R^{-0.55} \Gamma^{(0.266R^{0.057})} \quad (4.86)$$

$$\epsilon_2 = 2.19R^{-0.61} \Gamma^{(1.78R^{0.078})} \quad (4.87)$$

$$\Gamma = \left(\frac{1-x}{x} \right) \left[\frac{G^2(1-x)^2}{\rho_L^2 g D} \right] \left(\frac{\rho_L}{\rho_G} \right)^{-1/2} \left(\frac{\mu_L}{\mu_G} \right)^{-1/8} \quad (4.88)$$

$$R = \frac{\rho_L}{\rho_G} \quad (4.89)$$

The proposed method was compared with experimental data from different sources. In general, the predictions agreed well with a variety of published data for adiabatic gas-liquid flows in horizontal pipes.

4.4.5 ARS Model [58]

Hart, Hamersma and Fortuin [58] presented a phenomenological model, called ARS (Apparent Rough Surface), to calculate the value of the frictional pressure drop in gas-liquid pipe flow with a small liquid holdup, $\epsilon_L < 0.06$ ($\epsilon > 0.94$), covering the stratified, wavy and annular flow regimes. For this kind of flow it was shown that liquid, flowing along the tube wall, may be considered as a local roughness over a fraction $\theta = \alpha/2\pi$ of the tube wall, see Fig. (4.6). The interfacial shear stress τ_i exerted by the gas on the liquid film may be considered as shear stress exerted by the gas phase on a rough wall.

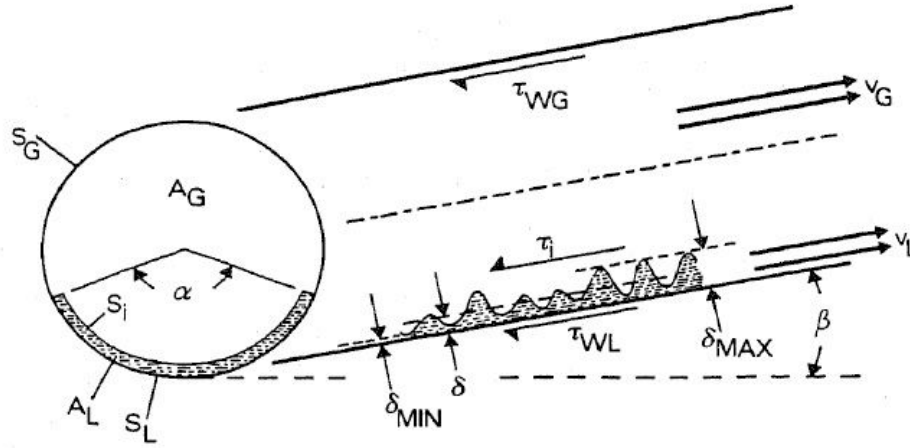


Figure 4.6: Schematic representation of gas-liquid flow with a small liquid holdup ϵ_L in straight smooth tubes (ARS 1989).

These assumptions led to the following correlation for the two-phase pressure drop ΔP_{TP} :

$$\Delta P_{TP} = 4f_{TP} \left(\frac{L}{D} \right) \frac{1}{2} \rho_G u_G^2 \quad \text{for } u_G \gg u_i \quad (4.90)$$

where f_{TP} is the two-phase friction factor and u_G is the vapor mean velocity defined in Chapter 2.

The complete procedure for the calculation of f_{TP} and afterwards ΔP_{TP} is as follows:

1. The value of the liquid holdup ϵ_L is calculated from:

$$\frac{\epsilon_L}{1 - \epsilon_L} = \frac{j_L}{j_G} \left\{ 1 + \left[10.4 Re_{SL}^{-0.363} \left(\frac{\rho_L}{\rho_G} \right)^{1/2} \right] \right\} \quad (4.91)$$

where superficial velocities j_G and j_L are calculated from Eqs. (2.9) and (2.10) introduced in Chapter 2 and $Re_{SL}(= j_L D / \mu_L)$ is the liquid Reynolds number based on superficial liquid velocity.

2. Vapor mean velocity u_G and liquid mean velocity u_L are calculated using Eqs. (2.5) and (2.6).
3. Modified Fr and the Re of the gas phase are calculated with

$$Fr = \frac{u_L^2 \rho_L}{gD(\rho_L - \rho_G)} \quad Re_G = \frac{u_G D}{\mu_G} \quad (4.92)$$

4. The value of the wetted wall fraction θ is calculated by means of the following correlation:

$$\theta = \theta_o + 0.26Fr^{0.58}, \quad \text{in which } \theta_o = 0.52\epsilon_L^{0.374} \quad (4.93)$$

If $\theta > 1$ then $\theta = 1$.

5. Apparent relative roughness of the liquid film k/D is determined from:

$$\frac{k}{D} = 2.3 \left(\frac{\delta}{D} \right) \simeq 2.3 \left(\frac{\epsilon_L}{4\theta} \right) \quad (4.94)$$

6. Interfacial friction factor f_i is calculated with

$$f_i = \frac{0.0625}{\left[\log \left(\frac{15}{Re_G} + \frac{k}{3.715D} \right) \right]^2} \quad (4.95)$$

7. The value of the single-phase friction factor f is calculated with

$$f_G = \frac{0.07725}{\left[\log \left(\frac{Re_G}{7} \right) \right]^2} \quad (4.96)$$

which is valid for $2100 < Re_G < 10^8$.

8. The two-phase friction factor f_{TP} is calculated from proration of the respective wet and dry perimeters as

$$f_{TP} = (1 - \theta)f + \theta f_i \quad (4.97)$$

9. Finally, the value of the two-phase pressure drop ΔP_{TP} is calculated with Eq. (4.90).

This model has been verified with experimental data. These data refer to steady-state gas-liquid flow through horizontal straight smooth tubes and have been obtained both from the literature and from authors' own experiments.

4.5 Conclusions

Existing two-phase pressure drop model have been presented and critically reviewed. The models were classified according to the different approaches used for their development, that is empirical, analytical and phenomenological. The main advantages and disadvantages of those approaches and methods were emphasized. While empirical based model are the easiest to implement and provide a reasonable accuracy within the range of database used in their implementation, their reliability seemed to be the weakness link due to the amount of empirical information used. In contrast, the analytical approach provides general models, since no empirical information is used, but their implementation is very complex and time consuming just to do one calculation. A good compromise between purely empirical and purely analytical seems to be the phenomenological approach. This later preserves their general applicability, as they are theoretically based, and introducing some empiricism they overcome complex calculations resulting in somewhat easy to use models. Despite this, one needs to know in advance the interfacial structure, introducing the need of a reliable flow pattern map to allow the prediction of flow patterns or flow regimes. Apparently, no flow pattern based two-phase frictional pressure model that covers the important flow regimes occurring in horizontal refrigerant evaporator tubes, is available in the literature. Thus, this proves the analytical objective of the present work.

Chapter 5

Description of Experimental Test Facility

The existing LTCM intube refrigerant test loop has been modified and adapted to the new test conditions and measurement methods. Two new test sections have been successively implemented into the modified test rig. In order to determine pressure drop separately for the different flow regimes, the new test sections consist of both diabatic and adiabatic zones. The present configuration allows tests to be run under diabatic and adiabatic conditions simultaneously. All modifications have been made on the original test rig developed by Kattan [75] and modified afterwards by Zürcher [162].

5.1 General description

The objective of the experimental part of this study was to run in-tube evaporation tests over a wide range of experimental conditions in order to obtain accurate values of two-phase pressure drops. The ranges of the experimental conditions are shown in Table (5.1).

Experimental test conditions	
Test fluids	R134a, R22, R410A
Saturation temperature (T_{sat})	5°C
Internal diameter (d)	8.00, 13.8 mm
Vapor quality (x)	0 – 1.0 [–]
Mass velocity (G)	70 – 700 kg/m ² s
Heat flux (q)	6.0 – 57.5 kW/m ²

Table 5.1: Experimental conditions for in-tube evaporation tests.

The existing LTCM test loop, developed by Kattan [75] and modified afterwards by Zürcher [162], has been adapted to be able to run tests over a wide range of test variables. Two new test sections have also been implemented into the modified test rig. The new configuration results in very accurate values of two phase pressure drops. The test facility consists of a refrigerant circuit and a heating water circuit. An overall view of the modified test facility is shown in Fig. (5.1).

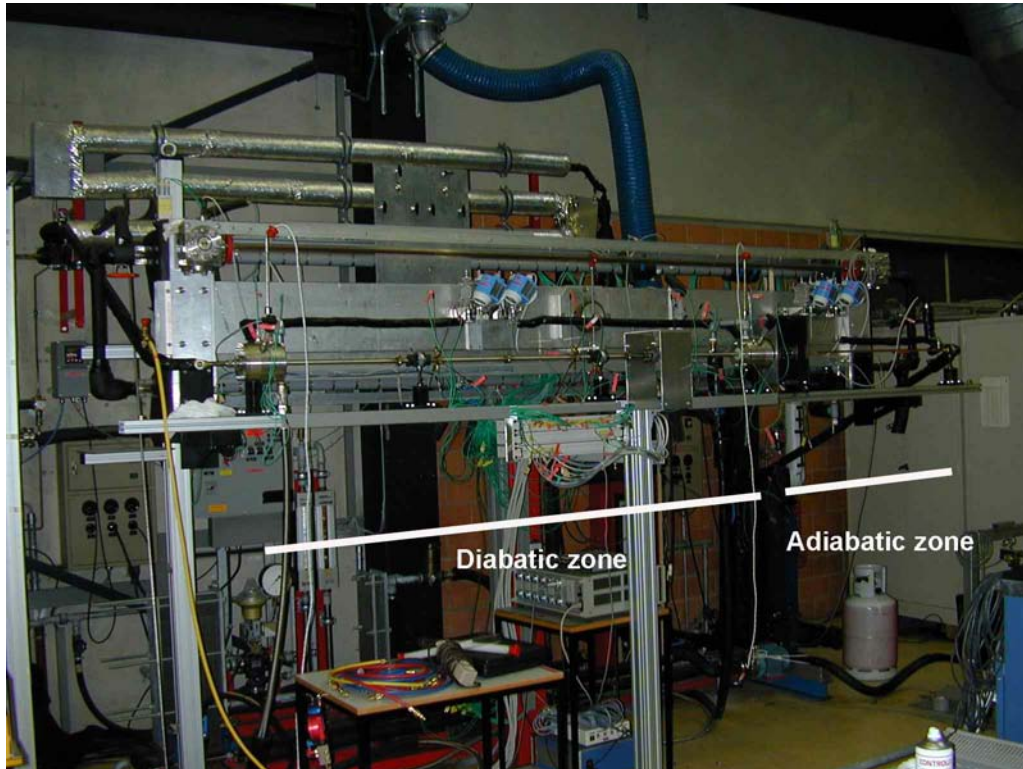


Figure 5.1: Overall view of the modified test facility including the new two-zone test section.

5.2 Refrigerant circuit

A schematic of the refrigerant circuit is depicted in Fig. (5.2). The refrigerant passes first through a series of electrical preheaters and then through an insulated tube before it enters the two zone test section. In the first zone (called diabatic zone) refrigerant is heated by a counter-current flow of hot water in the annulus of the double pipe system. Then, refrigerant passes through a visualization zone and through the second part of the test section (called diabatic zone) where no heat is added to or removed from the refrigerant. Refrigerant exits the test section and goes through a condenser, a magnetically driven gear type pump and finally a Coriolis mass flow meter. The refrigerant circuit also includes a vapor-liquid reservoir for controlling the amount of refrigerant circulating in the test rig and thus the operating pressure.

A particularly detailed description of the new two-zone test section is given in Section (5.4) in this chapter, while a description of other main components of the refrigerant circuit are given below:

Preheater

The electrical preheater is made of six horizontal stainless steel tubes. Internal and external diameters of the tubes are 13 mm and 16 mm , respectively. The length of each tube is 1.40 m and a 3 mm diameter and 10 m long hot wire is coiled around the tube. The total maximum heat flux provided by the preheater is 61.2 kW/m^2 . Thermocouples are installed on each tube to prevent operation from reaching the critical heat flux (CHF).

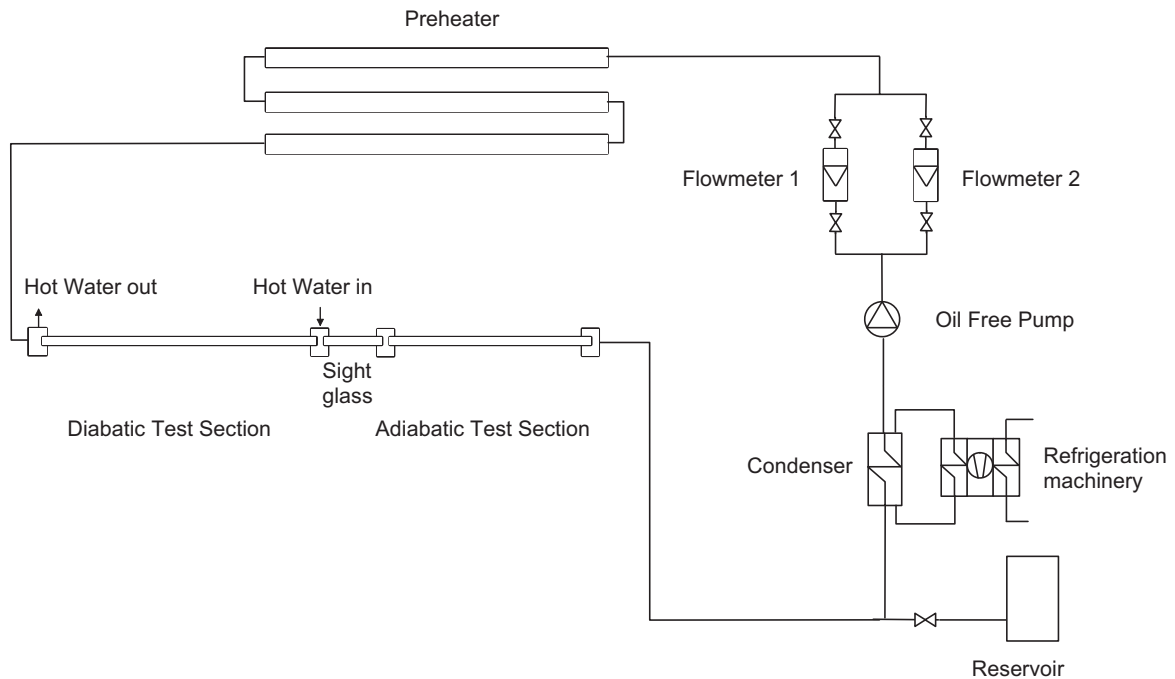


Figure 5.2: Schematic of the refrigerant circuit.

Condenser

Refrigerant is condensed and subcooled by means of a stainless-steel shell and tube condenser. Condensation takes place inside the tubes and the chilled liquid receives the heat. The condenser is composed of 165 stainless steel tubes of 1.5 m length. External and internal tube diameters are 6.35 mm and 4.55 mm, respectively. The total area of heat exchange is 5 m².

Gear pump

To avoid the presence of oil in the experimental test rig, a magnetic drive gear pump has been used. Both gears are made of nickel-molybdenum-chromium alloy compatible with refrigerants used during the experimental campaign. The pump provided stable flow in the range from 0.15 kg/min to 10 kg/min. The regulation of the flow can be done either by a by-pass around the pump or by pump motor frequency variation.

Flow meters

Two Coriolis type flow meters were installed on the modified test rig. The two flow meters are fixed securely to the wall to insure steady measurement conditions. A selection of valves allowed switching between them depending on operating flow rates. The nominal measurement points are 1.5 kg/min and 10 kg/min for the small and big flow meter, respectively. The accuracy of the flow meters is 0.15% of the measured value. The channels connecting the pump to the flow meter and flow meter to the preheater are heavily insulated to avoid heat gain from the surroundings.

5.3 Hot water circuit

A schematic of the hot water circuit is depicted in Fig. (5.3). The hot water circuit reheats water after it passes through the diabatic zone of the two-zone test section. The hot water flows counter currently to the refrigerant in the annulus of the diabatic zone of the test section. The water flow rate is measured by a Coriolis flow meter and the water is circulated by a stainless steel pump. The operating pressure of water flow is fixed to 2 bars. The inlet water temperature (which determines heat flux) is controlled by two secondary water circuits using two plate heat exchangers connected to an industrial cold water circuit. To insure the mixing of the heating water in the annular chamber, the laminar condition has been avoided. The Reynolds number of flowing water was always higher than 4500 for the experimental conditions described in Table (5.1).

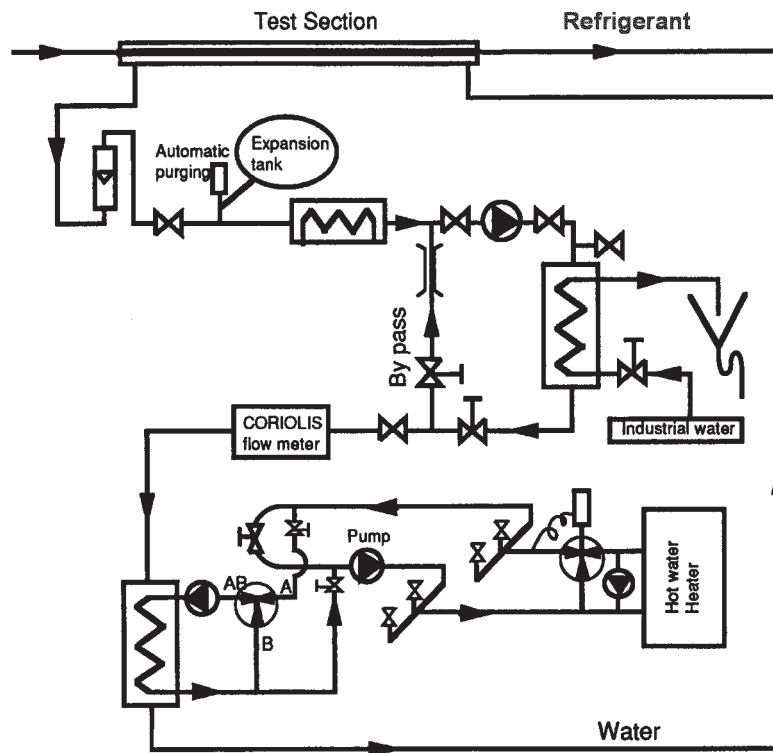


Figure 5.3: Schematic of the hot water circuit ([75]).

5.4 Test sections

Two test sections have been constructed and implemented into the modified test rig. Each test section consists of two separate zones called diabatic and adiabatic, respectively. In the first zone of the test section (diabatic zone), refrigerant is heated by a counter-current flow of hot water in the annulus of the double pipe system. In the second zone of the test section (adiabatic zone) no heat is added or removed from the refrigerant. Both test sections were made of copper and have plain smooth interiors. Internal diameters were 8.00 mm (TS1) and 13.8 mm (TS2), respectively. The outer stainless steel annulus has an internal diameter of 14.00 mm for TS1 and 20.00 mm for TS2. The internal tubes (only diabatic zone) are perfectly centered within the outer annulus tube

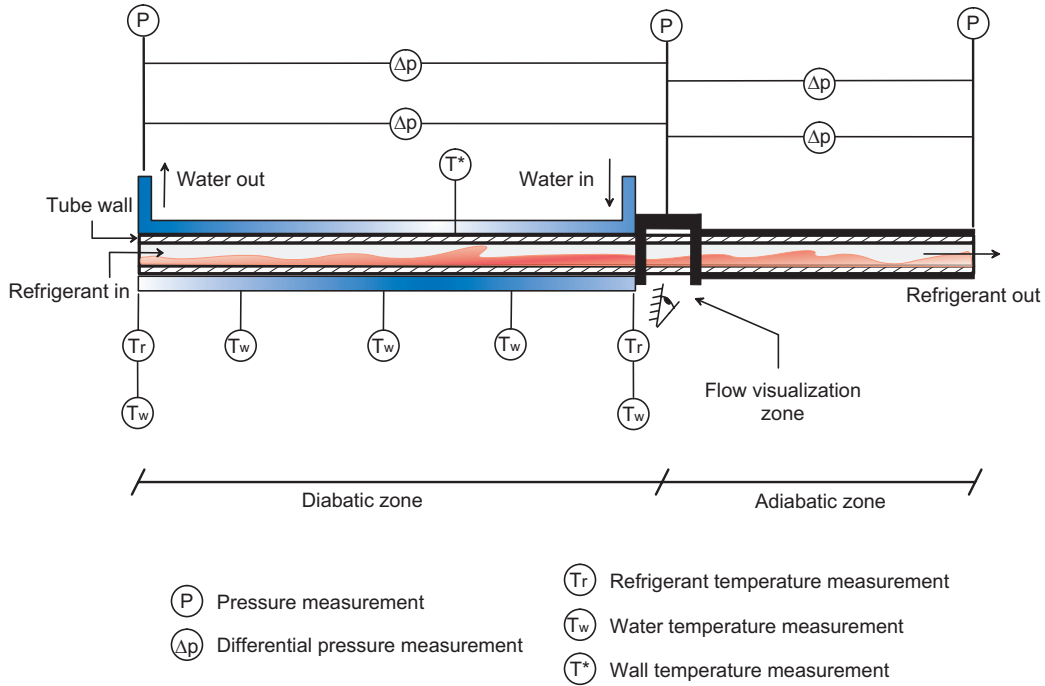


Figure 5.4: New two-zone test section.

in five positions using centering screws. The external surfaces of both zones of the test section were heavily insulated to avoid heat gain from surroundings. The main physical properties and geometrical dimensions of the implemented test sections are shown in Table (5.2), where: D is the internal diameter of the tube, D_{ext} is the external diameter of the tube, $z_{diab.}$ is the length of the diabatic zone, $z_{adiab.}$ is the length of the adiabatic zone, λ is the thermal conductivity and δ_{wat} is the annular gap for the heating water in the diabatic zone.

	Internal tube						External tube			
	Mat.	D_{ext}	D	$z_{diab.}$	$z_{adiab.}$	λ	Mat.	D_{ext}	D	δ_{wat}
		[mm]	[mm]	[mm]	[mm]	[W/m ² K]		[mm]	[mm]	[mm]
TS1	Cu	9.53	8.00	2035	980	339	SS	17.40	14.00	2.235
TS2	Cu	15.87	13.8	2026	989	339	SS	23.00	20.00	2.065

Table 5.2: Main properties and geometrical dimensions of the implemented test sections.

A schematic of the two-zone test section is depicted in Fig. (5.4). Refrigerant flows into the internal tube from left to right, and hot water flows counter-currently into the annulus from right to left.

5.5 Experimental procedure and data acquisition

All the measurements are made with a computer equipped with a data acquisition system. The data acquisition system is a National Instruments SCXI. The acquisition card is a PCI MIO 16XE 50 installed in the computer. The resolution of this card is 16 bits and the maximum acquisition frequency on a single channel is 10 kHz . A SCXI 1000 module with four bays is connected to this card. Each of the four bays has a 32 channel voltage measurement card (type 1102). The total number of acquisition channels is thus 128. Each channel has a computer programmable gain: 1 for 0 to 10 V signal (pressure transducer and mass flow meter) and 100 for low voltage signal (thermocouples). The signals can be adjusted to the 0 to 10 V range of the acquisition card in the computer. A 2 Hz low pass frequency filter is also included in the card for each channel. This helps to diminish the measurement noise and does not affect the steady-state measurement. At the end of the acquisition chain, a terminal block with 32 sockets is connected to the 1102 card. Each card has its own terminal block. The cold junction for every thermocouple is made in this terminal block at the socket. The material for this socket is copper for both poles (+ and -), the continuity of the two different specific materials of the thermocouple is then broken at this point located inside the terminal block. The temperature of the 32 cold junctions is maintained uniform with a metallic plate and is measured via a RTD installed in the middle. Additionally, all the terminal blocks are placed in a close cupboard away from external thermal influences.

In order to measure a test parameter in a channel, 100 acquisitions are made in 0.02 s (50 Hz electrical period) and the average of these 100 values is calculated during the acquisition. The result is the measured value of the channel. By this way, the noise from alternating current on the measured signal is removed. This value is stored and the system goes to the next channel. With this measurement method, the theoretical channel measurement frequency is 50 channels per second, but due to the switching time between channels, the actual frequency is 30 channels per second. In total, it takes 4.3 s to measure all the channels of the acquisition system once. To obtain one experimental point, 10 of such acquisition cycles are recorded and averaged.

5.6 Measurements

The major objective of the experimental part of this work was to measure two-phase pressure drops over the vapor quality range from 0 to 1. Two-phase pressure drop values were directly obtained from the differential pressure transducers. Meanwhile to completely establish the experimental conditions, some others parameters need to be determined by calculation from measured values.

5.6.1 Pressure drop

The two-phase pressure drops across the diabatic test sections were each measured by a selection of sensors depending on the level of the pressure drop being measured. For the diabatic test section two differential pressure transducers ($0 - 40\text{ mbar}$ and $0 - 500\text{ mbar}$) were used for the small and intermediate pressure drops and a pair of absolute pressure sensors for pressure drops larger than 500 mbar . For the adiabatic test section, two differential pressure transducers ($0 - 20$ and $0 - 160\text{ mbar}$) were used.

5.6.2 Refrigerant temperature

The saturation temperature of the refrigerant T_{sat} was calculated using the the pressure measurements at the inlet and outlet of the diabatic part of the test section and by the assumption of a linear pressure distribution over the length of the diabatic test section as is typical in such tests. Then, knowing the saturation pressure P_{sat} the saturation temperature is obtained based on the thermodynamical properties calculated using EES (linked to REFPROP 6.0 of NIST).

5.6.3 Heat Flux

Heat is transferred from the hot water to the refrigerant. The temperature of the water is measured at five positions (represented as T_w in Fig. (5.4)) with a total of 26 thermocouples giving five local water temperature values T_w . The enthalpy of the flowing water, assuming that the pressure drop along the annulus is negligible is given for any location along the heated tube by the following equation:

$$h_w = c_{p_{water}} T_w \quad (5.1)$$

From Eq. (5.1), five discrete enthalpy values were obtained from the five water temperature measurement points. These points were used to determine the enthalpy profile over the diabatic test section. For the enthalpy profile determination, a second order polynomial fit has been used.

Then, the heat transferred from the water between two points of the test section can be defined as:

$$Q_{12} = (h_{w2} - h_{w1}) \dot{M}_w \quad (5.2)$$

The derivative of Eq. (5.2) with respect to axial position along the divided by the tube perimeter gives the external heat flux q_{ext} along an elementary length dz :

$$q_{ext} = \frac{1}{\pi D_{ext}} \frac{dQ}{dz} = \frac{\dot{M}_{wat}}{\pi D_{ext}} \left(\frac{dh_w(z)}{dz} \right) \quad (5.3)$$

Thus, knowing the enthalpy profile $h_w(z)$, the external heat flux can be calculated at any point along the diabatic test section. The internal heat flux provided to the refrigerant is determined as:

$$q(z) = q_{ext} \left(\frac{D_{ext}}{D} \right) = \frac{\dot{M}_w}{\pi D} \left(\frac{dh_w(z)}{dz} \right) \quad (5.4)$$

5.6.4 Vapor quality

The vapor quality is calculated by an energy balance over the preheater and the test section. Hence, the vapor at any test section position can be calculated from the following equation:

$$x(z) = \frac{P + \dot{M}_w c_w (T_{w(inlet)} - T_w(z))}{\dot{M}_{ref} h_{LV}} \quad (5.5)$$

where P is the electrical power provided from the preheater, $T_{w(inlet)}$ is the temperature of the heating water at the inlet of the diabatic test section, $T_w(z)$ is the water temperature at any position along the test section, c_w is the water specific heat, \dot{M}_w , \dot{M}_{ref} are the water and refrigerant mass flow, respectively.

5.7 Accuracy of measurements

In order to sure that the entire measurement system is working correctly, liquid-liquid tests have been done with subcooled R22 and R410A versus water for both test sections. The accuracy of the energy balance between the heating and cooling fluids was thus determined. The results of this tests are not shown here but Q_w/Q_{ref} varied from 0.98 to 1.02, with a mean error of $\pm 0.98\%$ for R410A and $\pm 0.96\%$ for R22 in the 13.8 mm test section. Similar results were obtained for the 8 mm test section. This is very accurate for this type of measurement and confirms that all measurement instruments were precisely calibrated and that the system was working correctly.

5.7.1 Pressure drop measurement accuracy

Two different types of pressure transducers were used to determine the two-phase pressure drop, namely: absolute and differential. The pair of absolute transducers used in this study ranged 1 to 25 bars. They were calibrated with a very accurate balance and their accuracy was found to be $\pm 20 \text{ mbar}$. Four differential transducers were used for the small and intermediate range in this study. They ranged 0 – 20 mbar and 0 – 40 mbar for the low range and 0 – 160 mbar and 0 – 500 mbar for the intermediate. An accuracy of $\pm 0.05\% \text{ F.S.}$ was given by the supplier. After inhouse calibration against a water column, this value was realistic and taken as the accuracy of the transducers.

5.7.2 Heat flux measurement accuracy

For the local heat flux absolute error determination, first the derivative of the enthalpy was converted into the derivative of the temperature of the heating water

$$\frac{dh_w(z)}{dz} = c_{pw} \frac{dT_w(z)}{dz} \quad (5.6)$$

Then, substituting into Eq. (5.4), local heat flux in each point of the test section can be calculated with:

$$q(z) = \frac{\dot{M}_w}{\pi D} c_{pw} \frac{dT_w(z)}{dz} \quad (5.7)$$

and assuming that the measurements of the water temperature are linearly independent, the absolute error of the heat flux Δq can be determined with the following expression:

$$\Delta q(z) = \sqrt{\left(\frac{dq(z)}{d\dot{M}_w} \Delta \dot{M}_w\right)^2 + \left(\frac{dq(z)}{dT_w} \Delta T_w\right)^2} \quad (5.8)$$

After calculation, the mean relative error does not exceed 2% and 1% for the 13.8 mm and 8 mm test section, respectively.

5.7.3 Vapor quality measurement accuracy

Assuming that all measured values are linearly independent, the absolute vapor quality error at each position of the evaporator based on the general definition applied to Eq. (5.5) can be expressed as:

$$\Delta x(z) = \sqrt{\begin{aligned} & \left(\frac{\partial x}{\partial P} \Delta P\right)^2 + \left(\frac{\partial x}{\partial T_{1_{water}}} \Delta T_{1_{water}}\right)^2 + \left(\frac{\partial x}{\partial T_{wat}(z)} \Delta T_{wat}(z)\right)^2 + \left(\frac{\partial x}{\partial \dot{M}_{wat}} \Delta \dot{M}_{wat}\right)^2 \\ & + \left(\frac{\partial x}{\partial \dot{M}_{ref}} \Delta \dot{M}_{ref}\right)^2 + \left(\frac{\partial x}{\partial P_{sat}} \Delta P_{sat}\right)^2 \end{aligned}} \quad (5.9)$$

The term with the saturation pressure P_{sat} in the vapor quality error calculation is encountered because the latent heat of the refrigerant is determined from the measurement of the saturation pressure.

The absolute uncertainty for the heating power measurements is ± 20 W and the accuracy of the temperature measurements is $\pm 0.02^\circ\text{C}$. The absolute error of the absolute pressure transducers after calibration has been estimated to be ± 20 mbar. The refrigerant and water mass flow rates are measured with an accuracy of $\pm 0.15\%$. After calculating of partial derivatives and substituting all values in Eq. (5.9), the maximum absolute errors for each tested mass velocity have been obtained. The calculated mean relative errors does not exceed 2% and 3% for the 13.8 mm and 8 mm test section, respectively.

5.8 Conclusions

The existing LTCM flow boiling test facility has been successfully modified and adapted to the different test conditions and measurement methods. Two new test sections, 8.00 mm and 13.8 mm plain horizontal tubes, have been successively implemented into the modified test rig. The new test section consists in two zones: diabatic and adiabatic. This configuration allows tests to be run that obtain experimental two-phase pressure drop values under diabatic and adiabatic conditions simultaneously. Moreover, the addition of an adiabatic test section allows data to be obtained with the same flow regime at the inlet and outlet of the test section.

Chapter 6

Experimental Results

This chapter focuses on experimental results obtained during the experimental campaign. First, the data reduction procedure to obtain the two-phase frictional component of the measured values is described and validated. Next, the influence of the different test variables is depicted for some representative sets of experimental conditions. Finally, the entire results of the two-phase pressure drop measurements are presented.

6.1 Reduction of experimental data

The general expression for describing the total two-phase pressure drop Δp_{total} is:

$$\Delta p_{total} = \Delta p_{static} + \Delta p_{mom} + \Delta p_{frict} \quad (6.1)$$

where Δp_{static} is the elevation head pressure drop (presently $\Delta p_{total} = 0$ for a horizontal tube), Δp_{mom} is the momentum pressure drop created by acceleration of the flow in a diabatic process and Δp_{frict} is the two-phase frictional pressure drop.

The new two-zone test sections yields the two-phase pressure drops in the diabatic (first zone) and adiabatic (second zone) simultaneously. The adiabatic two-phase pressure drops were obtained at the vapor quality leaving the diabatic test section and for the reason mention above (adiabatic process) the momentum pressure drop $\Delta p_{mom} = 0$. Hence, one can directly determine the two-phase frictional pressure drops for the adiabatic test section from the measured values:

$$\Delta p_{frict} = \Delta p_{total} \quad (6.2)$$

For the diabatic test section one determines the two-phase frictional pressure drops from the following equation:

$$\Delta p_{frict} = \Delta p_{total} - \Delta p_{mom} \quad (6.3)$$

Hence, one must first evaluate the momentum pressure drop Δp_{mom} to obtain the frictional pressure drop values. The momentum pressure drop in the diabatic test section reflects the increase in the kinetic energy of the flow during the evaporation process and is given by the following expression:

$$\Delta p_{mom} = G^2 \left\{ \left[\frac{(1-x)^2}{\rho_L(1-\epsilon)} + \frac{x^2}{\rho_G\epsilon} \right]_{out} - \left[\frac{(1-x)^2}{\rho_L(1-\epsilon)} + \frac{x^2}{\rho_G\epsilon} \right]_{in} \right\} \quad (6.4)$$

where G is the total mass velocity of liquid plus vapor, x is the vapor quality at the inlet or outlet of the test section, ϵ is the vapor cross-sectional void fraction at the inlet or outlet of the test section, ρ_L and ρ_V are the liquid and vapor densities and g is 9.81 m/s^2 . Based on a recent work by Wojtan-Ursenbacher-Thome [154], they found the Steiner version of the Rouhani-Axelsson drift flux model to be very accurate for predicting void fractions in similar experimental conditions. Hence the following expression is used to calculate the void fractions:

$$\epsilon = \frac{x}{\rho_G} \left[(1 + 0.12(1-x)) \left(\frac{x}{\rho_G} + \frac{(1-x)}{\rho_L} \right) + \frac{1.18(1-x)[g\sigma(\rho_L - \rho_G)]^{0.25}}{G^2 \rho_L^{0.5}} \right]^{-1} \quad (6.5)$$

This expression is used in Eq. (6.4) to determine the momentum pressure from the experimental conditions.

Using water in the annulus of the double pipe system to evaporate the refrigerant, the water undergoes a temperature change while the phase changing refrigerant stays at nearly the same saturation temperature. This causes a change in the local heat flux as the temperature difference between the water and the refrigerant decreases during the evaporation process along the length of the tube. In order completely determine the momentum pressure drop created by acceleration of the flow Δp_{mom} , one must know the vapor quality. As this is changing during the evaporation process, the results are reported at the mean vapor quality in the diabatic test section based on an evaluation (piecewise decomposition) of the enthalpy profile obtained from the water-side.

Figs. (6.1) and (6.2) show, for the 8 mm and 13.8 mm tube respectively, the total, momentum and frictional pressure drops for a representative set of experimental conditions. The momentum pressure drops were calculated following the procedure detailed previously and the total pressure drops correspond to the measured values. As expected, the momentum pressure drop is larger for high heat fluxes reflecting the increase in the kinetic energy due to the evaporation process and vary from around 3% of the total pressure drop for the lowest heat fluxes up to 40% for the highest.

Fig. (6.3) shows a comparison, for a representative set of experimental conditions, of the two-phase pressure gradients for the adiabatic test section versus those for the diabatic test section. The agreement between the results is quite remarkable, attesting to the accuracy and reliability of the measurements as well as the appropriate data reduction procedure. At high vapor qualities, the difference between the two types of measurements is thought to be caused by the vapor quality variation along the diabatic test section around the peak, which averages out the pressure gradient rather than giving the "local" value at a particular vapor quality as in the adiabatic test section. For instance, in the diabatic test section at the vapor quality at the peak, part of the test section will be operating at local conditions before the peak and part at local conditions after the peak, resulting in a lower value than for the adiabatic test section at the same vapor quality. It is for this range of test conditions that the adiabatic test section was added to the loop in order to obtain data representative of the real pressure gradients at high vapor qualities near and after the peak.

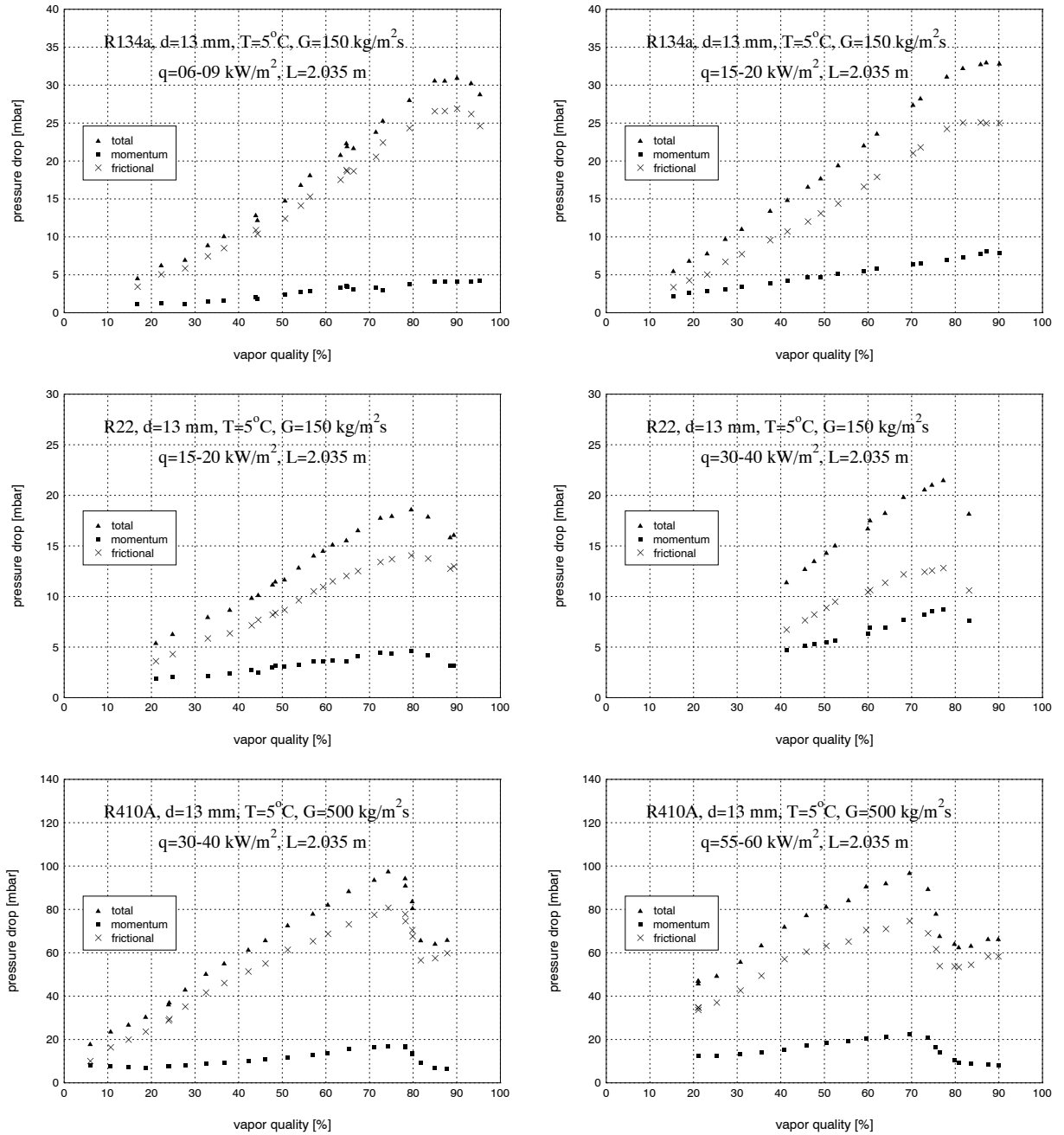


Figure 6.1: Total, frictional and momentum pressure drops vs. vapor quality at different experimental conditions ($d = 13.8\text{ mm}$).

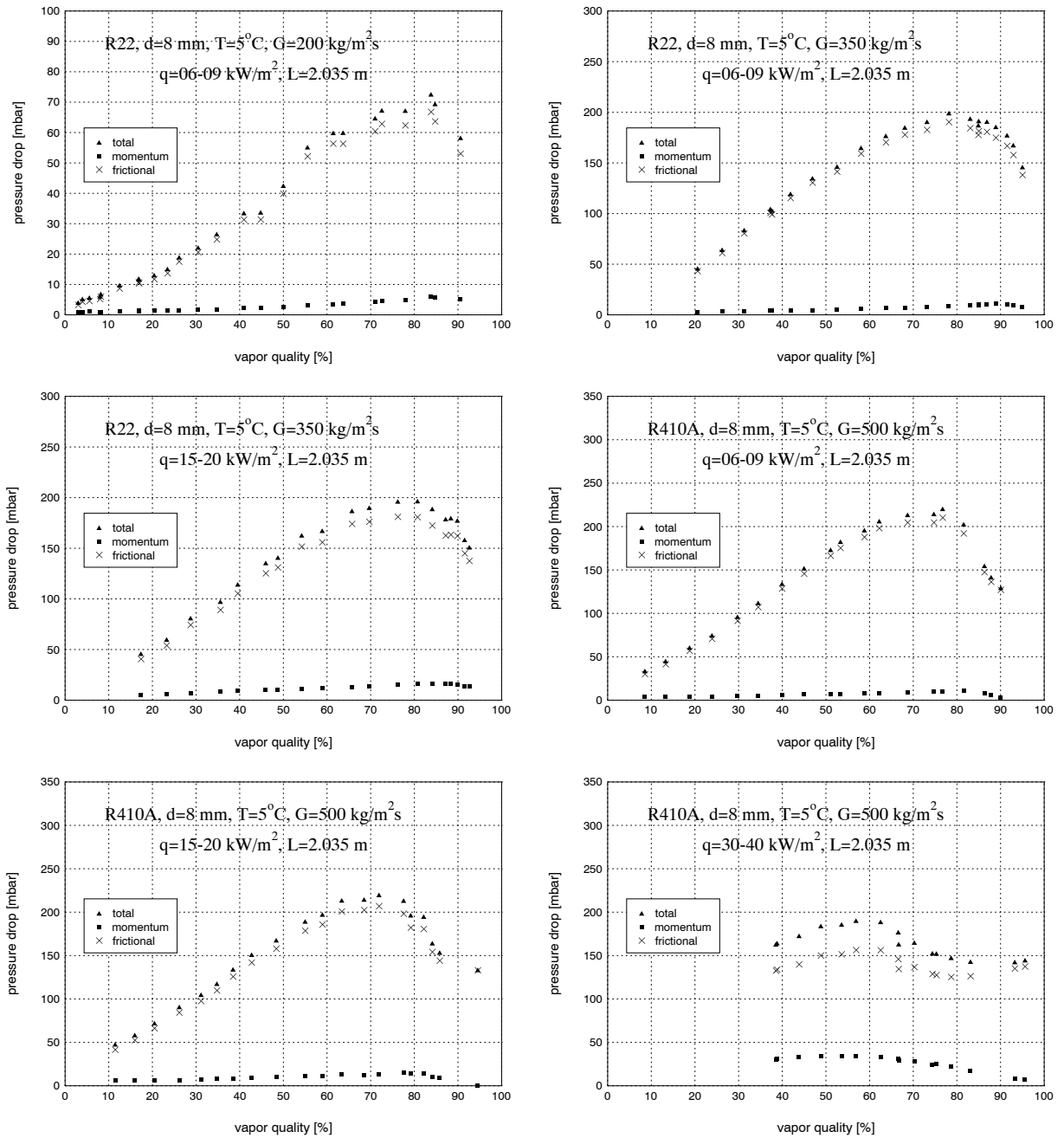


Figure 6.2: Total, frictional and momentum pressure drops vs. vapor quality at different experimental conditions ($d = 8$ mm).

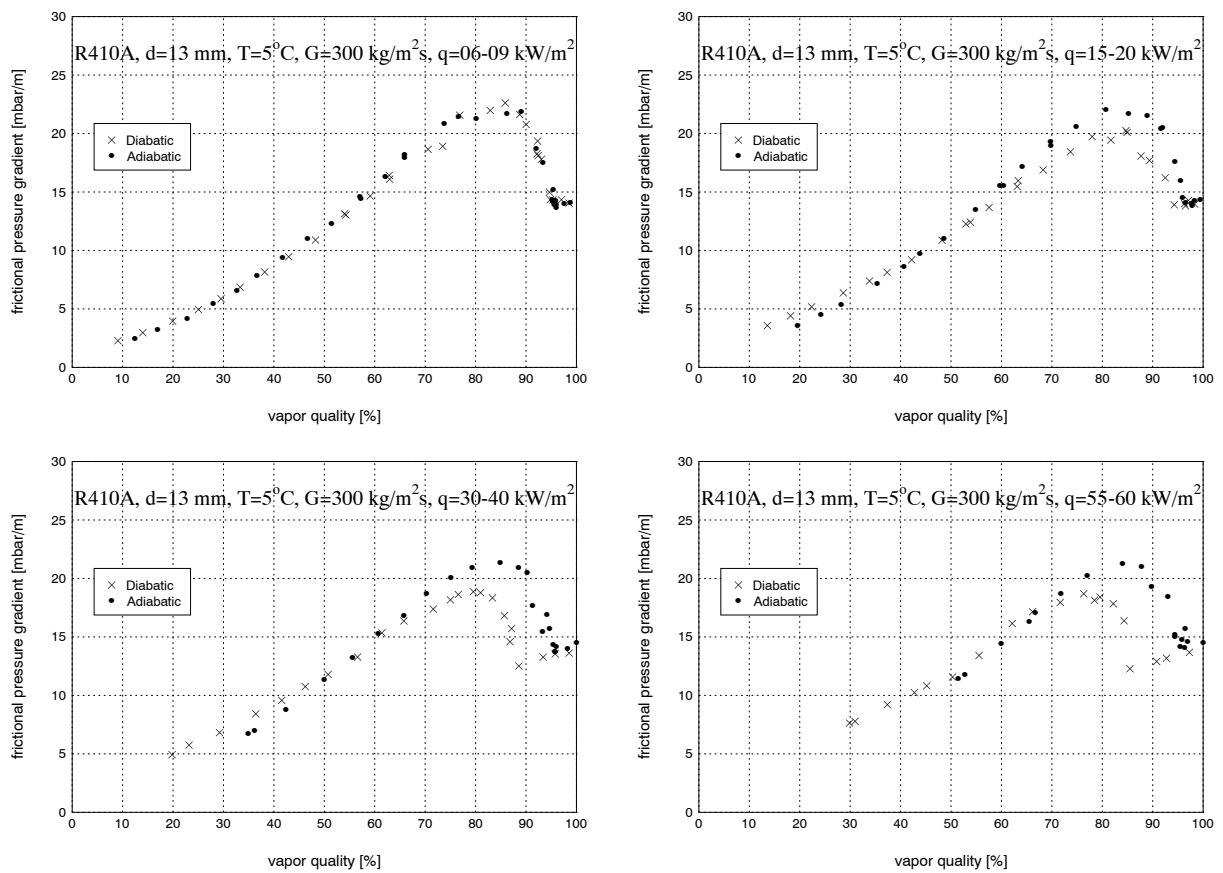


Figure 6.3: Adiabatic vs. diabatic test section results for R410A.

6.2 Two-phase pressure drop measurements

First, some comparisons of two-phase pressure drop measurements are presented here in order to determine the influence of different test variables. Then, the entire database is depicted in a graphical form.

6.2.1 Some comparisons for different experimental parameters

Diameter

Fig. (6.4) depicts a comparison of the two-phase frictional pressure drops for the internal diameters tested at a particular set of test variables. The smaller diameter tube induces a larger two-phase pressure gradient.

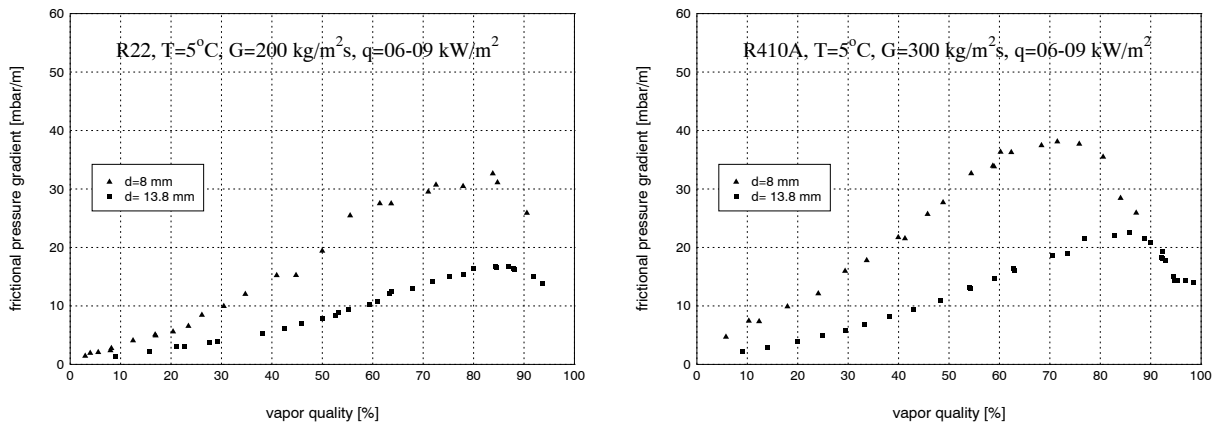


Figure 6.4: Frictional pressure gradients vs. vapor quality for R22 and R410A.

Fluid

Fig. (6.5) shows that the frictional two-phase pressure gradients are largest for R134a and smallest for R410A with R22 in the middle. The data for each fluid shows the characteristic rise in two-phase frictional pressure gradient with rising vapor quality, a peak at high vapor quality, and the subsequent falloff as the vapor quality approaches 100%. The trends in the data are seen to be very clear with little scatter in the data because of the accuracy of the transducers, the accuracy of the energy balances and the fine control on the steady-state operating conditions.

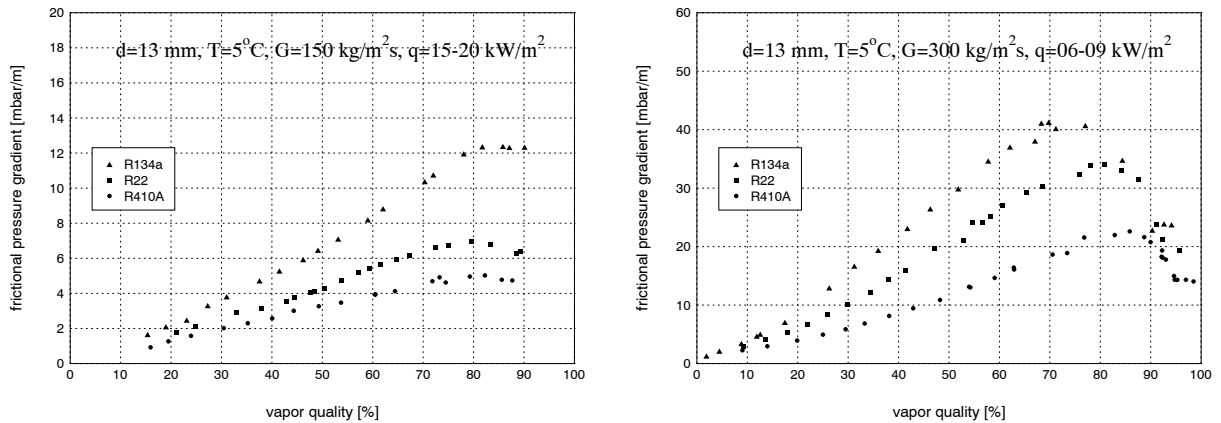


Figure 6.5: Comparison of the frictional pressure gradients for R134a, R22 and R410A at two set of experimental conditions.

Mass velocity

Fig. (6.6) depicts the experimental results for R22 and R410A at several mass velocities for a particular set of experimental conditions. As expected, the frictional pressure gradient increases with mass velocity.

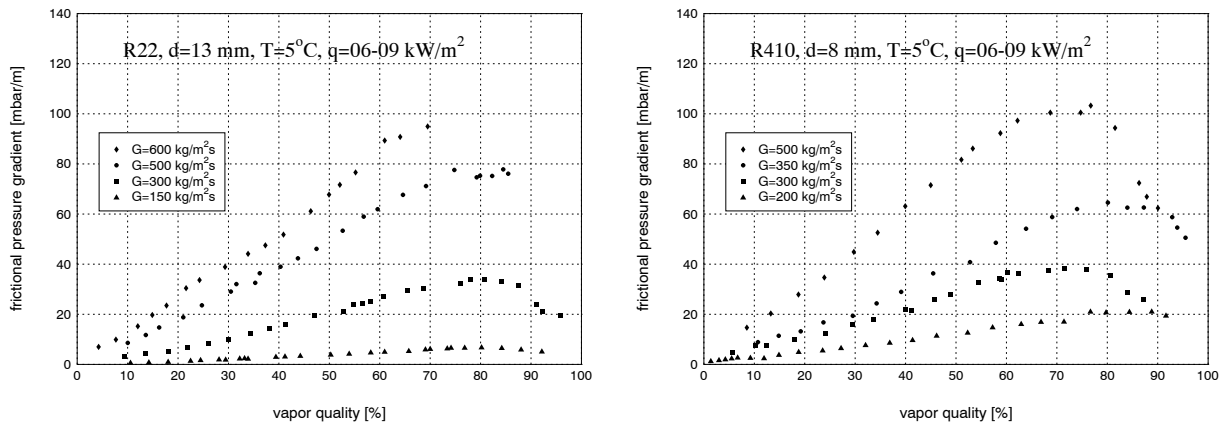


Figure 6.6: Frictional pressure gradients vs. vapor quality for different mass velocities.

Heat flux

Fig. (6.7) illustrates the frictional pressure drop data obtained at different heat fluxes, from rather low to quite high values. The effect of the evaporation heat flux is seen to be of only minor importance at vapor qualities before the peak. At high vapor qualities, the peak is shifted to lower vapor qualities by the increase in the heat flux and this is the more important influence of the heat flux observed. The location of the peaks coincides with the onset of dryout at the top of the tube and the top of the tube is dry after the peak. For the highest heat fluxes, based on visual observations in the sight glass at the end of the diabatic test section, the flow was observed to convert to mist flow, and these are the data at high vapor quality that depict an increasing trend with vapor quality after the falloff, e.g. such as those in the left graph at $q = 55 - 60 \text{ kW/m}^2$.

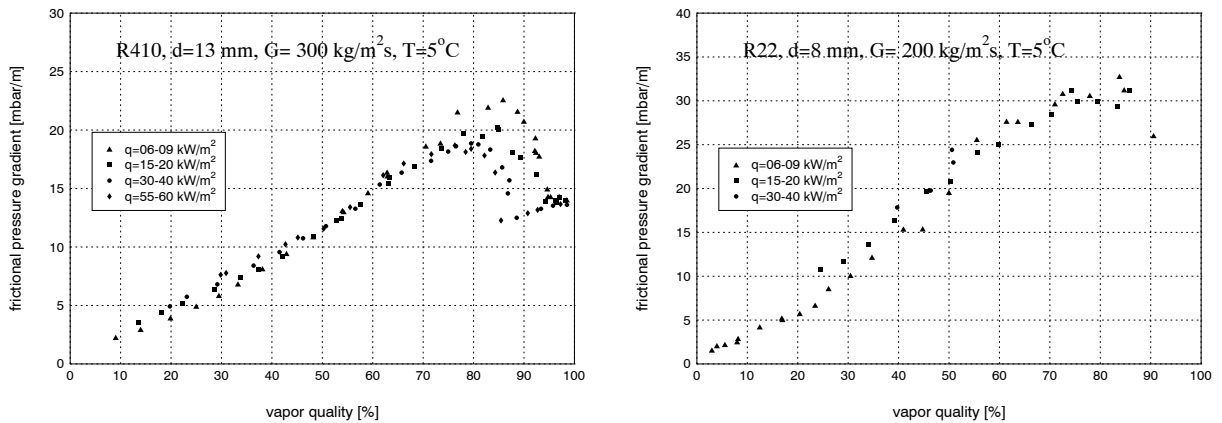


Figure 6.7: Frictional pressure gradients vs. vapor quality at different heat fluxes.

6.2.2 Results for R134a

$d=13.8\text{ mm}$

All the results for R134a are shown in Fig. (6.8). Only tests with the 13.8 mm test section were made for this refrigerant.

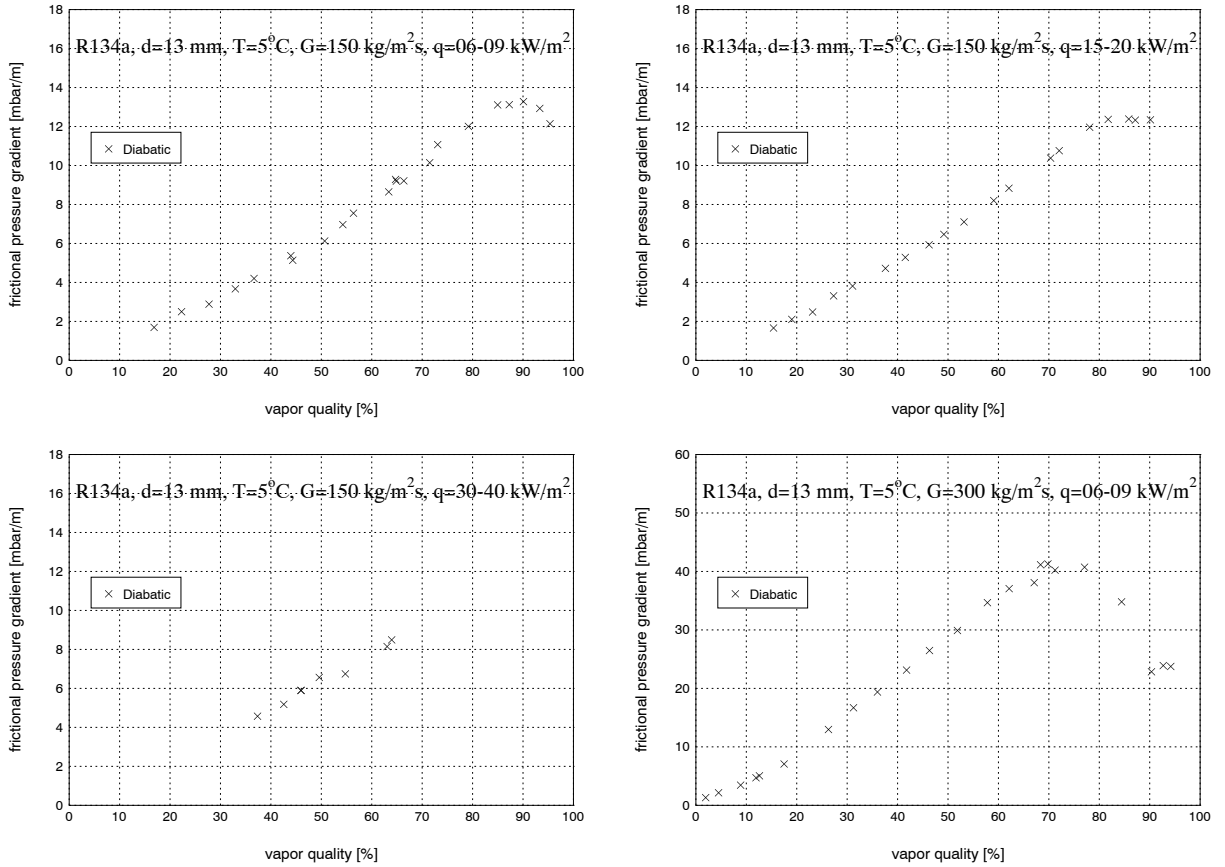
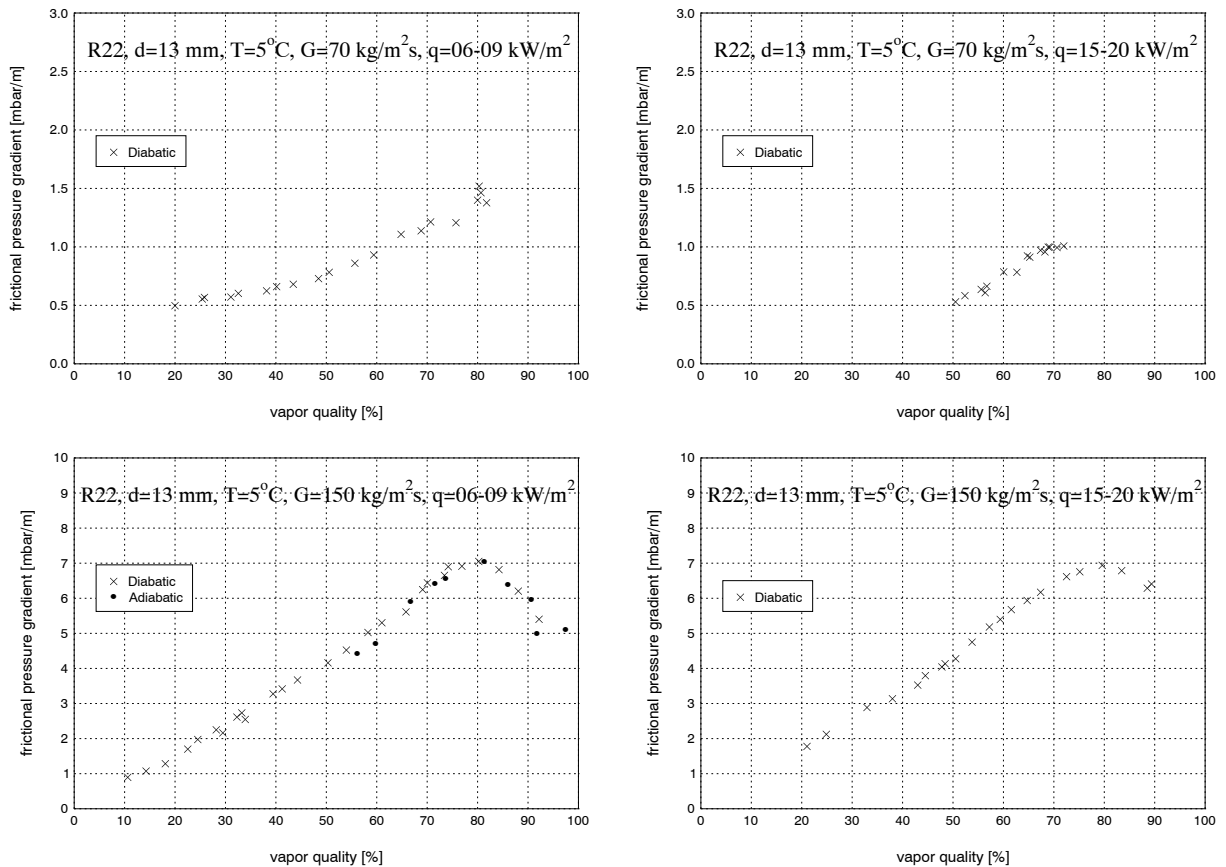


Figure 6.8: Frictional pressure gradients vs. vapor quality for R134a at different experimental conditions ($d = 13.8\text{ mm}$).

6.2.3 Result for R22

d=13.8 mm

All the results obtained for R22 in the 13.8 mm test section are shown in Figs. (6.9)-(6.12).

Figure 6.9: Frictional pressure gradients vs. vapor quality for R22 at different experimental conditions ($d = 13.8 \text{ mm}$) – (I).

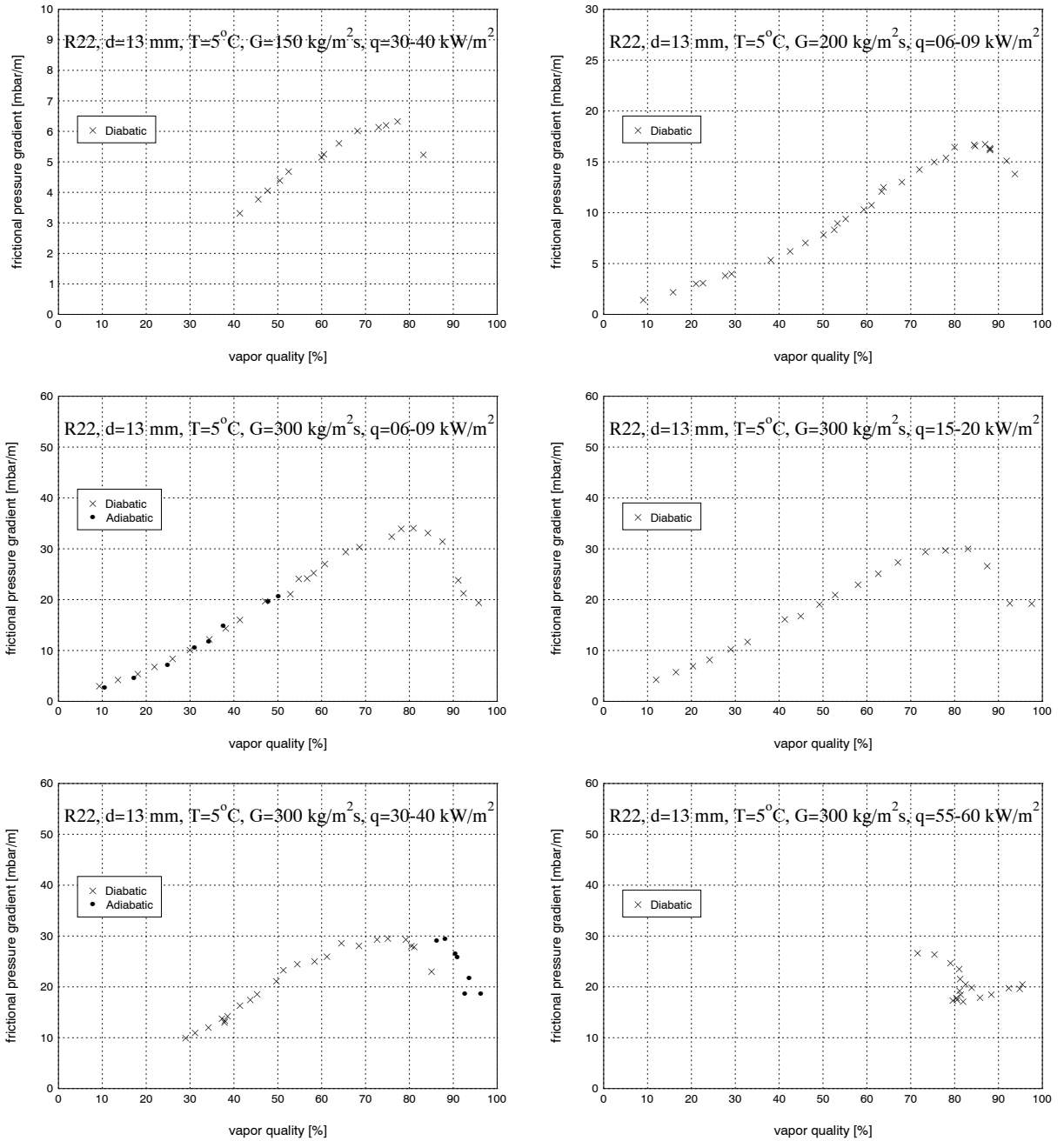


Figure 6.10: Frictional pressure gradients vs. vapor quality for R22 at different experimental conditions ($d = 13.8 \text{ mm}$) – (II).

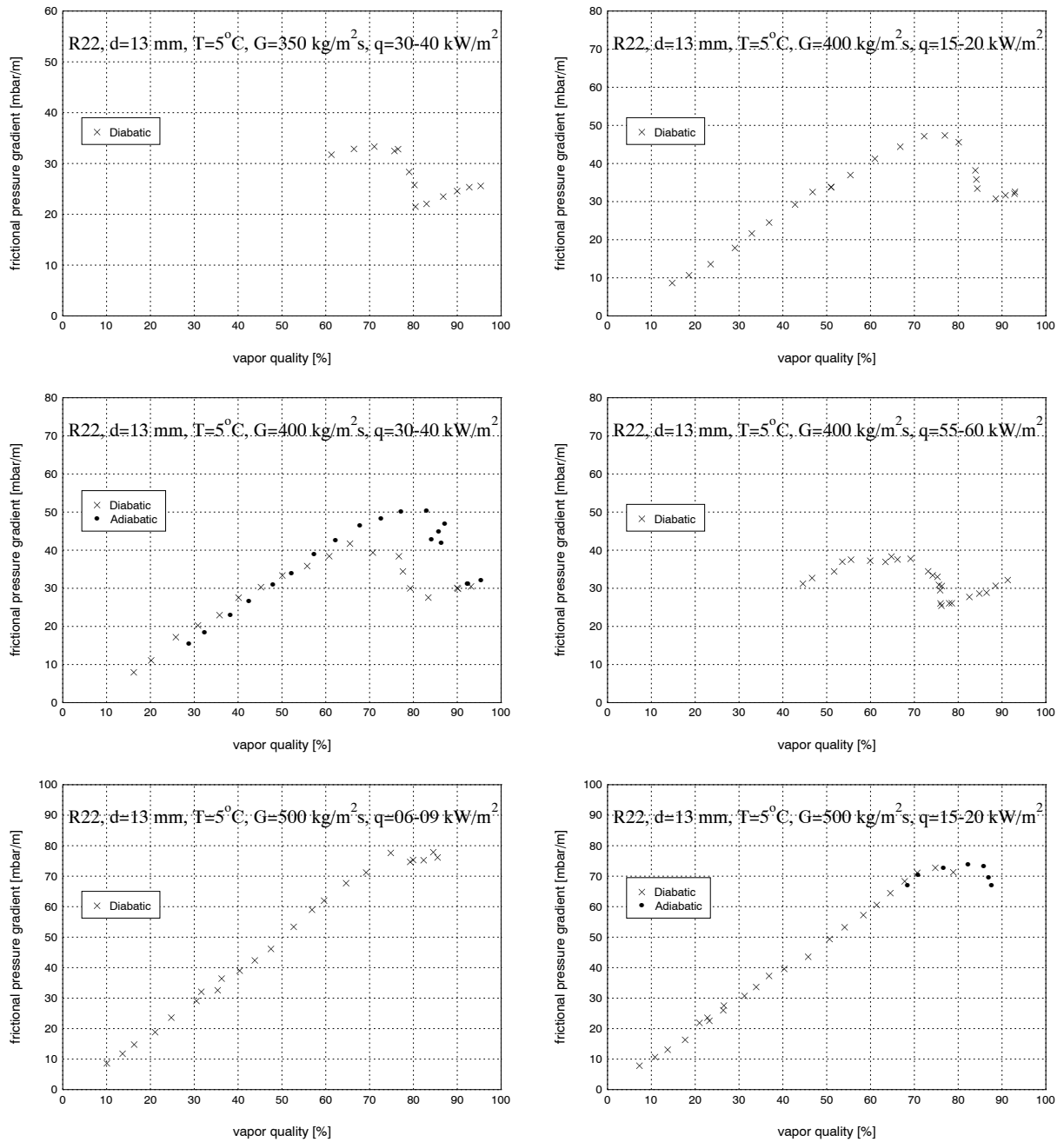


Figure 6.11: Frictional pressure gradients vs. vapor quality for R22 at different experimental conditions ($d = 13.8\text{ mm}$) – (III).

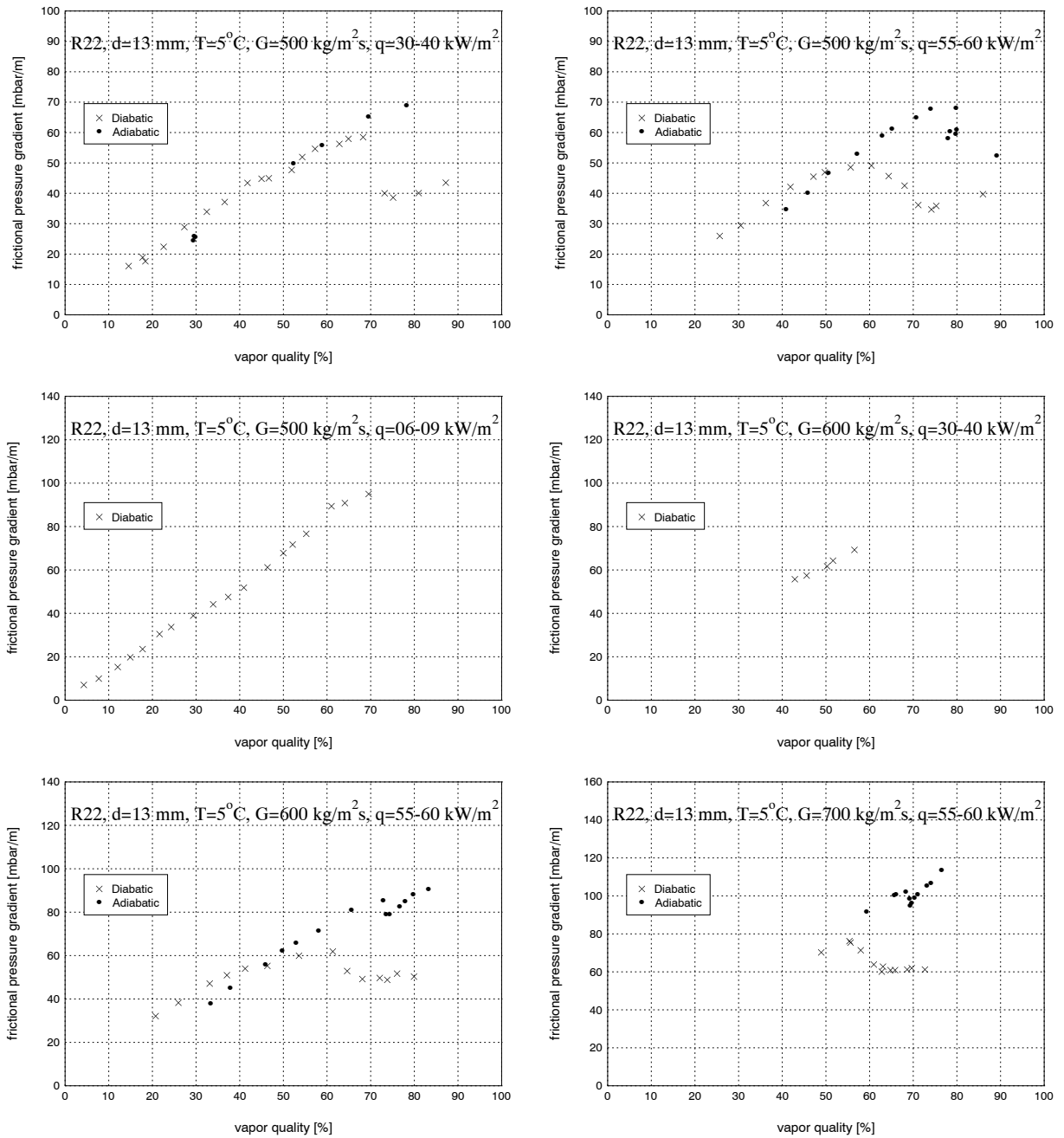


Figure 6.12: Frictional pressure gradients vs. vapor quality for R22 at different experimental conditions ($d = 13.8\text{ mm}$) – (IV).

$d=8\text{ mm}$

All the results obtained for R22 in the 8 mm test section are shown in Figs. (6.13)-(6.14).

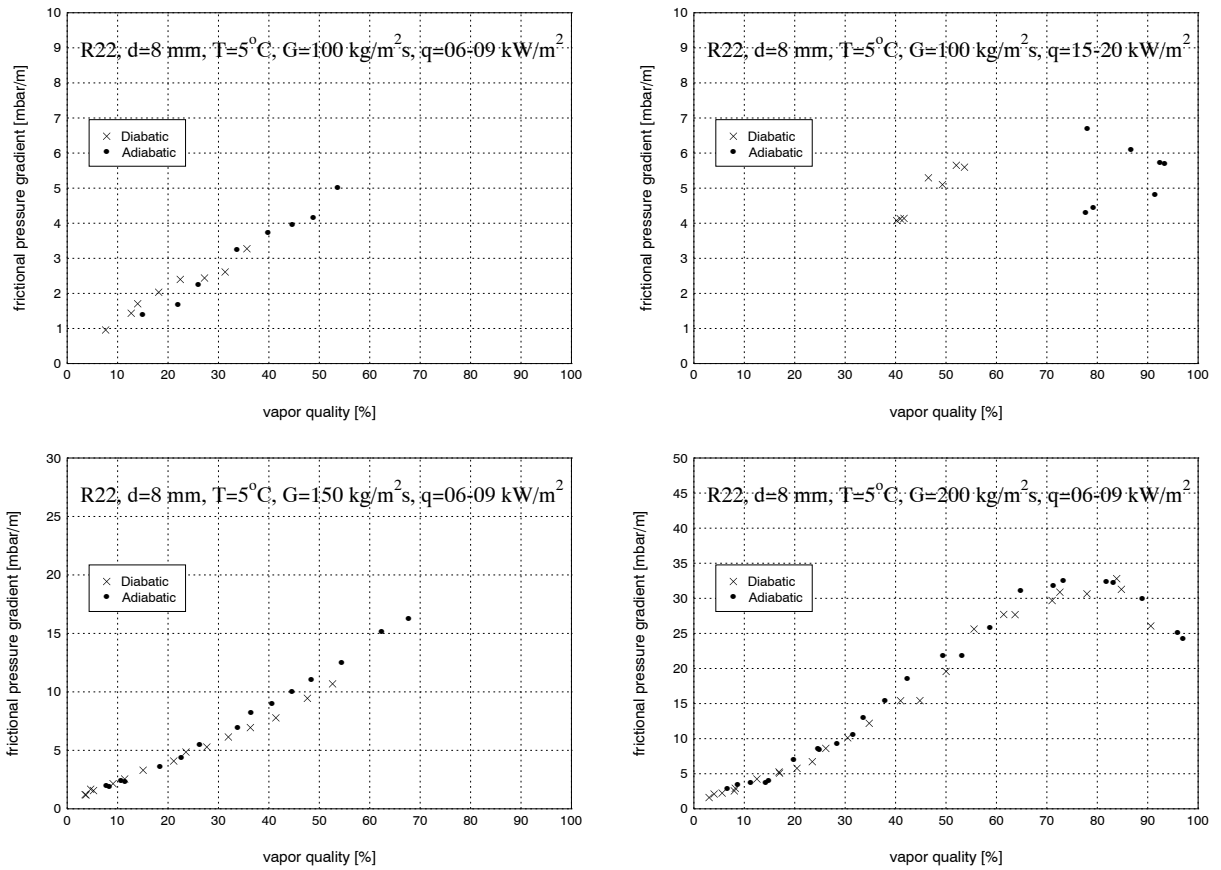


Figure 6.13: Frictional pressure gradients vs. vapor quality for R22 at different experimental conditions ($d = 8\text{ mm}$) – (I).

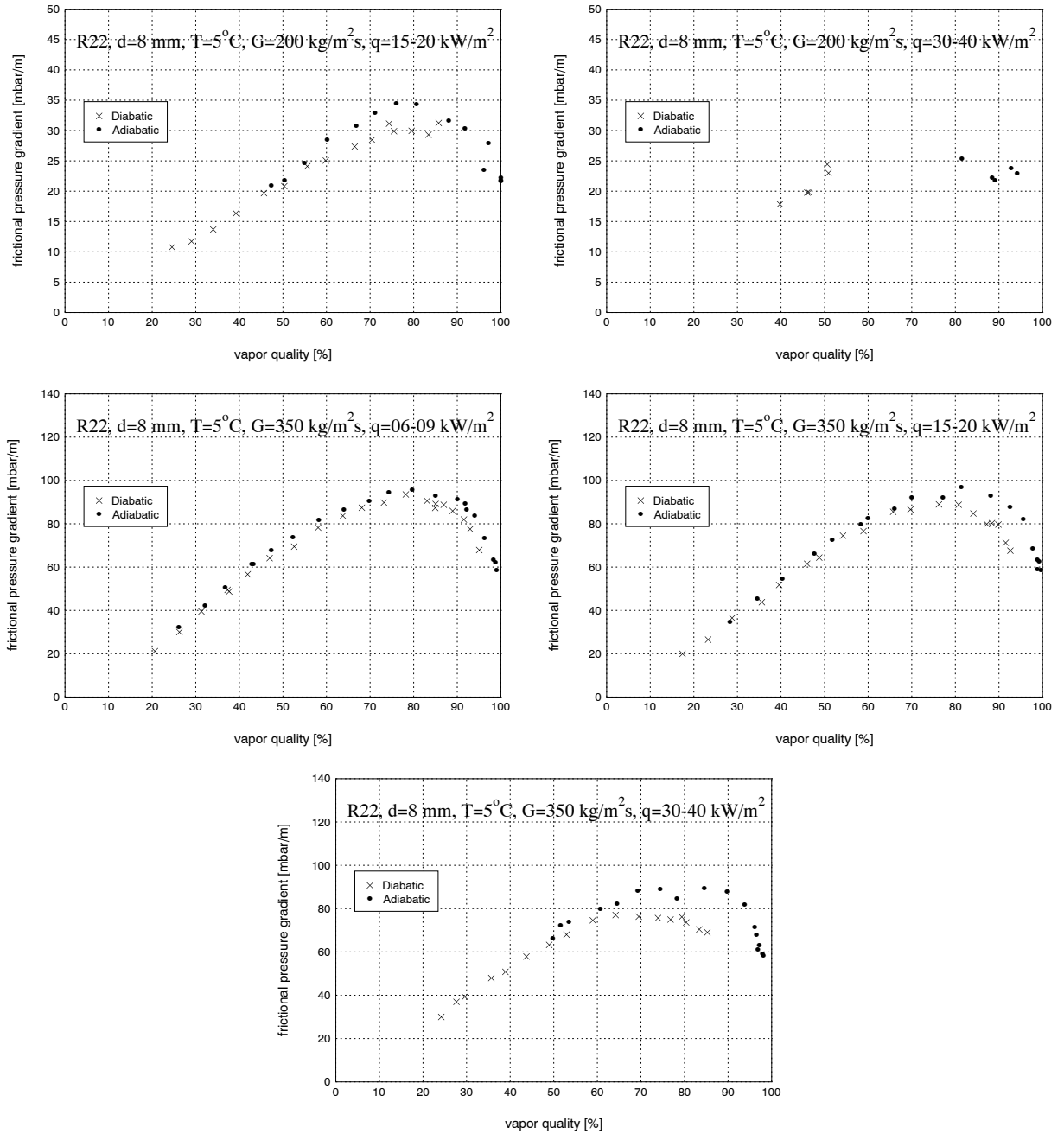


Figure 6.14: Frictional pressure gradients vs. vapor quality for R22 at different experimental conditions ($d = 8\text{ mm}$) – (II).

6.2.4 Result for R410A

d=13.8 mm

All the results obtained for R410A in the 13.8 mm test section are shown in Figs. (6.15)-(6.18).

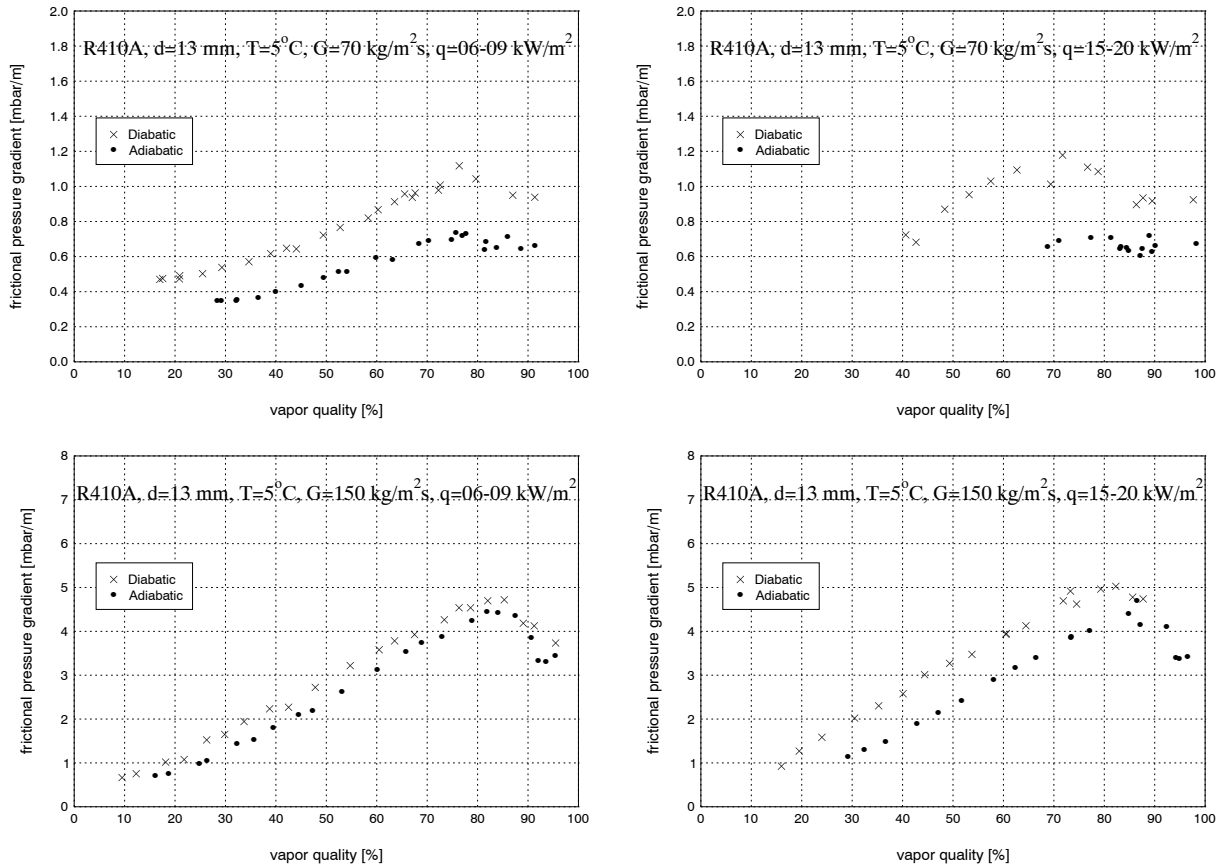


Figure 6.15: Frictional pressure gradients vs. vapor quality for R410A at different experimental conditions ($d = 13.8 \text{ mm}$) – (I).

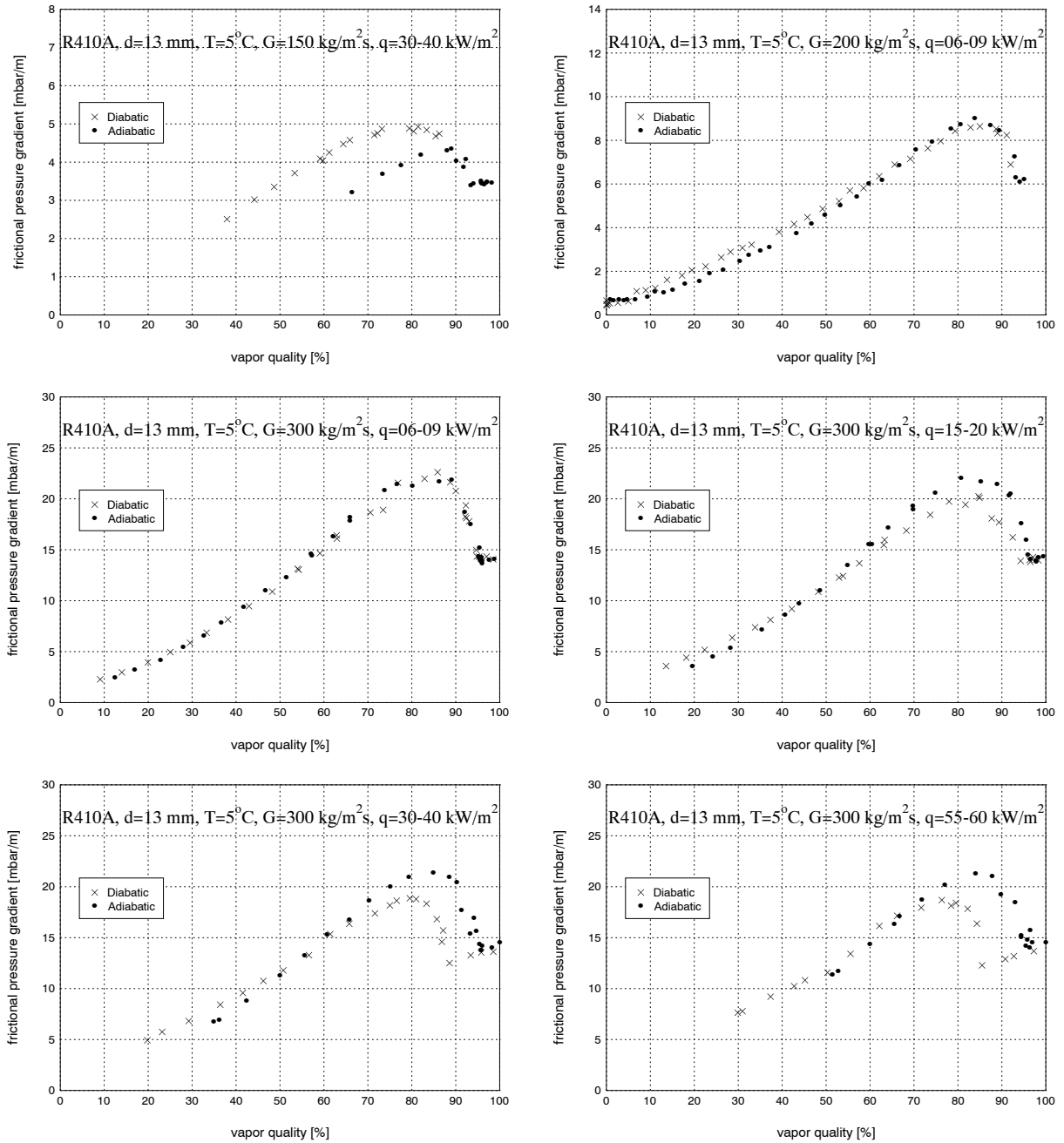


Figure 6.16: Frictional pressure gradients vs. vapor quality for R410A at different experimental conditions ($d = 13.8\text{ mm}$) – (II).

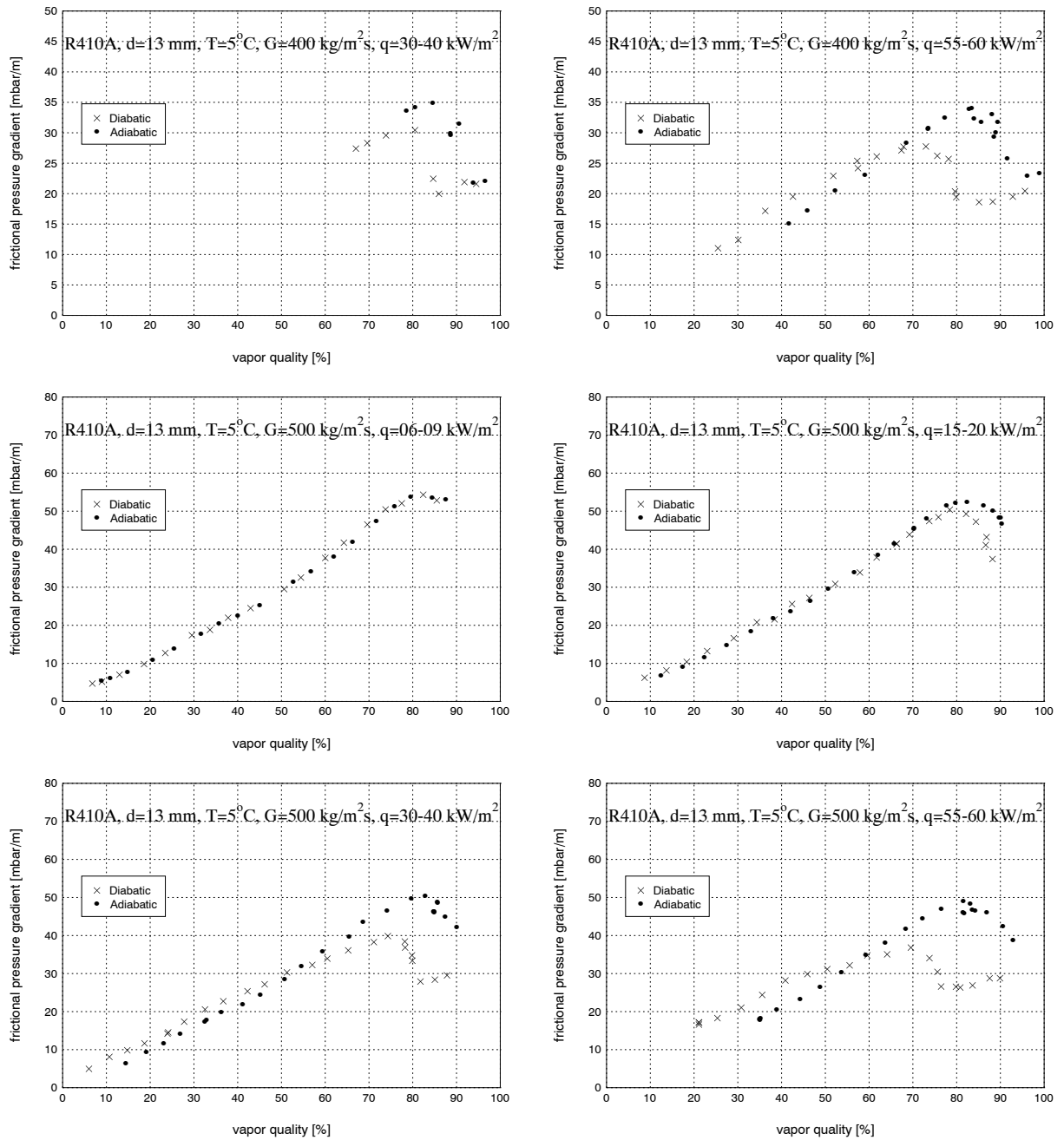


Figure 6.17: Frictional pressure gradients vs. vapor quality for R410A at different experimental conditions ($d = 13.8\text{ mm}$) – (III).

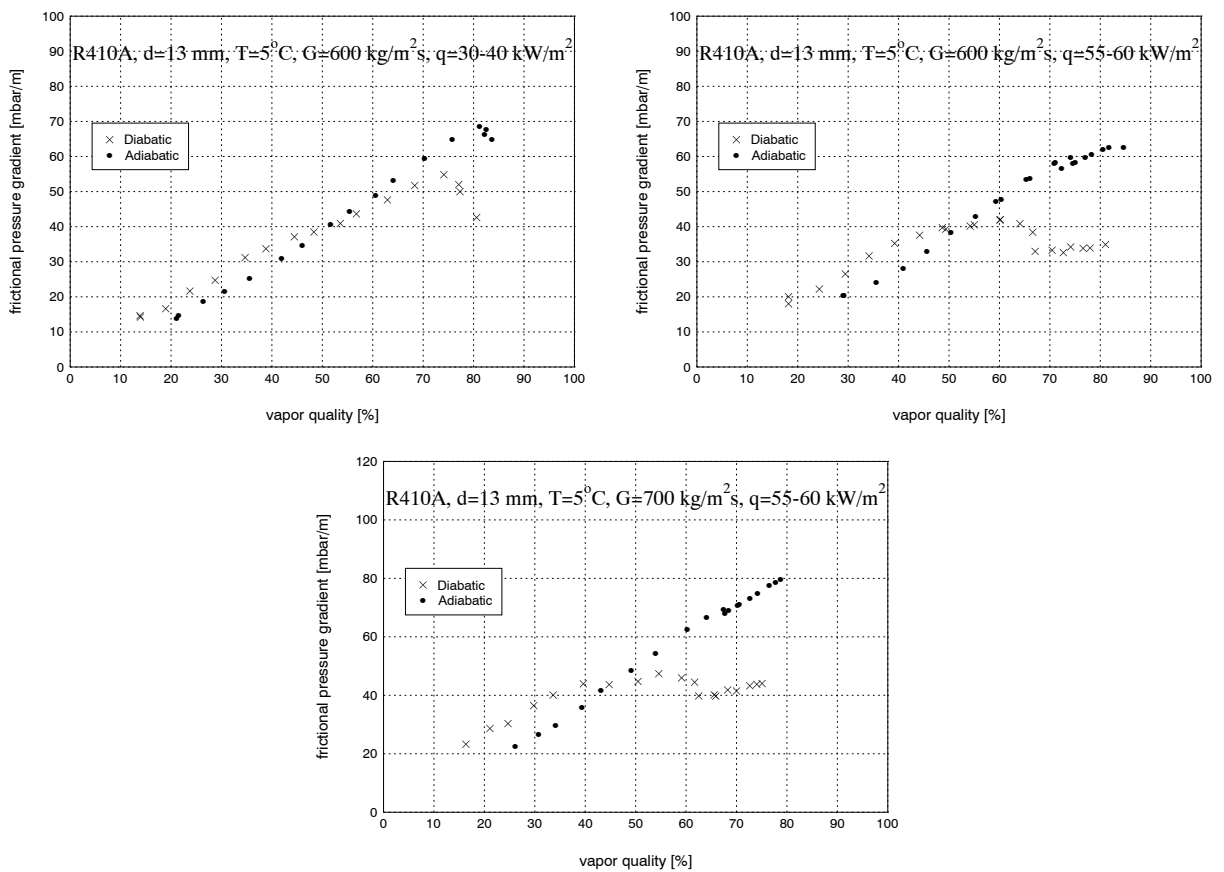


Figure 6.18: Frictional pressure gradients vs. vapor quality for R410A at different experimental conditions ($d = 13.8\text{ mm}$) – (IV).

$d=8\text{ mm}$

All the results obtained for R410A in the 8 mm test section are shown in Figs. (6.19)-(6.22).

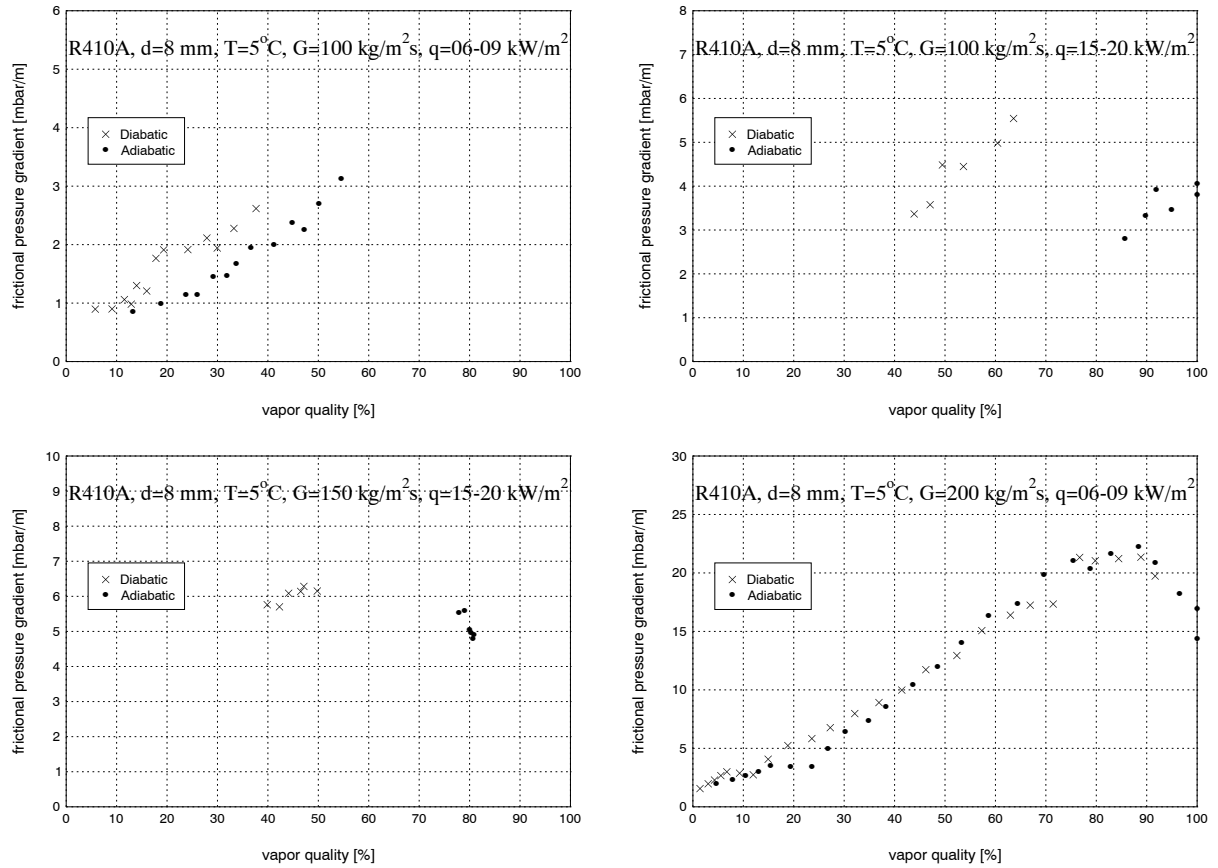


Figure 6.19: Frictional pressure gradients vs. vapor quality for R410A at different experimental conditions ($d = 8\text{ mm}$) – (I).

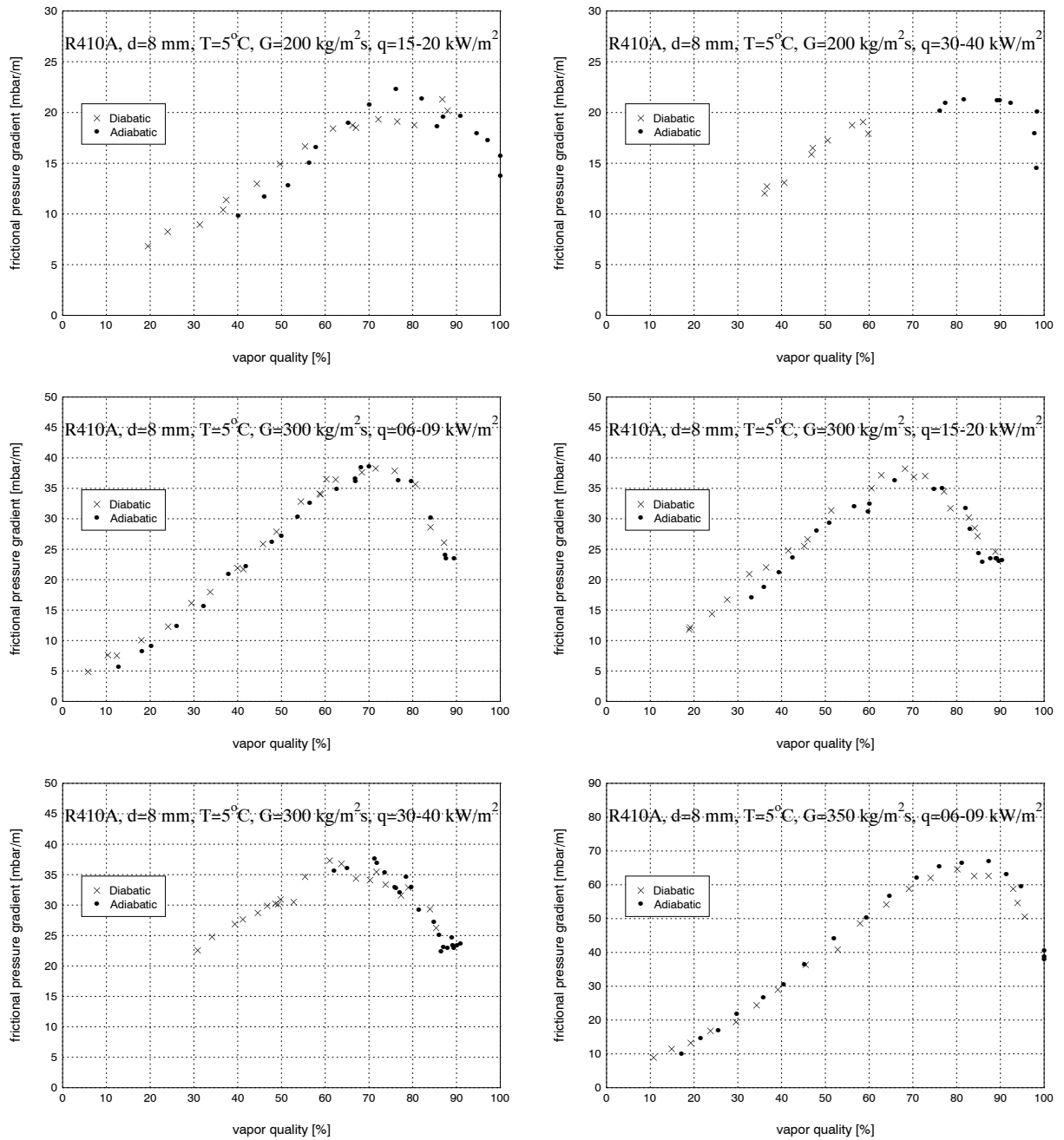


Figure 6.20: Frictional pressure gradients vs. vapor quality for R410A at different experimental conditions ($d = 8 \text{ mm}$) – (II).

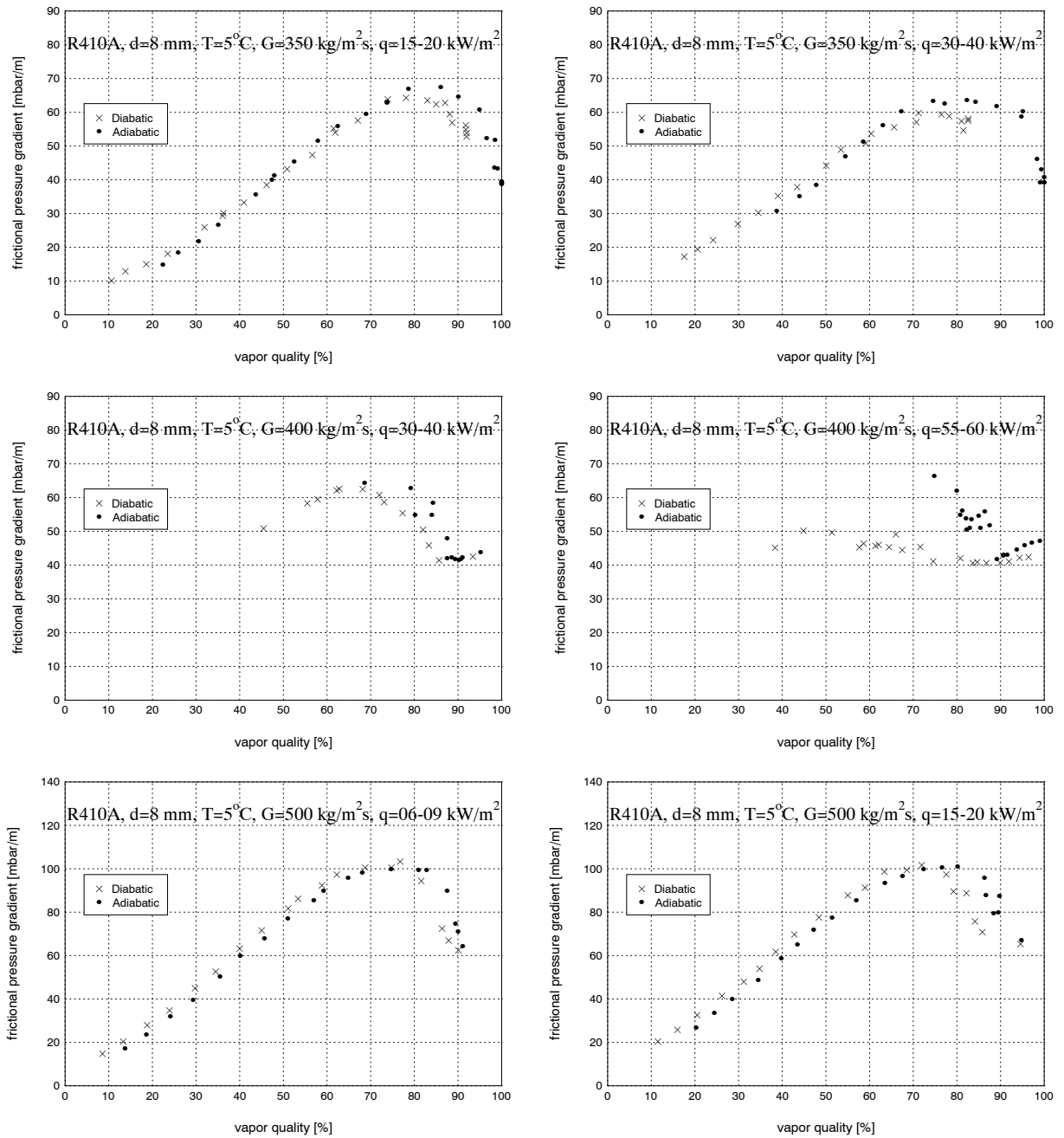


Figure 6.21: Frictional pressure gradients vs. vapor quality for R410A at different experimental conditions ($d = 8\text{ mm}$) – (III).

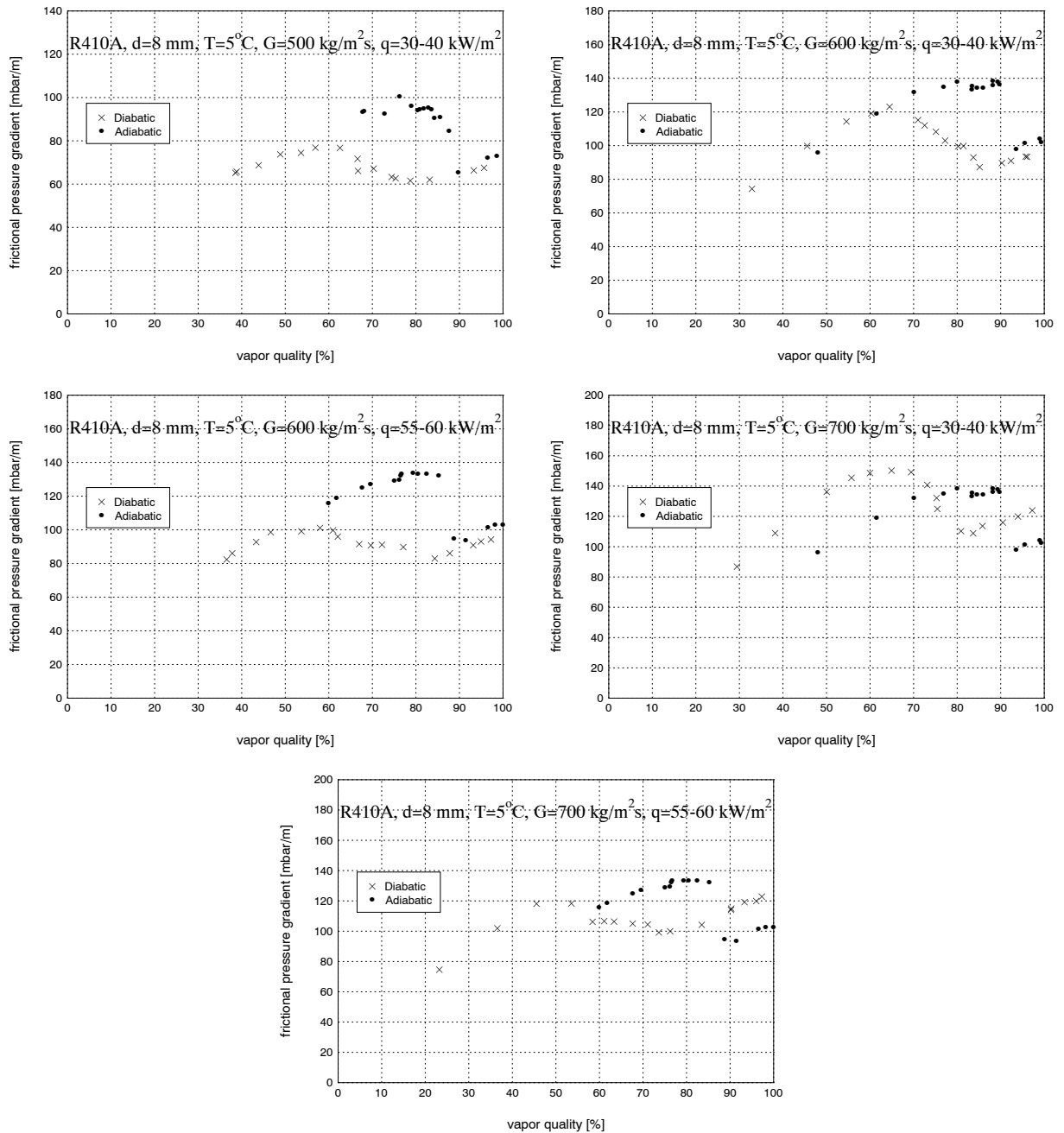


Figure 6.22: Frictional pressure gradients vs. vapor quality for R410A at different experimental conditions ($d = 8\text{ mm}$) – (IV).

6.3 Conclusions

The procedure to obtain the two-phase frictional component from the measured values has been detailed. As the test section consisted of two separate zones, the reduction of the experimental data was different depending on the zone. While for the adiabatic part of the test section there is no momentum pressure drop created by acceleration of the flow and the frictional component corresponded to the measured value, for the diabatic zone this term needs to be evaluated and subtracted from the measured values. In order to evaluate the significance of this component a set of graphs, for sake of space even if the reduction of experimental data was applied to the entire database, showed the different components of the two-phase pressure drops for a selected set of experimental conditions. By this, it was shown that the momentum pressure drop became larger as the evaporation process was more intense, i.e. high heat fluxes. Furthermore, as a validation of the data reduction procedure a set of graphs showed comparisons, for a representative set of experimental conditions, of the two-phase frictional pressure gradients for the adiabatic test section versus those for the diabatic test section. The agreement between was shown to be quite remarkable attesting to the accuracy and reliability of the measurements as well as the aptness of the data reduction protocol.

Next, and before the entire presentation of the entire database, a parametric study to evaluate the influence of the test variables was undertaken. The test variables were for the present study: fluid, diameter, mass velocities and heat fluxes as well as vapor quality representing the evaporation process. A set of graphs, for a selected representative values of the test variables, showed that while the fluid, diameter and mass velocity had a strong effect over the entire range of vapor quality, the heat flux influenced the measured values only for a particular range of vapor qualities. This latter was the reason to introduce the new two-zone test section and by this way the appropriateness of that choice has been justified.

Finally, the entire set of experimental values is presented. The results are segregated first by fluid and secondly by diameter in order to be presented in a systematic and easily readable way. More than 2500 experimental values of the two-phase pressure drops were obtained, and just to claim the significance of the presented results it is important to signal that around 25 minutes were necessary to reach the steady-state conditions.

Chapter 7

New Two-Phase Frictional Pressure Drop Model Based on Flow Pattern Map

In this chapter, first the experimental results obtained during the experimental campaign are compared to the three leading existing two-phase frictional pressure drop correlations. Second, and as a consequence of their incapability to reliably predict the present experimental database, a new two-phase frictional pressure drop model is proposed and described. The new model is developed following a phenomenological approach, that is physically based on a simplified interfacial flow structure using the recent Wojtan-Ursenbacher-Thome [155] flow pattern map. Finally, all experimental data are compared with the new prediction methods on a statistical basis. The present work completes the fourth basic steps in LTCM's flow pattern based work on two-phase and heat transfer inside horizontal tubes: (i) generalized flow pattern map, (ii) flow boiling heat transfer model, (iii) convective condensation model and (iv) two-phase frictional pressure drop model.

7.1 Comparison to existing methods

Tribbe and Müller-Steinhagen [134] compared some of the leading two-phase frictional pressure drop correlations to a large database, including the following fluid combinations: air-oil, air-water, water-steam and several refrigerants. They found that statistically the method of Müller-Steinhagen and Heck [97] gave the best and most reliable results. In another recent comparison, Ould Didi, Kattan and Thome [105] compared leading methods to experimental pressures drops obtained for five different refrigerants over a wide range of experimental conditions. Overall, they found the Grönnerud [53] and the Müller-Steinhagen and Heck [97] methods to be equally best while the Friedel [46] method was the third best in a comparison to seven leading methods.

As a first step in the present analysis, the experimental results were compared to the three previously "best" methods. The popular Lockhart-Martinelli correlation is not shown here in this comparison in spite of its extensive use and continued historical references because it was not well ranked in previous studies (nor does it compare well to the present data). A detailed description of these methods can be found in Chapter 4.

Figs. (7.1) and (7.2) show a representative comparison of the three prediction methods (Friedel,

Grönnerud and Müller-Steinhagen and Heck) for different experimental conditions. Starting first with the Grönnerud method, it works quite well at low mass velocities from low to medium vapor qualities and it also captures the maximum in the data at high vapor quality, although not in magnitude but reasonably well the location of the peak. Instead, at the highest mass velocities the Grönnerud method very significantly overpredicts all the results except at low vapor qualities. The Müller-Steinhagen and Heck correlation does not follow the trends in the data well, underpredicting most of them and does not capture the peak in the data at all. The Friedel method is seen to significantly overpredict at the lowest mass velocity while underpredicting most of the data at the highest and does not follow the variation in the data with vapor quality, again missing the peak. For sake of simplicity, comparisons for refrigerant R314a are not shown here but the situation is essentially the same.

Figs. (7.3), (7.4) and (7.5) show a comparison of the complete database to the three prediction methods (Friedel, Grönnerud and Müller-Steinhagen and Heck). Certainly of the three, the Müller-Steinhagen and Heck comes out the best overall. However, it is only able to predict one-half of the database within $\pm 20\%$.

Hence, it is clear that none of these three methods are reliable for optimizing the thermal-hydraulics of a direct-expansion evaporator, even though statistically they are not that bad when considering the normal situation for the prediction of two-phase frictional pressure drops.

In general, the existing two-phase frictional pressure models available in the literature for horizontal flows have some or all of the following deficiencies:

- They do *not* account for flow pattern effects on the process;
- They do *not* account explicitly for the influence of interfacial waves;
- They do *not* account for the upper dry perimeter of stratified types of flows;
- They do *not* use the actual velocities of the vapor and liquid by introduction of the local void fraction into the method;
- They use tubular flow expressions to represent annular film flows;
- They do *not* capture the peak in the pressure gradient at high vapor qualities (or not its location or magnitude) nor give a good representation of the pressure gradient trend versus vapor quality.
- They do *not* go to acceptable limits at $x = 0$ and $x = 1$.

Hence, this state of affairs is the justification to develop a new model. Secondly, the present flow pattern based pressure drop model fits into the unified method of Thome and coworkers to model evaporation and condensation inside horizontal tubes.

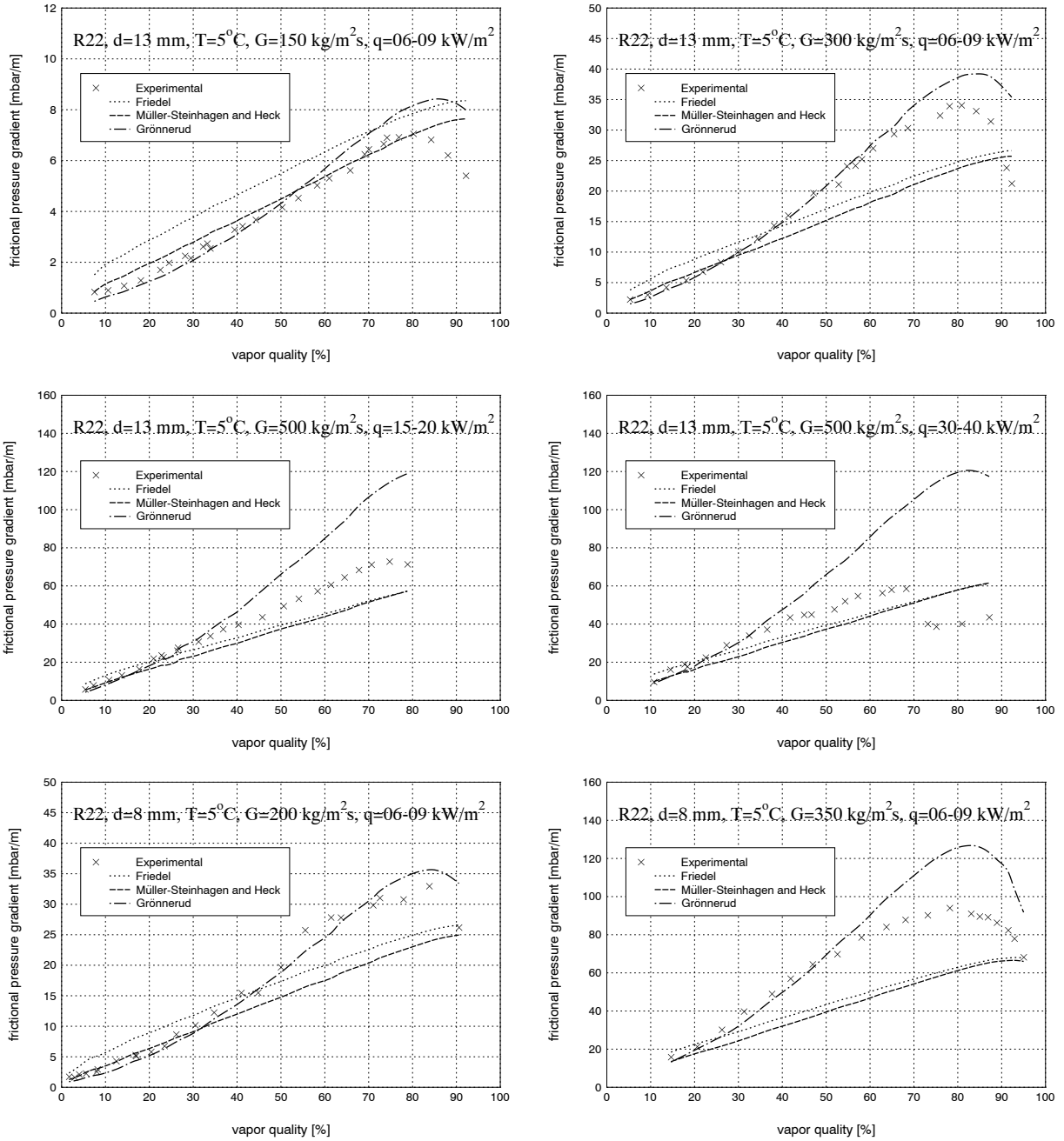


Figure 7.1: Frictional pressure gradients vs. three prediction methods for R22 at different experimental conditions.

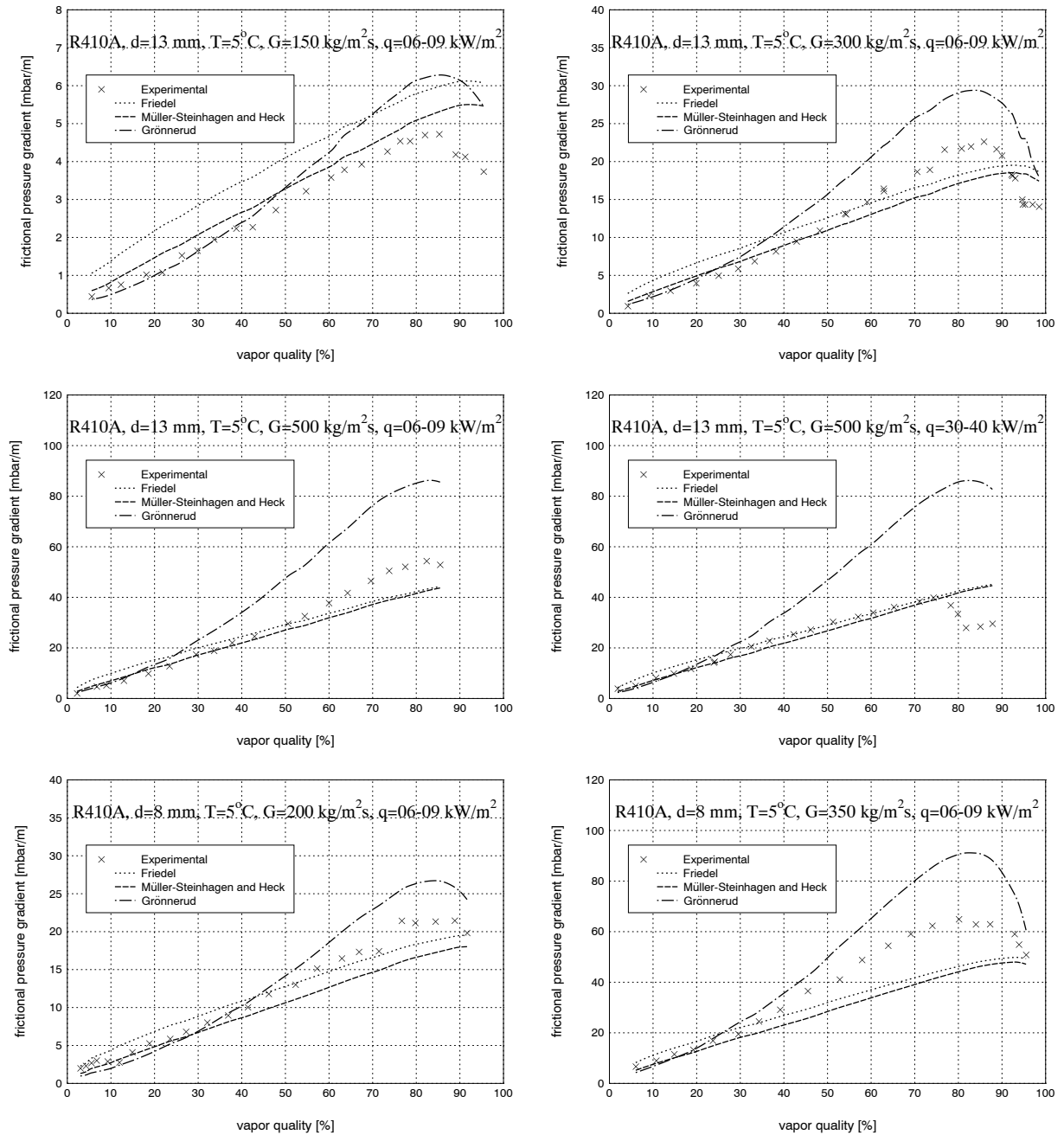


Figure 7.2: Frictional pressure gradients vs. three prediction methods for R410A at different experimental conditions.

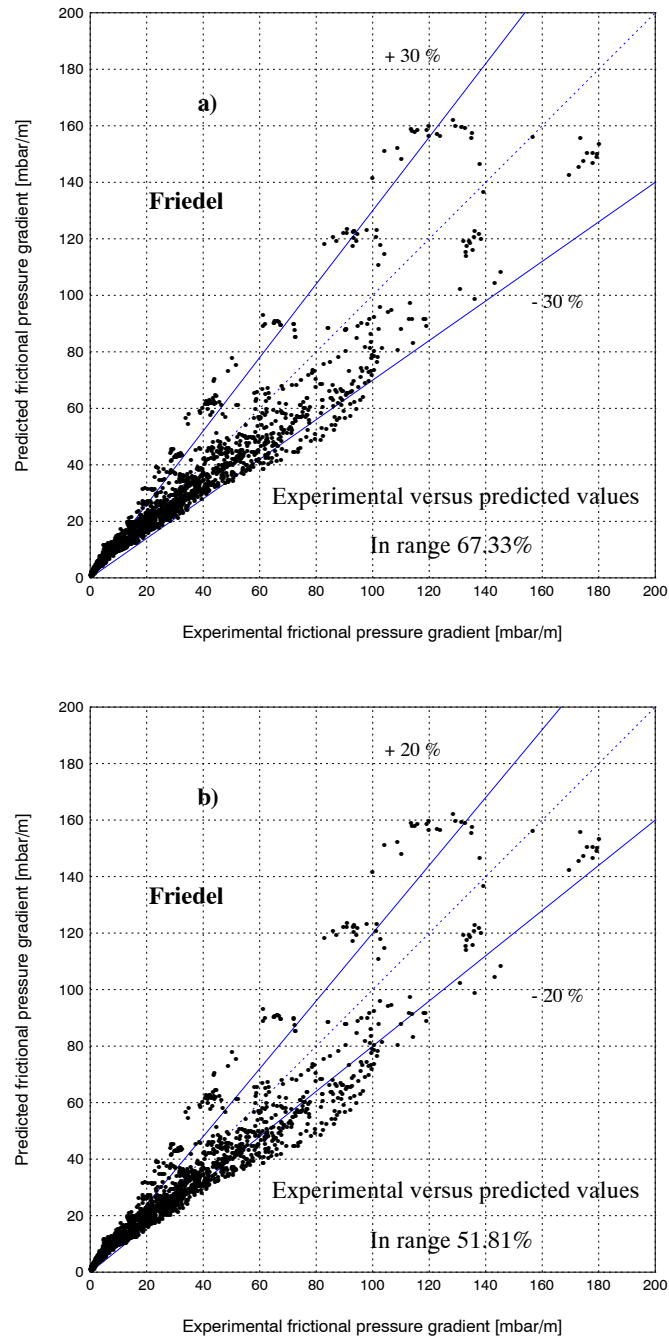


Figure 7.3: Comparisons of experimental to predicted values using Friedel correlation for the entire database: a) 67.33% are predicted within $\pm 30\%$, b) 51.81% are predicted within $\pm 20\%$.

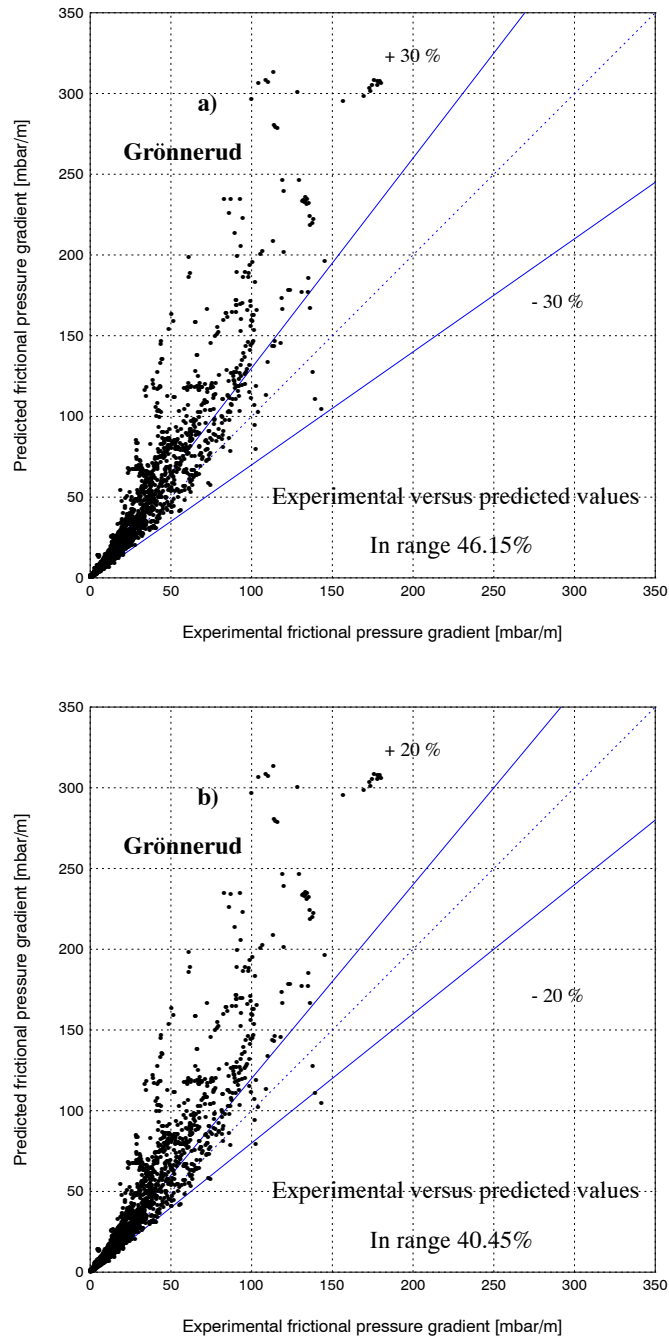


Figure 7.4: Comparisons of experimental to predicted values using Grönnerud correlation for the entire database: a) 46.15% are predicted within $\pm 30\%$, b) 40.45% are predicted within $\pm 20\%$.

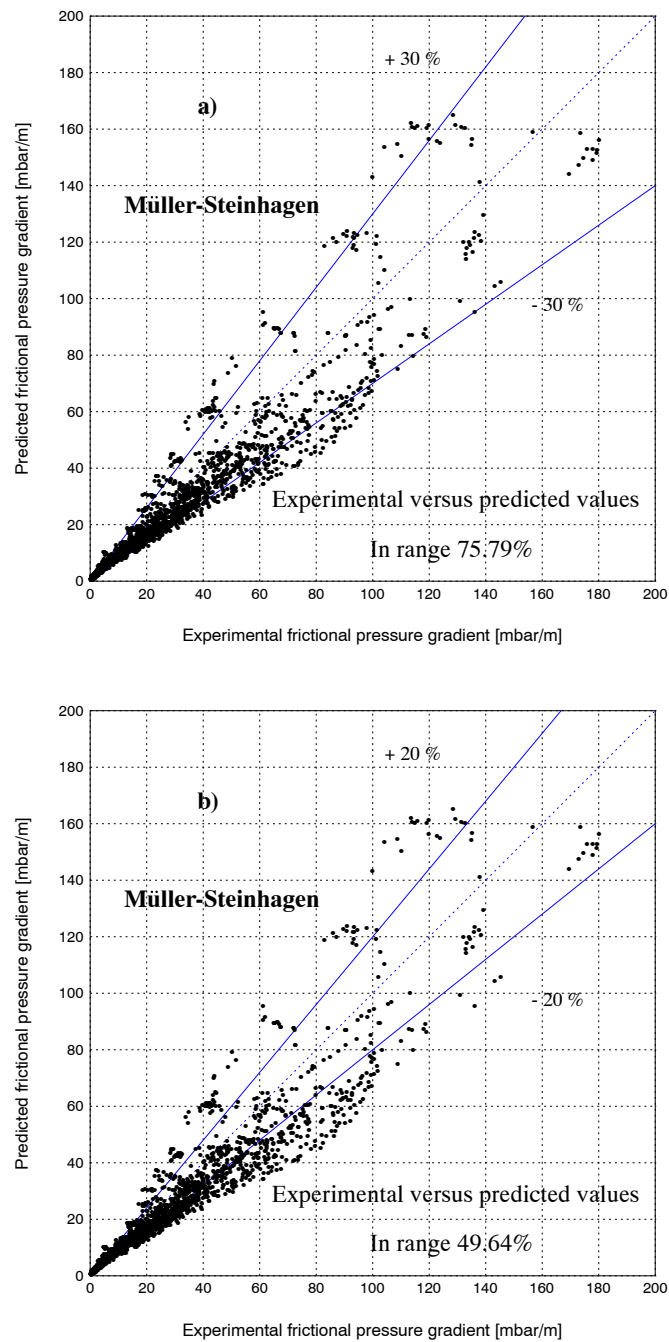


Figure 7.5: Comparisons of experimental to predicted values using Müller-Steinhagen and Heck correlation for the entire database: a) 75.79% are predicted within $\pm 30\%$, b) 49.64% are predicted within $\pm 20\%$.

7.2 New two-phase pressure drop model

7.2.1 Introduction

The new two-phase frictional pressure drop model is developed following a phenomenological approach, that is physically based on a simplified interfacial two-phase flow structure. The corresponding interfacial flow structure is determined using the recent Wojtan-Ursenbacher-Thome [155] flow pattern map described in Chapter 3. The main reasons to use this flow pattern map are:

- First, this flow pattern map has been experimentally validated.
- Second, this flow pattern map does not require any iterative calculations and it can be easily used for flow regime identification.
- Finally, the use of this flow pattern map fits the present flow pattern based pressure drop model into the unified approach of Thome and coworkers to model evaporation and condensation inside horizontal tubes.

7.2.2 Segregation of experimental data

The entire experimental data are segregated by flow regime as a previous step in the new model development. For the reasons mentioned above, the recent Wojtan-Ursenbacher-Thome is used for this task. For sake of simplicity and knowing that for a given set of experimental conditions a flow pattern map needs to be generated in order to accomplish the segregation process, it has been chosen to include in this section the flow pattern map for some representative sets of experimental parameters. The procedure to generate the flow pattern and the complete set of equations can be found in Chapter 3.

Table (7.1) shows the entire database segregated by flow regime using the recent Wojtan et al. flow pattern map. It has to be pointed out here that only experimental values where the complete test section was in the same flow regime are taken into account. This restriction is always verified for the adiabatic test section as no heat is added to the refrigerant, while for the diabatic test section the inlet and outlet vapor qualities were checked to verify that the entire test section was in the same regime. For this reason only 1745 experimental points have been used in new model development from the more than 2500 experimental values obtained during the experimental campaign (representing about 50% diabatic data and 50% adiabatic data).

It has to be pointed out here that the fixed value of the mass velocity appearing in the graphs depicted in Figs. (7.6)-(7.8) represents the value used for the void fraction calculation using Eq. (3.35). As the variation of this value practically does not affect the void fraction calculation for mass velocities above $50 \text{ kg/m}^2\text{s}$, a design condition for the mass velocity is assumed for simplicity in generating these graphs and this is the value appearing in the title of the graphs. In actual application of the of the flow pattern map and the new frictional pressure drop model, the actual mass velocity is used in calculations.

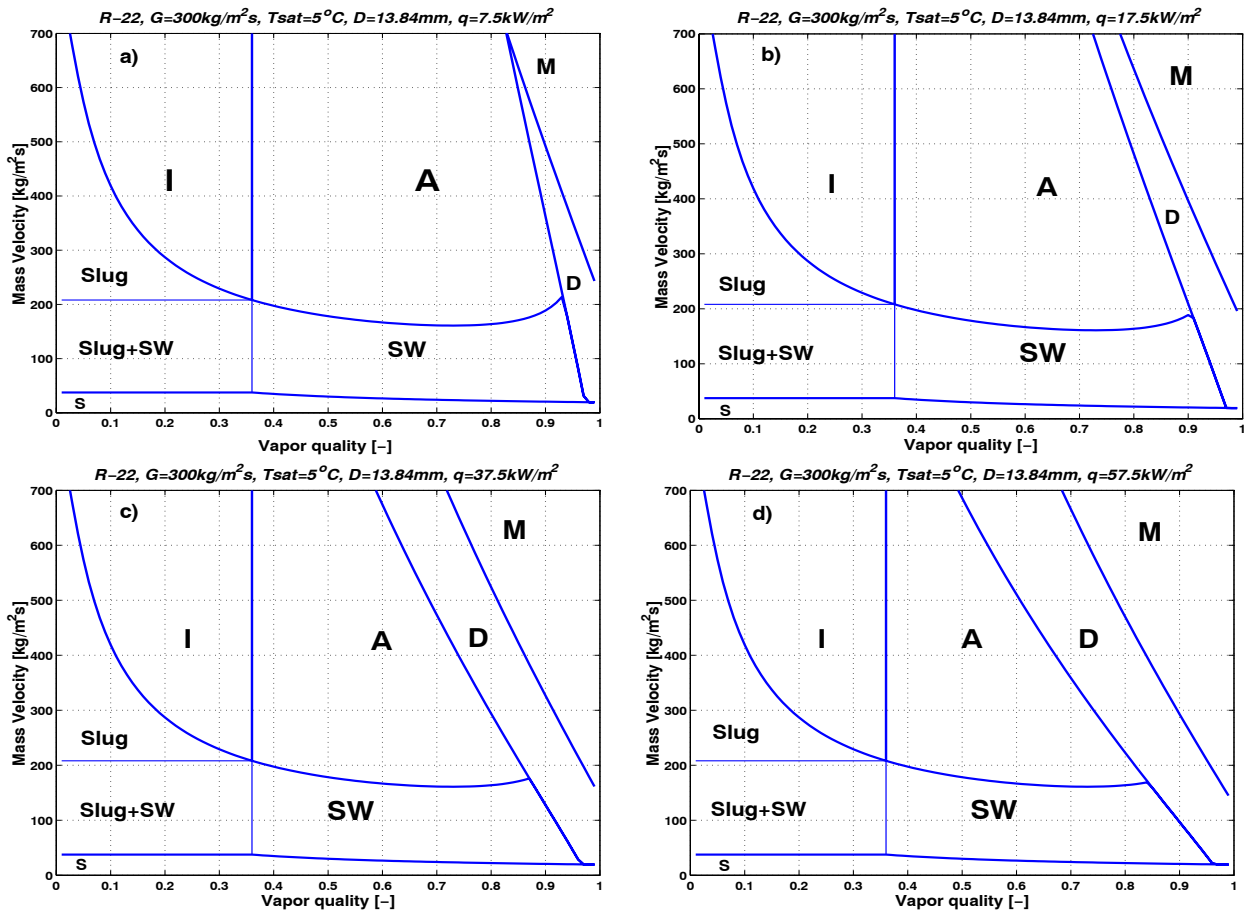


Figure 7.6: Flow pattern maps for R-22, $T_{sat} = 5^\circ\text{C}$, $D = 13.84 \text{ mm}$ at $G = 300 \text{ kg/m}^2\text{s}$ and heat fluxes: a) 7.5 kW/m^2 , b) 17.5 kW/m^2 , c) 37.5 kW/m^2 , d) 57.5 kW/m^2 .

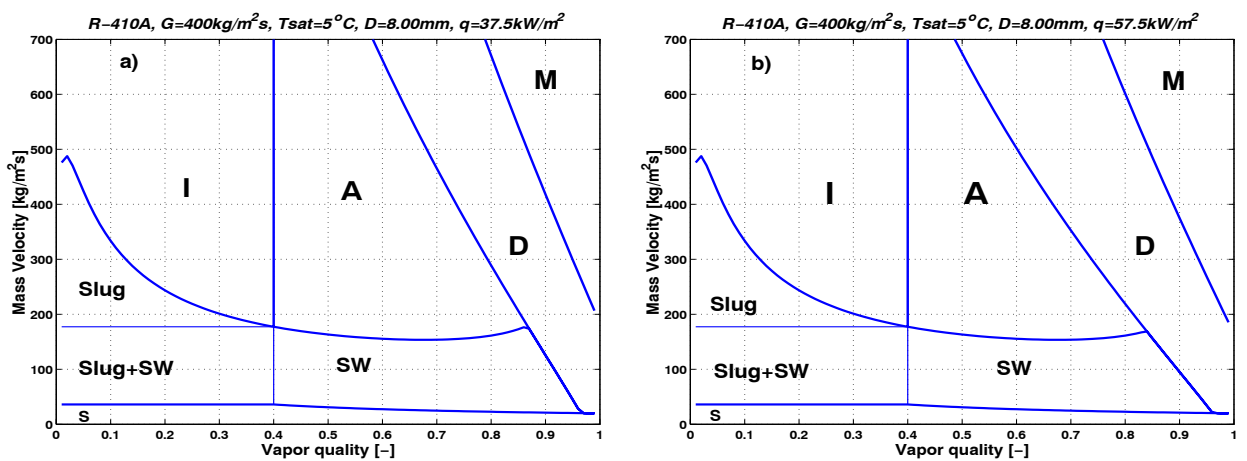


Figure 7.7: Flow pattern maps for R-410A, $T_{sat} = 5^\circ\text{C}$, $D = 8.00 \text{ mm}$ at $G = 400 \text{ kg/m}^2\text{s}$ and initial heat fluxes: a) 37.5 kW/m^2 , b) 57.5 kW/m^2 .

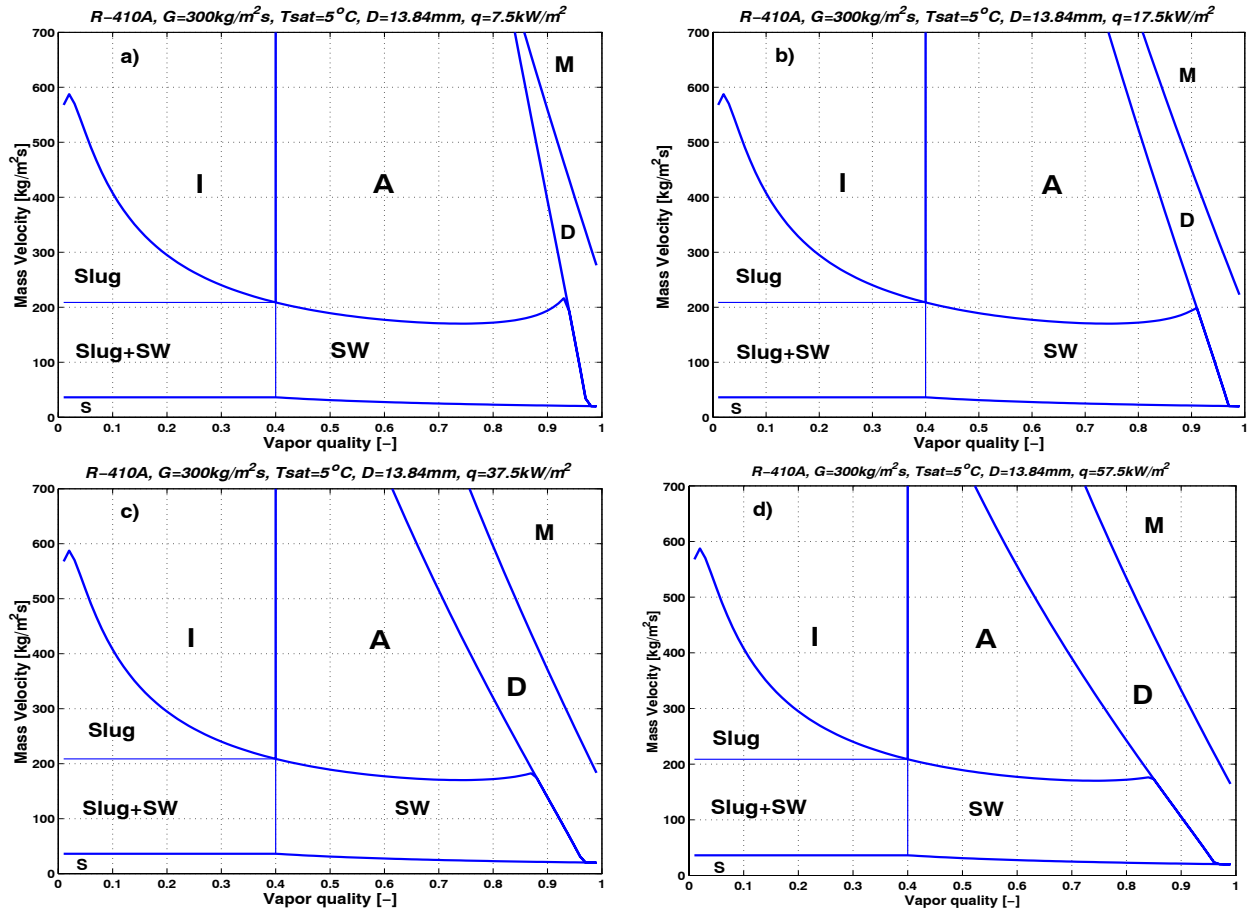


Figure 7.8: Flow pattern maps for R-410A, $T_{sat} = 5^\circ\text{C}$, $D = 13.84 \text{ mm}$ at $G = 300 \text{ kg/m}^2\text{s}$ and initial heat fluxes: a) 7.5 kW/m^2 , b) 17.5 kW/m^2 , c) 37.5 kW/m^2 , d) 57.5 kW/m^2 .

Segregated experimental values by flow regime									
Fluid	$D[\text{mm}]$	Slug+SW	SW	Slug	I	A	D	M	S
R134a	13.8	6	3	5	2	13	0	0	0
R22	8	28	20	18	12	75	21	17	0
R22	13.8	18	54	15	37	162	44	47	0
R410A	8	26	19	24	55	167	121	110	0
R410A	13.8	78	115	17	77	166	104	69	0
Total		156	211	79	183	583	290	243	0

Table 7.1: Segregated experimental values by flow regime using Wojtan et al. flow pattern map, where **S**= stratified flow, **SW**= stratified-wavy flow, **I**= intermittent flow, **A**= annular flow, **M**= mist flow and **D** represents the transition zone between annular and mist flow.

7.2.3 Model development

Hence, once the flow regime is known, a simplified interfacial structure can be assumed, and then a set of equations is proposed to determine two-phase pressure drop for that regime, while at the same time taking care not to have any jumps in the predicted values when crossing a flow transition boundary. Below, the new model and its calculation procedure for the different flow regimes is proposed and described.

Annular region (A)

According to the flow pattern map, about one-third of the experimental data were in the annular flow regime. Therefore, this regime will be treated first. The model for analysis is a simplified annular flow consisting of a liquid film and a gas core, as shown Fig. (7.9). Entrainment is neglected and the liquid film is assumed to be smooth and to have a uniform thickness δ around the circumference. These assumptions are not always valid but they allow a much more simplified model to be proposed.

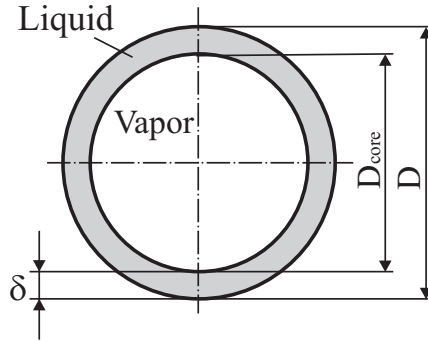


Figure 7.9: Simplified annular flow configuration.

The model is based on the steady-state gas and liquid phase momentum balance equations. Assuming equal average pressure gradients in the gas and liquid, which is generally valid in the absence of interfacial liquid level gradients, this leads to the following equation:

$$\frac{\Delta p}{L} = 4 \frac{\tau_i}{(D - 2\delta)} \quad (7.1)$$

Taking into account that generally $D \gg \delta$, Eq. (7.1) can be written as follows:

$$\frac{\Delta p}{L} = 4 \frac{\tau_i}{D} \quad (7.2)$$

The expression above states that the frictional pressure gradient is directly related to the interfacial shear stress τ_i and the tube diameter D . The interfacial shear stress represents the shear stress exerted by the gas on the liquid and is given by:

$$\tau_i = f_i \frac{1}{2} \rho_G (u_G - u_L)^2 \approx f_i \frac{1}{2} \rho_G u_G^2 \quad \text{if} \quad u_L \ll u_G \quad (7.3)$$

where f_i is the interfacial friction factor and u_G and u_L are the true average velocities defined in Chapter 2. The interfacial friction factor f_i remains unknown and is as always the most difficult parameter to model in two-phase flow. From Eqs. (7.2) and (7.3) and the present two-phase frictional pressure drop database in the annular flow regime obtained during the experimental campaign, the following new film flow correlation for f_i is proposed:

$$(f_i)_{annular} = 0.67 \underbrace{\left[\frac{\delta}{2R}\right]^{1.2}}_1 \underbrace{\left[\frac{(\rho_L - \rho_G)g\delta^2}{\sigma}\right]^{-0.4}}_2 \underbrace{\left[\frac{\mu_G}{\mu_L}\right]^{0.08}}_3 \underbrace{[We_L]^{-0.034}}_4 \quad (7.4)$$

where the non-dimensional groups include the following effects:

- Group 1: Film thickness effect relative to the internal radius of the tube R .
- Group 2: Related to the formation of interfacial waves with the characteristic wavelength similar to the film thickness. A more detailed description of this effect can be found in Appendix B.
- Group 3: The viscosity ratio of the gas and liquid phases.
- Group 4: The Surface tension effect is introduced by means of the liquid Weber We_L number (Eq. (2.30)).

The empirical constant and exponents were obtained statistically from the annular flow database. Hence, the frictional two-phase pressure drop can be now calculated with:

$$(\Delta p)_{annular} = 4 (f_i)_{annular} \left(\frac{L}{D}\right) \frac{\rho_G u_G^2}{2} \quad (7.5)$$

Slug + Intermittent (Slug+I)

These two flow regimes were treated together as was shown in the previous chapter, the respective experimental frictional two-phase pressure drops follow similar trends. This behaviour is consistent with Wojtan [153] observations regarding flow boiling heat transfer coefficients. Moreover, due to the unsteadiness of the flow characterizing these two regimes trying to capture this behaviour its quite complex. A common characteristic of both regimes is that all the tube perimeter is continuously wetted, explaining perhaps why their data have similar trends.

For the reasons mentioned above, and to avoid a jump at the transition with annular flow while also respecting the natural limit at $x = 0$, a good compromise was found by using the following expression:

$$(\Delta p)_{slug+intermittent} = \Delta p_{L0} \left(1 - \frac{\epsilon}{\epsilon_{IA}}\right)^{0.25} + (\Delta p)_{annular} \left(\frac{\epsilon}{\epsilon_{IA}}\right)^{0.25} \quad (7.6)$$

where Δp_{L0} is single-phase frictional liquid pressure drop (evaluated at $x = 0$), ϵ_{IA} is the void fraction at the intermittent to annular transition boundary x_{IA} and $(\Delta p)_{annular}$ is the two-phase frictional pressure drop evaluated at the actual vapor quality using annular flow equations.

Eq. (7.6) is an interpolation between the single-phase frictional liquid pressure drop ($x = 0$) and the two-phase frictional pressure drop $(\Delta p)_{annular}$ that would exist if the regime were annular for these flow conditions. Using void fraction for the interpolation procedure, this expression accomplishes two important purposes: first, it matches the correct limit at $x = 0$ (single-phase liquid flow). Second, it insures a smooth transition at the intermittent to annular transition without introducing any jump. In doing so, the model is in agreement with the experimental observations and bypasses these two drawbacks of some existing models.

Stratified-Wavy (SW)

In this regime, the parameter that defines the flow structure and the ratio of the tube perimeter in contact with the liquid and gas is the dry angle θ_{dry} shown in Fig. (7.10).

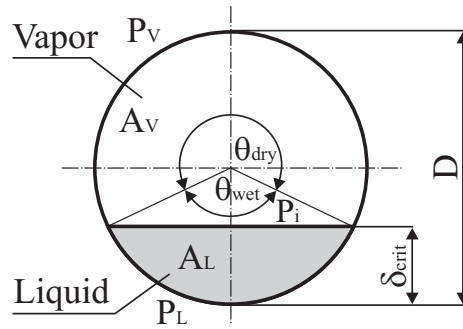


Figure 7.10: Simplified stratified flow configuration.

It is an experimental fact in stratified-wavy flow that liquid creeps up the sides of the tube to a varying extent. This effect significantly affects the interfacial perimeters P_i , P_L and P_G , as well as the interfacial friction factor f_i . In fact, for a fixed vapor quality x , θ_{dry} varies from 0 for $G_{wavy}(x)$ at the annular flow transition and to its maximum value of θ_{strat} for $G_{strat}(x)$ at the fully stratified flow transition. Several expressions have been proposed to capture this variation: a linear variation by Kattan et al. [78] and a quadratic interpolation by El Hajal [40]. In the recent work of Wojtan et al. [156] based on experimental heat transfer data for this region, they have proposed the following expression:

$$\theta_{dry} = \left[\frac{(G_{wavy} - G)}{(G_{wavy} - G_{strat})} \right]^{0.61} \theta_{strat} \quad (7.7)$$

where θ_{strat} is determined using the approximate expression, evaluated in terms of void fraction, proposed by Biberg [16],

$$\theta_{strat} = 2\pi - 2 \left\{ \begin{array}{l} \pi(1 - \epsilon) + \left(\frac{3\pi}{2}\right)^{1/3} [1 - 2(1 - \epsilon) + (1 - \epsilon)^{1/3} - \epsilon^{1/3}] \\ -\frac{1}{200}(1 - \epsilon)\epsilon[1 - 2(1 - \epsilon)[1 + 4((1 - \epsilon)^2 + \epsilon^2)] \end{array} \right\} \quad (7.8)$$

Using Eqs. (7.7) and (7.8) to determine θ_{dry} , the following equation is now proposed for the two-phase friction factor:

$$(f_{tp})_{stratified-wavy} = \theta_{dry}^* f_G + (1 - \theta_{dry}^*) (f_i)_{annular} \quad (7.9)$$

where $\theta_{dry}^* = \theta_{dry}/2\pi$, f_G is single-phase gas friction factor calculated using the classical definition

$$f_G = \frac{0.079}{Re_G^{0.25}} \quad \text{where} \quad Re_G = \frac{GxD}{\mu_G \epsilon} \quad (7.10)$$

and $(f_i)_{annular}$ is the interfacial friction factor for the annular flow regime described previously evaluated at the actual vapor quality.

The frictional two-phase pressure drop can now be calculated as follows:

$$(\Delta p)_{stratified-wavy} = 4(f_{tp})_{stratified-wavy} \left(\frac{L}{D}\right) \frac{\rho_G u_G^2}{2} \quad (7.11)$$

Slug+Stratified-Wavy (Slug+SW)

In this regime both low amplitude waves (which do not reach the top of the tube) and liquid slugs washing the top of the tube are observed. With increasing vapor quality in this zone, the frequency of slugs decreases and the waves become more dominant. This behaviour is highly chaotic and as a consequence is quite difficult to capture physically within a simplified model. A good compromise was found, as for the slug and intermittent regimes, by using the following expression:

$$(\Delta p)_{slug+SW} = \Delta p_{L0} \left(1 - \frac{\epsilon}{\epsilon_{IA}}\right)^{0.25} + (\Delta p)_{stratified-wavy} \left(\frac{\epsilon}{\epsilon_{IA}}\right)^{0.25} \quad (7.12)$$

where Δp_{L0} is the single-phase frictional liquid pressure drop (evaluated at $x = 0$), ϵ_{IA} is the void fraction at the intermittent to annular transition boundary and $(\Delta p)_{stratified-wavy}$ is the two-phase frictional pressure drop evaluated at the actual vapor quality using stratified-wavy flow equations.

Eq. (7.12) again insures a smooth transition at the intermittent to annular boundary and matches the correct limit for $x = 0$. The interpolation exponent is again 0.25 as in Eq. (7.6) and gives the best representation of the data.

Mist (M)

This regime is encountered when all the liquid is entrained in the gas core by the high velocity gas. The vapor phase is the continuous phase and the liquid flows in the form of droplets. In fact, it is not far from reality to consider the two phases to flow as a single phase possessing mean fluid properties. Under these conditions one can use the homogeneous flow theory in order to accurately predict two-phase frictional pressure drop values. Hence, the following expression is used to calculate the two-phase frictional pressure drop in this regime:

$$(\Delta p)_{mist} = 2 f_m \left(\frac{L}{D}\right) \frac{G^2}{\rho_m} \quad (7.13)$$

where ρ_m is the homogeneous density and is determined as

$$\rho_m = \rho_L(1 - \epsilon_H) + \rho_G \epsilon_H \quad (7.14)$$

and the homogeneous void fraction ϵ_H is

$$\epsilon_H = \frac{1}{1 + \frac{(1-x)\rho_G}{x\rho_L}} \quad (7.15)$$

The friction factor f_m is calculated introducing an homogeneous viscosity μ_m using single-phase equations as follows,

$$f_m = \frac{0.079}{Re_m^{0.25}} \quad \text{where} \quad Re_m = \frac{GD}{\mu_m} \quad (7.16)$$

and μ_m is determined using the Cicchitti (1960) expression:

$$\mu_m = x\mu_G + (1-x)\mu_L \quad (7.17)$$

This expression (Eq. 7.13) goes to the ideal limit of all gas flow at $x = 1$.

Dryout (D)

Analyzing the experimental results, it is obvious that there is not usually a step-wise jump from annular(A) to mist(M) flow. This transition regime between them is called dryout. The process of dryout starts at the top of the tube, where the liquid film is thinner, and takes place over a range of vapor qualities (from the inception of dryout at x_{di} at the top of the tube to the completion of dryout at x_{de} at the bottom of the tube) and thus ends when the fully developed mist flow regime is reached. This process is depicted in Fig. (7.11).

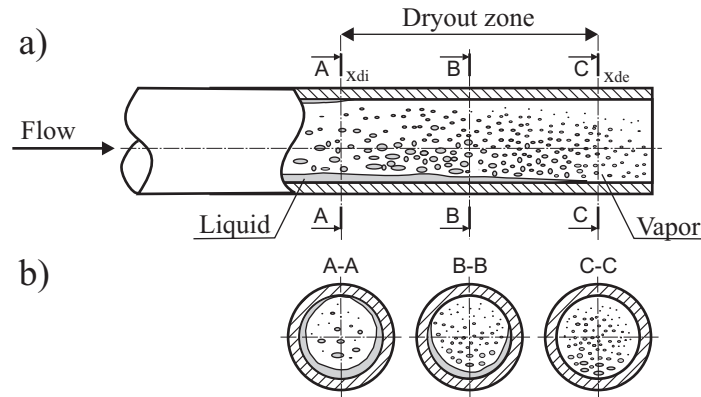


Figure 7.11: Dryout zone during evaporation in horizontal tube.

The following linear interpolation captures this variation and does not introduce any jump in the frictional pressure gradient being in agreement with the experimental observations:

$$(\Delta p)_{dryout} = (\Delta p)_{tp}(x_{di}) - \frac{x - x_{di}}{x_{de} - x_{di}} \left[(\Delta p)_{tp}(x_{di}) - (\Delta p)_{mist}(x_{de}) \right] \quad (7.18)$$

where x_{de} is the dryout completion quality and x_{di} is the dryout inception quality calculated, according with the flow pattern map, using the following expressions proposed by Wojtan et al. [153]:

$$x_{di} = 0.58e^{[0.52-0.235We_G^{0.17} Fr_G^{0.37}(\rho_G/\rho_L)^{0.25}(q/q_{crit})^{0.70}]} \quad (7.19)$$

$$x_{de} = 0.61e^{[0.57-5.8 \cdot 10^{-3}We_G^{0.38} Fr_G^{0.15}(\rho_G/\rho_L)^{-0.09}(q/q_{crit})^{0.27}]} \quad (7.20)$$

that are equivalent to Eqs. (3.54) and (3.55).

$(\Delta p)_{tp}(x_{di})$ is the frictional pressure drop at the inception quality calculated either with Eq. (7.5) for annular flow or Eq. (7.11) for stratified-wavy flow and $(\Delta p)_{mist}(x_{de})$ is the frictional pressure drop at the completion quality calculated with Eq. (7.13). At high mass velocities the value of x_{de} intersects that of x_{di} ; at these conditions, the dryout zone (D) no longer exists and a jump is contemplated between annular and mist flow.

Stratified (S)

The stratified flow regime was out of the possibilities of the present test facility as it occurs at very low mass velocities. Thus, no experimental values were obtained in this regime. In spite of an experimental verification the following calculation procedure is proposed for this regime:

– if $x \geq x_{IA}$ then

$$(f_{tp})_{stratified} = \theta_{strat}^* f_G + (1 - \theta_{strat}^*) (f_i)_{annular} \quad (7.21)$$

where $\theta_{strat}^* = \theta_{strat}/2\pi$, f_G is single-phase gas friction factor calculated with Eq. (7.10) and $(f_i)_{annular}$ is the interfacial friction factor for the annular flow regime described previously evaluated at the actual vapor quality.

The frictional two-phase pressure drop can now be calculated as follows:

$$(\Delta p)_{stratified}(x \geq x_{IA}) = 4(f_{tp})_{stratified} \left(\frac{L}{D}\right) \frac{\rho_G u_G^2}{2} \quad (7.22)$$

– if $x < x_{IA}$ then

$$(\Delta p)_{stratified}(x < x_{IA}) = \Delta p_{L0} \left(1 - \frac{\epsilon}{\epsilon_{IA}}\right)^{0.25} + (\Delta p)_{stratified}(x \geq x_{IA}) \left(\frac{\epsilon}{\epsilon_{IA}}\right)^{0.25} \quad (7.23)$$

where Δp_{L0} is single-phase frictional liquid pressure drop (at $x = 0$), ϵ_{IA} is the void fraction at the intermittent to annular transition boundary and $(\Delta p)_{stratified}(x \geq x_{IA})$ is the two-phase frictional pressure drop evaluated at the actual vapor quality using stratified flow equations for $x \geq x_{IA}$.

Bubbly (B)

Bubbly flows are not addressed these occur at mass velocities that are beyond the range of present interest. The bubbly flow transition from intermittent flow remains the same as in the original map, see Wojtan [155].

7.2.4 Comparisons of experimental to predicted values

This section presents comparisons of experimental to predicted values obtained using the new two-phase frictional pressure drop model.

Fig. (7.12) depicts comparisons of the entire database to predicted values. The new method predicts 82.3% within $\pm 30\%$ and 64.71% within $\pm 20\%$. Taking into account that the range of experimental conditions included a wide range of experimental conditions (fluids, diameter, mass velocities, heat fluxes), the method predicts very accurately the experimental data. The values for all the database versus the new and previous methods are summarized in Table (7.2).

Compilation of statistical results		
	$\pm 20\%$	$\pm 30\%$
Friedel	67.33%	51.81%
Grönnerud	46.15%	40.45%
Müller-Steinhagen and Heck	75.79%	49.64%
New Method	82.30%	64.71%

Table 7.2: Compilation of percentages of the database within an specific range for the new proposed model and three existing methods.

In order to check the reliability of the new model, Figs. (7.13) and (7.14) depict comparisons of experimental to predicted values when the fluid is changed for both internal tube diameters. Figs. (7.15) and (7.16) show comparisons for both fluids when the tube internal diameter is changed. It is deduced from the figures that changing these two important parameters does not have an effect on the accuracy of the predictions attesting for the reliability of the new method.

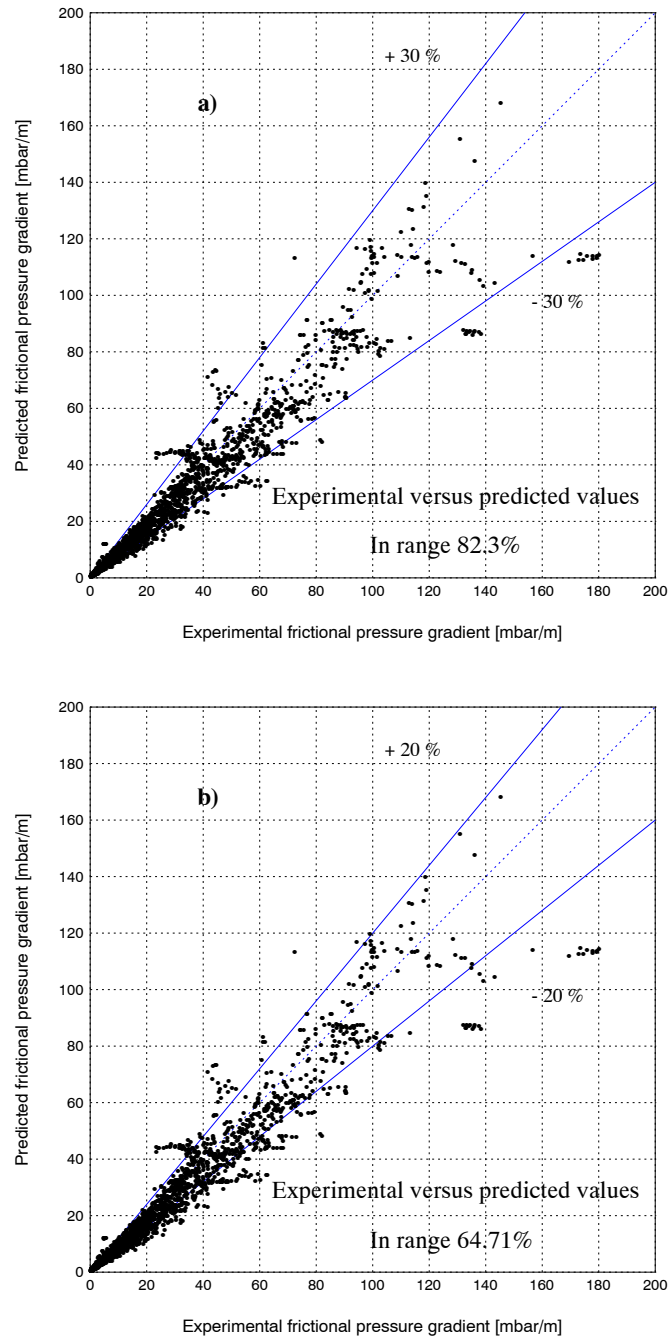


Figure 7.12: Comparisons of experimental to predicted values for the entire database: a) 82.30% are predicted within $\pm 30\%$, b) 64.71% are predicted within $\pm 20\%$.

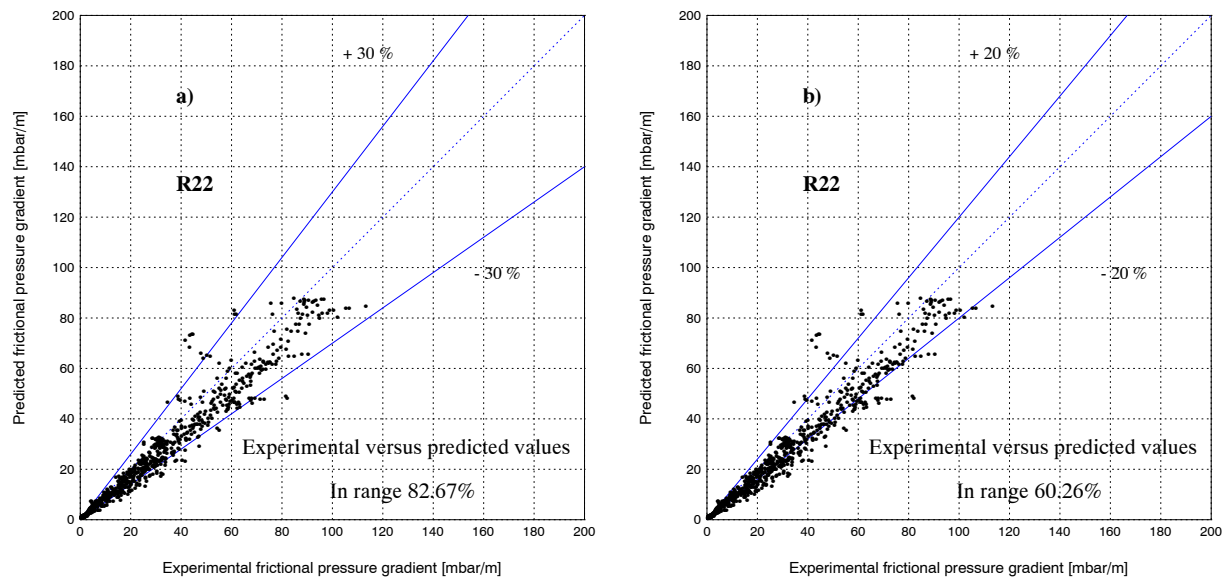


Figure 7.13: Comparisons of experimental to predicted values for R22 and both tested diameters: a) 82.67% are predicted within $\pm 30\%$, b) 60.26% are predicted within $\pm 20\%$.

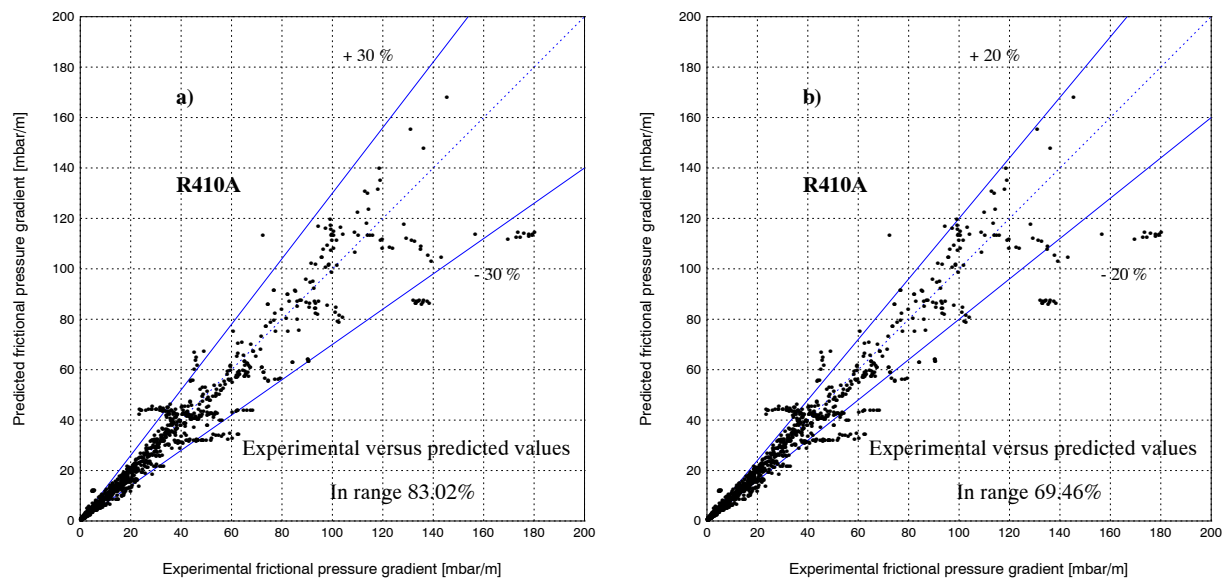


Figure 7.14: Comparisons of experimental to predicted values for R410A and both tested diameters: a) 83.02% are predicted within $\pm 30\%$, b) 69.46% are predicted within $\pm 20\%$.

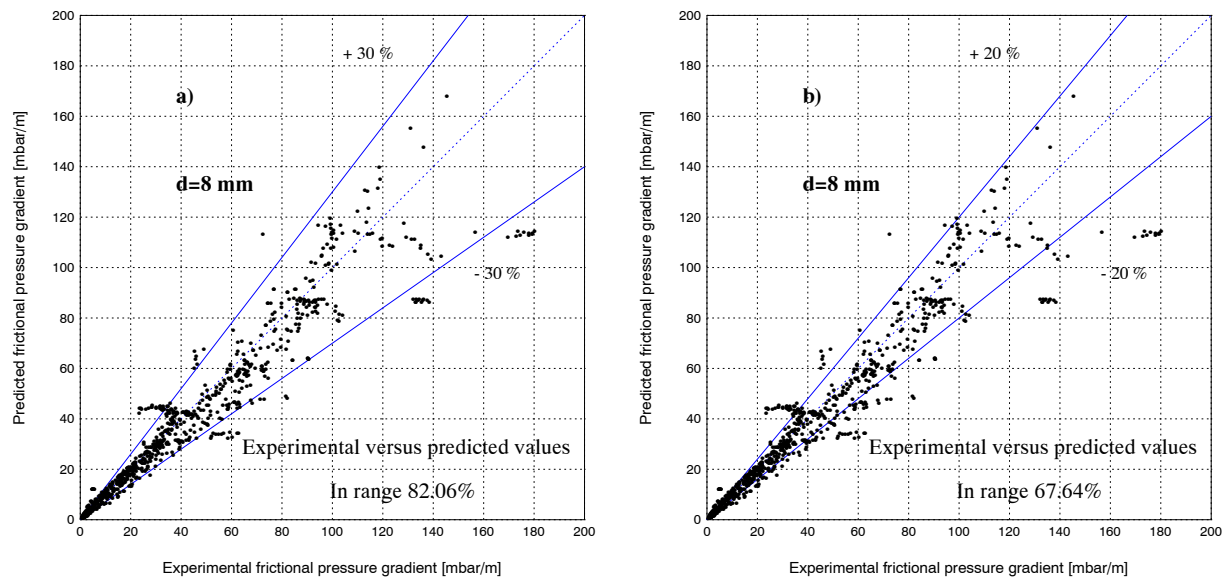


Figure 7.15: Comparisons of experimental to predicted values for $d = 8 \text{ mm}$ and both tested fluids: a) 82.06% are predicted within $\pm 30\%$, b) 67.64% are predicted within $\pm 20\%$.

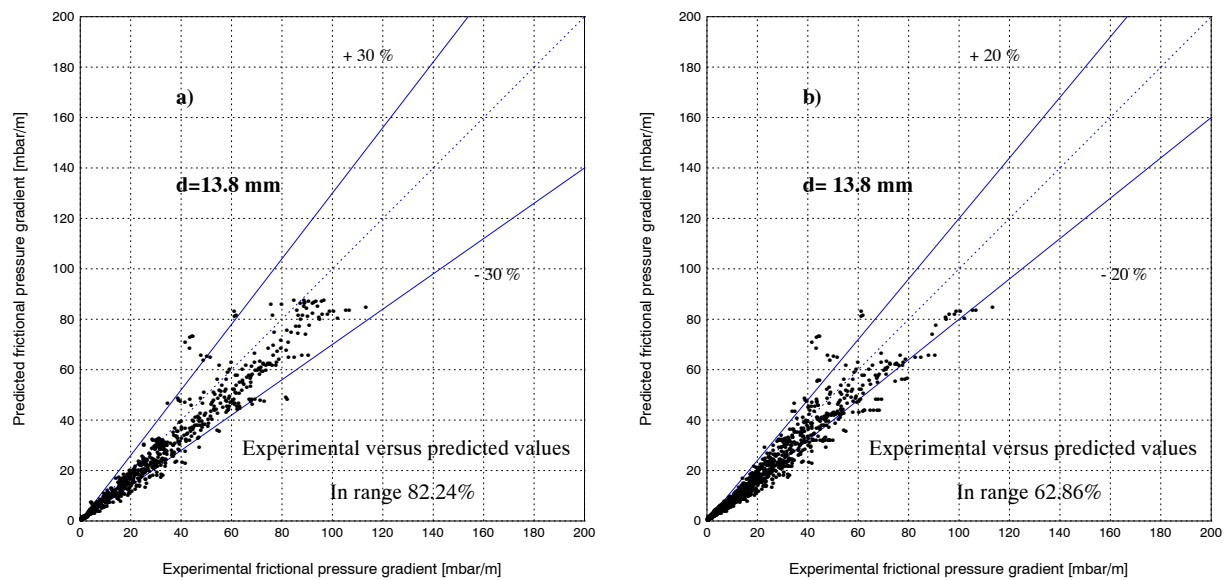


Figure 7.16: Comparisons of experimental to predicted values for $d = 13 \text{ mm}$ and both tested diameters: a) 82.24% are predicted within $\pm 30\%$, b) 62.86% are predicted within $\pm 20\%$.

Fig. (7.17) shows comparisons of experimental to predicted values for the entire database segregated by flow regime. For the sake of simplicity, the mist and dryout results are not shown in this figure but a similar behaviour was observed. It has to be pointed that pressure drop experimental values in the stratified-wavy (SW) and slug+stratified-wavy (Slug+SW) regimes were in the range of $0 - 8 \text{ mbar}$ and trying to accurately predict such low values is a difficult task because small deviations can induce large errors. This later feature assesses the quality of the proposed model.

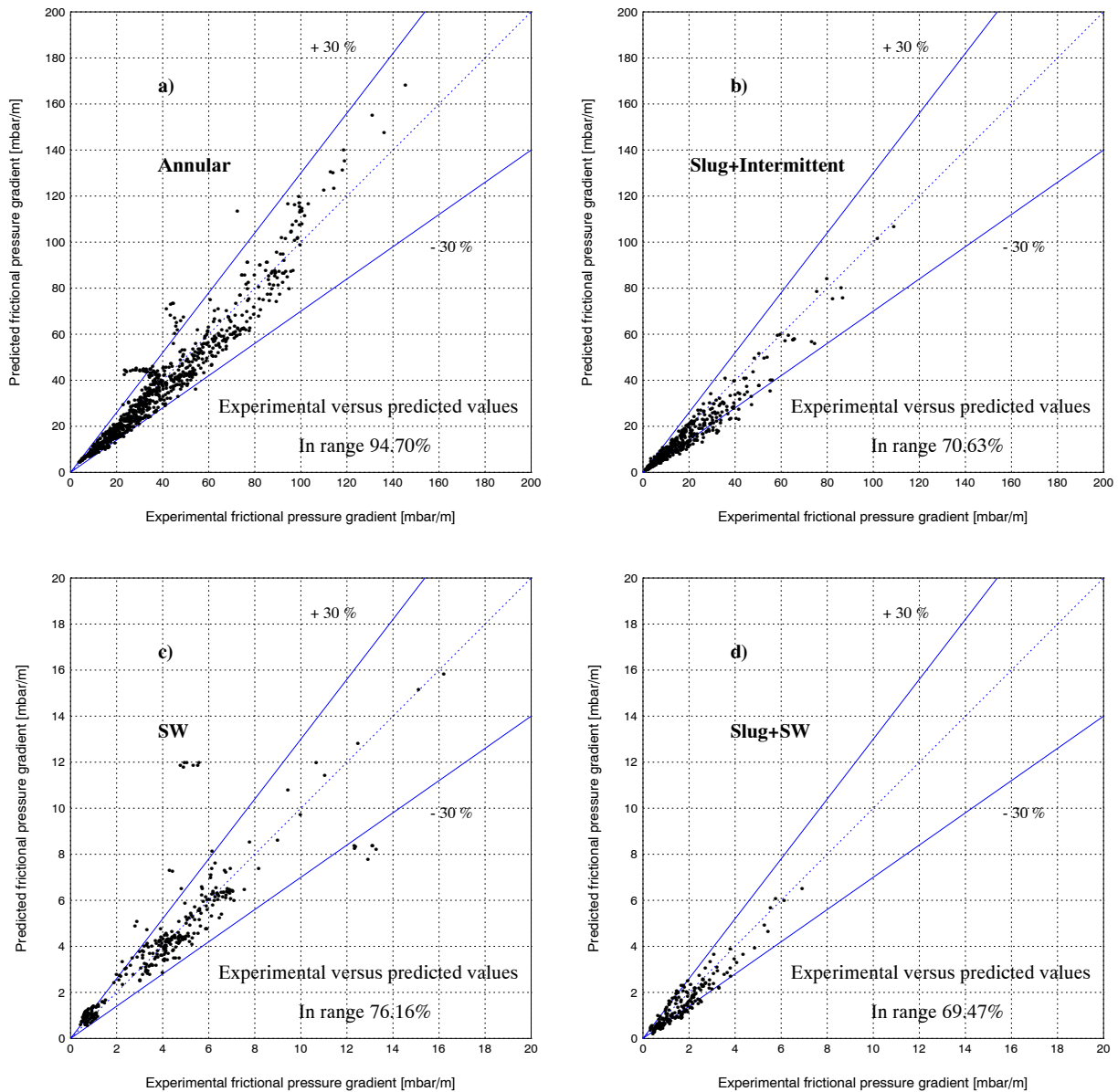


Figure 7.17: Comparisons of experimental to predicted values for the entire database segregated by flow regime: a) annular, b) Slug+Intermittent, c) SW, d) Slug+SW.

Thus, it has been shown that the new two-phase frictional prediction model from a statistical point of view is able to very accurately predict the experimental values. The reliability of the proposed model has also been proven but still a question remains open: Does the new model capture the

trends observed in the two-phase frictional pressure drops vs. vapor quality? This latter is crucial for the thermal optimization of evaporators. Figs. (7.18)-(7.22) show experimental and predicted values plotted vs. quality for a selected set of experimental conditions. The new model follows the experimental trends quite well and it is able to capture reasonably well the position and a little less so the magnitude of the characteristic peak at high vapor qualities.

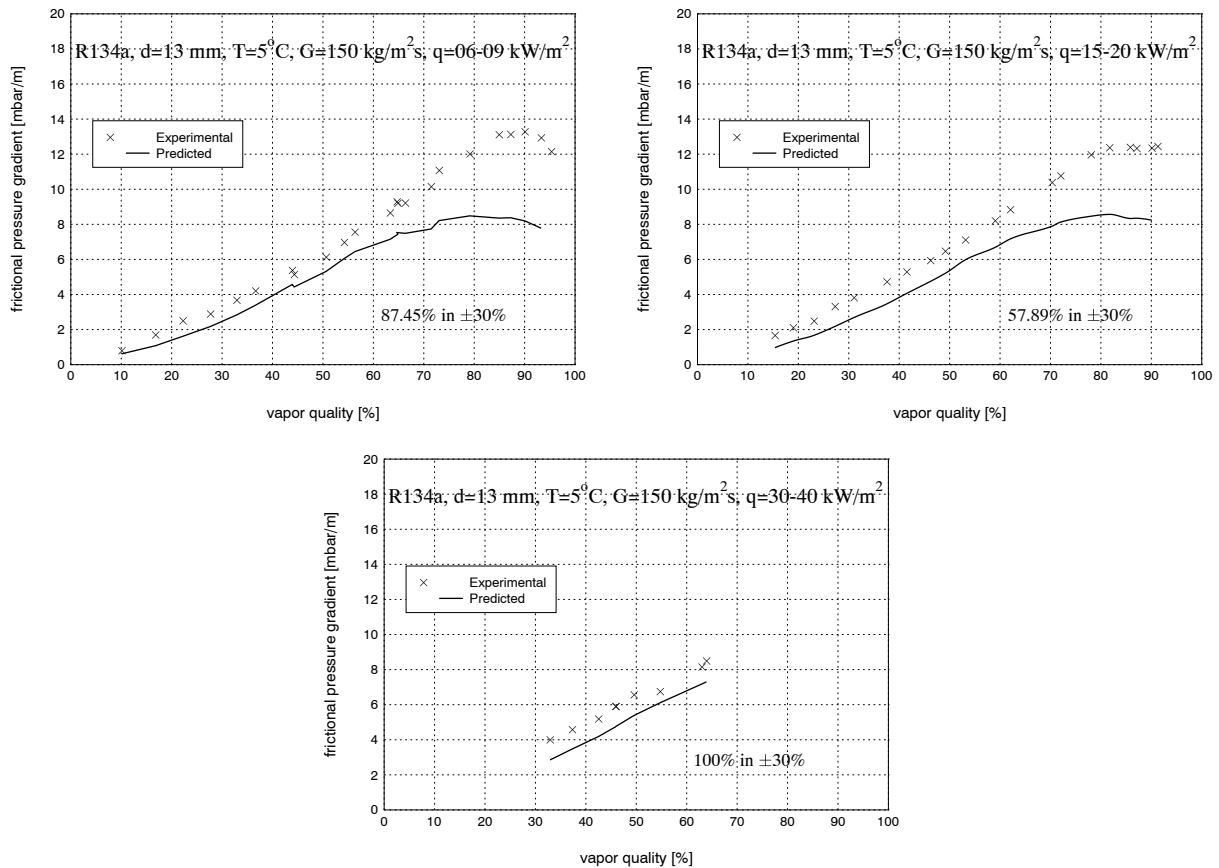


Figure 7.18: Experimental and predicted values vs. vapor quality for R134a at different experimental conditions.

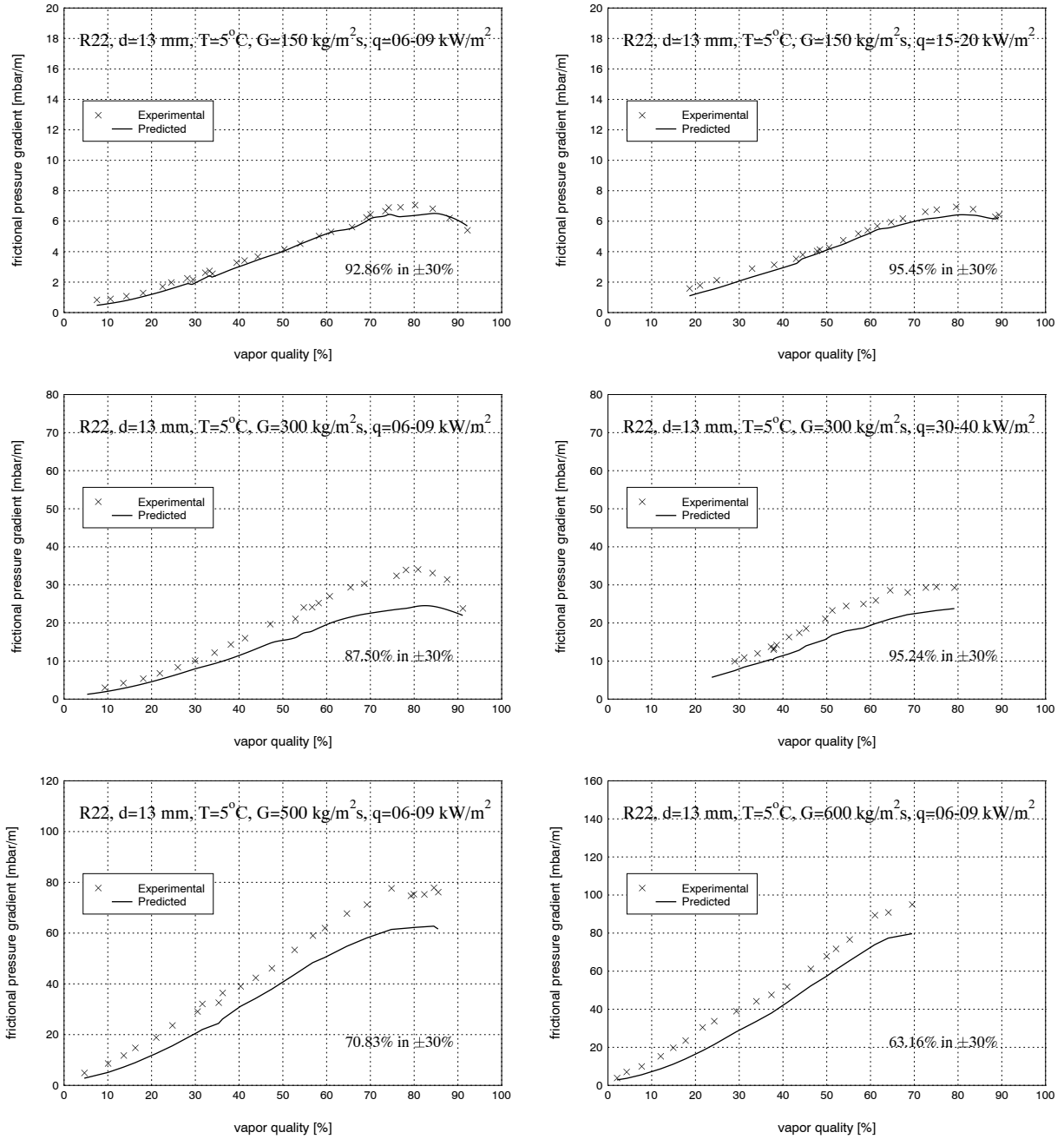


Figure 7.19: Experimental and predicted values vs. vapor quality for R22 at different experimental conditions and $d = 13.8\text{ mm}$.

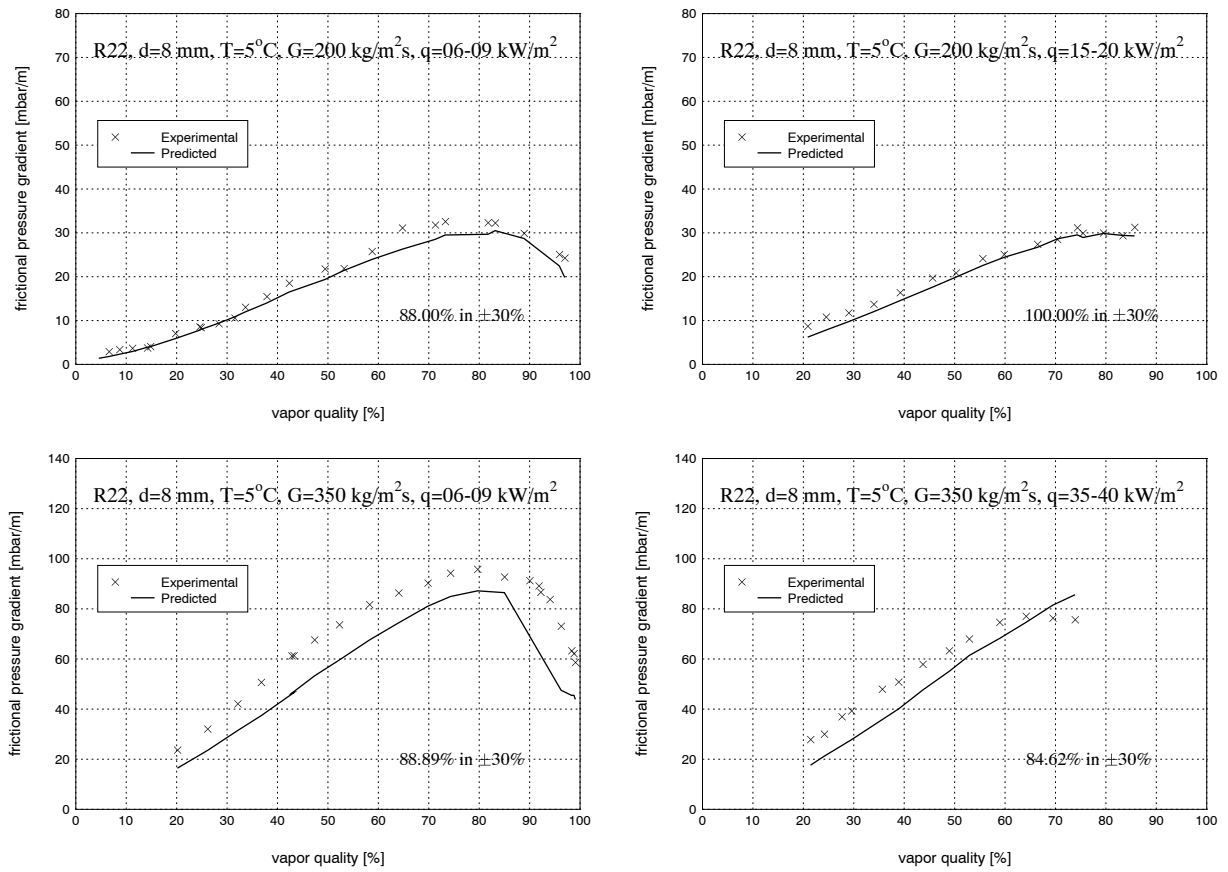


Figure 7.20: Experimental and predicted values vs. vapor quality for R22 at different experimental conditions and $d = 8\text{ mm}$.

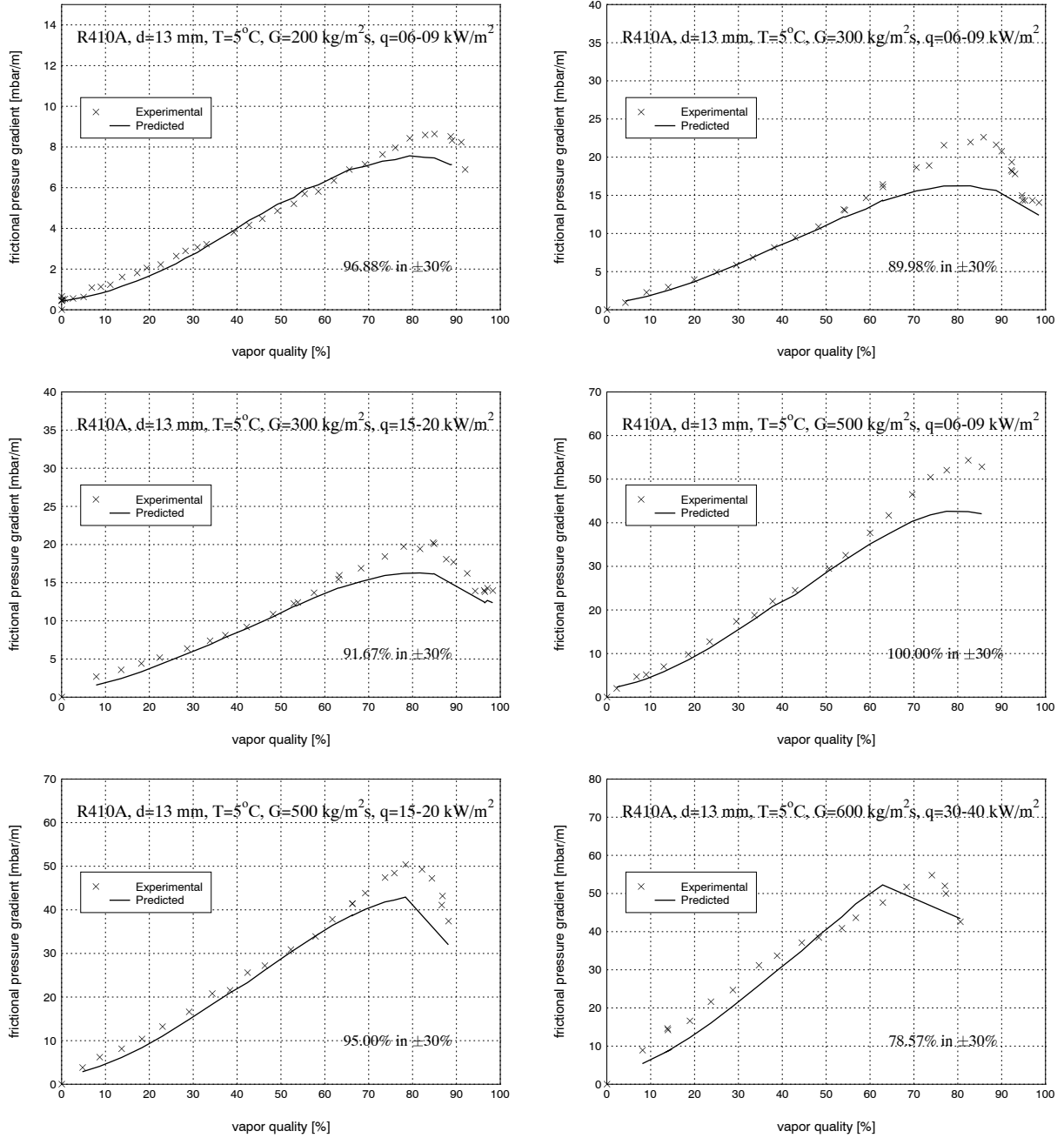


Figure 7.21: Experimental and predicted values vs. vapor quality for R410A at different experimental conditions and $d = 13.8\text{ mm}$.

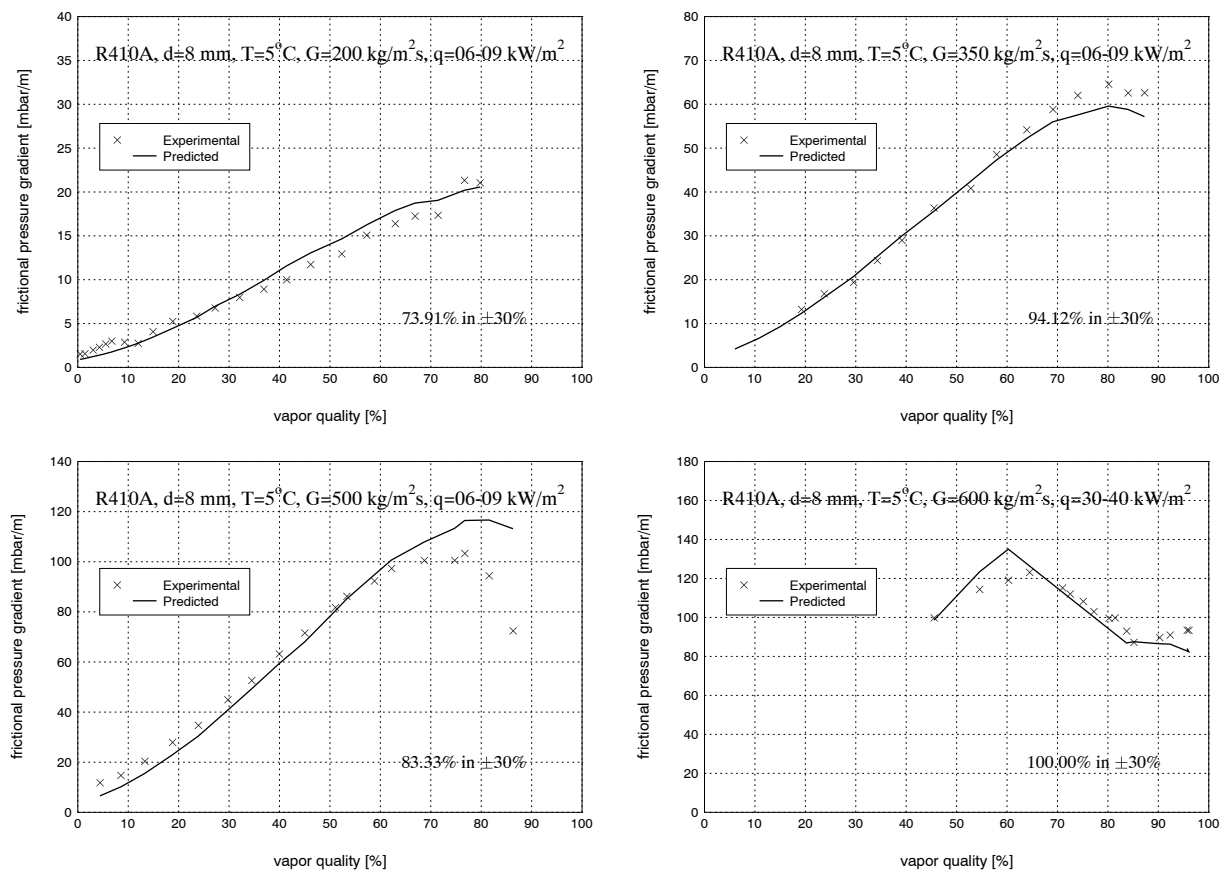


Figure 7.22: Experimental and predicted values vs. vapor quality for R410A at different experimental conditions and $d = 8$ mm.

Comments on the attributes of the new flow pattern based method:

- It is more accurate (according to Table (7.2)).
- It better follows the variation in pressure gradient with vapor quality.
- It captures the peak in the pressure gradient at high vapor qualities.
- It handles mist flow and the dryout region.
- It goes to the correct limits at $x = 0$ (single-phase liquid flow) and at $x = 1$ (single-phase gas flow).
- It explicitly includes the effect of interfacial waves.
- It includes the effect of interfacial flow structure (such as partially dry perimeter) via the flow pattern map.
- It is based on the actual mean velocities of the phases via the void fraction function rather than superficial velocities.

Furthermore, in thermal design with a vapor quality change from $x = 0.2$ at the inlet to $x = 1$ at the outlet, it is most important that the two-phase pressure gradient is calculated accurately where the gradients are high. For example, a 20% error at $x = 0.2$ is insignificant in the total pressure drop calculation. Hence, the present method that works very well in annular flow (see Fig. (7.17a)) and that captures the position of the peak will give much better total pressure drop predictions than the other methods.

7.3 Conclusions

The experimental results were compared to three recommended two-phase frictional pressure drop correlations: Friedel, Grönnerud and Müller-Steinhagen and Heck. While all three provided a reasonable agreement for some particular set of experimental conditions, they either significantly overpredicted or underpredicted the data for most of the others. Also, the methods did not reliably capture the variation in two-phase frictional pressure drop versus vapor quality, which is necessary for such methods to be useful for the thermal optimization of evaporators. Hence, the development of new two-phase frictional pressure drop model based on flow pattern map is justified. Then, the experimental data were segregated by flow regime using the recent Wojtan-Ursenbacher-Thome flow pattern map in order to develop the two-phase frictional pressure drop model based on flow pattern map, the new model is introduced and the development procedure is detailed. Comparisons with the database show that the new model is able to accurately and reliably predict experimental values and, furthermore, the variation of the frictional pressure drop vs vapor quality is well captured.

Chapter 8

Conclusions

As the first step in this work, a comprehensive experimental study was undertaken in order to obtain accurate two-phase pressure drop values during evaporation of refrigerants in horizontal tubes. The experimental conditions were chosen to obtain experimental values over a wide range of test parameters so that the effect of each parameter could be easily identified. The range of experimental conditions covered were: three refrigerants (low, medium and high pressure, respectively), two internal tube diameters, eight mass velocities and four heat fluxes. In addition, using water as heating fluid we were able to cover the entire range of vapor quality. Fulfilling these experimental requirements imposed a modification of the existing LTCM experimental facility and the implementation of new test sections. The new two-zone test sections allowed tests to (i) be run under both diabatic and adiabatic conditions simultaneously, (ii) to obtain two-phase pressure drop values for nearly every flow regime and (iii) to validate the data reduction procedure used to obtain the frictional component of the pressure drop. The campaign acquired 2543 experimental two-phase pressure drop values covering a wide range of experimental conditions and five flow regimes.

Next, based on a comprehensive state-of-the-art review and comparison versus leading two-phase frictional pressure drop prediction methods, it was proven that none of these methods were able to accurately and reliably predict the present experimental values. While leading methods provided partial agreement for a particular set of experimental parameters, they either significantly overpredicted or underpredicted the data for a different set of test variables. Furthermore, they did not adequately capture the trends observed in the two-phase frictional pressure drop vs. vapor quality nor the characteristic peak in the data at high vapor quality. Hence, it has been shown that none of the existing methods was reliable for optimizing the thermal-hydraulics of a direct-expansion evaporator, even though statistically they are not that bad when considering the normal situation for the prediction of two-phase frictional pressure drops.

For the reasons mentioned above, an analytical study was undertaken in order to develop a new two-phase frictional pressure drop prediction method. It has been shown in the literature that models developed based on a so called "phenomenological approach" could provide more accurate and realistic predictions as the interfacial structure between the phases is taken into account. Based on that, a phenomenological approach was chosen in the present study to develop a new two-phase pressure drop prediction method. To do this, the interfacial structure must be known in advance, which can be determined based on a flow pattern map. Hence, based on a comprehensive literature review of existing flow pattern maps, the recent Wojtan-Ursenbacher-Thome map was chosen to provide the corresponding interfacial structure needed for the development of the new model.

Hence, the entire experimental data were segregated by flow regime using this flow pattern map. Because about one-third of the experimental data were in the annular flow regime, this particular geometry was used as a starting point for model development and then extended to other flow regimes. The new model treats each flow regime (i.e. interfacial structure) separately and then ensures a smooth transition at the flow regime boundaries (no jump in pressure gradient), being in agreement with the experimental observations. Another important feature of the proposed model is that it matches the correct limits at $x = 0$ (single-phase liquid flow) and at $x = 1$ (single-phase gas flow).

Finally, based on a statistical analysis, it is concluded that the New Two-Phase Frictional Pressure Drop Model Based on Flow Pattern Map successfully predicts the present experimental data and is able to provide much better predictions than existing methods. It is recommended for optimizing the thermal-hydraulics of a direct-expansion evaporators.

The main advantages of the new method relative to previous methods are summarized below:

- It has been developed based on a 'phenomenological approach' as the interfacial structure of the various flow regimes is taken into account.
- It includes explicitly the effects of interfacial waves and flow patterns.
- It ensures smooth transitions (no jumps) between flow regimes, being in agreement with the experimental observations.
- It matches the correct limits for single-phase flow (single-phase liquid flow at $x = 0$ and single-phase gas flow at $x = 1$).
- It presents a reasonable degree of simplicity as no iteration is required for its application.
- It successfully predicts experimental data, based on a statistically based, and their change of trend with flow pattern.
- It captures the variation of the frictional pressure drop versus vapor quality, which is crucial for optimizing the thermal-hydraulics of evaporators.

Future work should extend comparison of the new model to other fluids and databases. This model should also be compared to two-phase pressure drops for in-tube condensing flows and modified to account for any differences arising from film condensation on the upper perimeter of stratified types of flow and the flow pattern map for condensation. Furthermore, two-phase pressure drops in U-bends and downstream of U-bends should also be investigated.

Appendix A

Fluid Physical Properties

Physical Properties							
Fluid	$T_{Sat}[^{\circ}C]$	$\rho_L[kg/m^3]$	$\rho_G[kg/m^3]$	$\mu_L[kg/ms]$	$\mu_G[kg/ms]$	$h_L[kJ/kg]$	$h_G[kJ/kg]$
R134a	0	1295	14.53	0.000331	1.08E-05	49.17	246.6
	5	1279	17.26	0.000312	1.10E-05	55.81	249.4
	10	1261	20.38	0.000294	1.12E-05	62.54	252.1
R22	0	1285	21.22	0.000232	1.19E-05	44.59	250.0
	5	1268	24.78	0.000226	1.21E-05	50.49	251.7
	10	1250	28.81	0.000220	1.23E-05	56.46	253.4
R410A	0	1176	30.67	0.000163	1.23E-05	56.46	277.0
	5	1155	35.95	0.000153	1.25E-05	63.89	278.4
	10	1133	41.98	0.000144	1.27E-05	71.44	279.6

Physical Properties							
Fluid	$P_{Sat}[bar]$	$k_L[W/mK]$	$k_G[W/mK]$	$c_{pL}[kJ/kgK]$	$c_{pG}[kJ/kgK]$	$\sigma[N/m]$	$P_{red}[-]$
R134a	2.93	0.09941	0.01179	1.308	0.9034	0.01157	0.07208
	3.49	0.09709	0.01222	1.327	0.9286	0.01085	0.08608
	4.15	0.09477	0.01264	1.346	0.9553	0.01015	0.1021
R22	4.97	0.1001	0.009396	1.160	0.7229	0.01174	0.09997
	5.83	0.09762	0.009696	1.173	0.7436	0.01099	0.1173
	6.80	0.09514	0.009996	1.187	0.7660	0.01025	0.13680
R410A	7.98	0.1139	0.01243	1.453	1.1180	0.01174	0.1622
	9.33	0.1108	0.01282	1.472	1.1700	0.01099	0.1896
	10.85	0.1076	0.01320	1.495	1.2280	0.01025	0.2203

Table A.1: Physical properties for fluids used during the experimental campaign at three different saturation temperatures.

Appendix B

Liquid-Vapor Interfaces

Instabilities associated with liquid-vapor interfaces can have a significant impact on the pressure drop (as well as on heat and mass transfer) during phase-change processes. Often these instabilities cause a change in the morphology of the two-phase system at a particular set of transition conditions. Altering the interface morphology results in changes in transport properties at the interface.

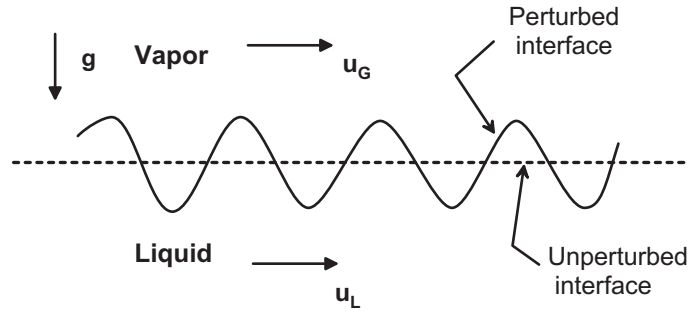


Figure B.1: Perturbed vapor-liquid interface.

The one-dimensional Taylor instability wavelength λ_T for the unsupported liquid film is:

$$\lambda_T \left[\frac{(\rho_L - \rho_G)}{\sigma} \right]^{1/2} = 2\pi\sqrt{3} \quad (\text{B.1})$$

and this is related to the formation of interfacial waves. If the interfacial waves have characteristics wavelengths similar to the film thickness, then substituting δ for λ_T means that the interfacial roughness $\Delta\delta_i$ will be approximately scaled as

$$\Delta\delta_i \propto \left[\frac{(\rho_L - \rho_G)g\delta^2}{\sigma} \right]^k \quad (\text{B.2})$$

where term inside the brackets is non-dimensional.

Bibliography

- [1] S. S. Agrawal, G. A. Gregory, and G. W. Govier. An analysis of horizontal stratified two phase flow in pipes. *Can. J. Chem. Eng.*, 51:280–286, 1973.
- [2] N. Andritsos and T. J. Hanratty. Influence of interfacial waves in stratified gas-liquid flows. *AIChE Journal*, 33(3):444–454, 1987.
- [3] C. Aprea, A. Greco, and G. P. Vanoli. Local heat transfer coefficients and pressure drop during evaporation in a smooth horizontal tube. In *Proceedings of IMECE2002*, New Orleans Louisiana, 2002.
- [4] M. M. Awad and Y. S. Muzychka. A simple asymptotic compact model for two-phase frictional pressure gradient in horizontal pipes. In *Proceedings of IMECE2004*, Anaheim, California, 2004.
- [5] B. J. Azzopardi. Drops in annular two-phase flow. *Int. J. Multiphase Flow*, 23:1–53, 1997.
- [6] S. Badie, C. P. Hale, C. J. Lawrence, and G. H. Hewitt. Pressure gradient and holdup in horizontal two-phase gas-liquid flows with low liquid loading. *Int. J. Multiphase Flow*, 26:1525–1543, 2000.
- [7] O. Baker. Design of pipe lines for simultaneous flow of oil and gas. *Oil and Gas J.*, 53:185–190, 1954.
- [8] J. Bandel. *Druckverlust und Wärmeübergang bei der verdampfung siedender kältemittel im durchströmten waagerechten rohr*. PhD thesis, University of Karlsruhe, 1973.
- [9] S. G. Bankoff. A variable density single-fluid model two-phase flow with particular reference to steam-water. *J. Heat Transfer*, 11(Series B):265–272, 1960.
- [10] D. Barnea. A unified model for predicting flow pattern transitions for the hole range of pipe inclinations. *Int. J. Multiphase Flow*, 13:1–12, 1987.
- [11] C. J. Baroczy. A systematic correlation for two-phase pressure drop. *Chem. Eng. Prog. Symp. Ser.*, 62(44):232–249, 1965.
- [12] D. R. H. Beattie. Two-phase flow structure and mixing length theory. *Nucl. Eng. Desing*, 21:46–64, 1972.
- [13] D. R. H. Beattie. A note on the calculation of two-phase pressure losses. *Nucl. Eng. Desing*, 25:395–402, 1973.

- [14] D. R. H. Beattie and P. B. Whalley. A simple two-phase frictional pressure drop calculation method. *Int. J. Multiphase Flow*, 8:83–87, 1982.
- [15] C. Ben-Salem and H. F. Ellouze. Pressure drop in annular horizontal two-phase flow. In G. P. Celata, P. di Marco, and R. K. Shah, editors, *Proceedings of the 2nd International Symposium on Two-Phase Flow Modelling and Experimentation*, volume 2, pages 1351–1355, Rome, Italy, 1999. Edizioni ETS, Pisa.
- [16] D. Biberg. An explicit equation for the wetted angle in two-phase stratified pipe flow. *Can. J. Chem. Eng.*, 77:1221–1224, 1999.
- [17] D. Biberg. Liquid wall friction in two-phase turbulent gas laminar liquid stratified flow. *Can. J. Chem. Eng.*, 77:1073–1082, 1999.
- [18] D. Biberg. Two-phase stratified pipe flow modelling: a new expression for the interfacial shear stress. In G. P. Celata, P. di Marco, and R. K. Shah, editors, *Proceedings of the 2nd International Symposium on Two-Phase Flow Modelling and Experimentation*, volume 2, pages 1–10, Rome, Italy, 1999. Edizioni ETS, Pisa.
- [19] G. Bigot. *Étude et conception de systèmes air/air inversables utilisant des mélanges à glissement de température*. PhD thesis, École de Mines de Paris, 2001.
- [20] J. A. Bouré. *Two-phase flows and heat transfer with application to nuclear design problems*. Hemisphere, New York, 1978.
- [21] R. S. Brodkey. *The phenomena of fluid motions*. Dover publications, New York, 1967.
- [22] Van P. Carey. *Liquid-vapor phase-change phenomena*. Taylor & Francis, Hebron, KY, 1992.
- [23] A. Cavallini, G. Censi, D. Del Gol, L. Doretto, G. A. Longo, and L. Rossetto. Experimental investigation on condensation heat transfer and pressure drop of new HFC refrigerants (R134a, R125, R32, R410A, R236ea) in a horizontal tube. *Int. J. Refrigeration*, 24:73–87, 2001.
- [24] A. Cavallini, D. Del Gol, L. Doretto, G. A. Longo, and L. Rossetto. Condensation pressure losses in smooth tubes. In E. W. P. Hahne, W. Heidemann, and K. Spindler, editors, *Proceedings of the 3rd European Thermal Sciences Conference*, volume 2, pages 927–932, Heidelberg, Germany, 2000. Edizioni ETS, Pisa.
- [25] G. P. Celata, K. Mishima, and G. Zummo. Critical heat flux prediction for saturated flow boiling of water in vertical tubes. *Int. J. Heat Mass Transfer*, 44:4323–4331, 2001.
- [26] S. D. Chang and S. T. Ro. Pressure drop of pure HFC refrigerants and their mixtures flowing in capillary tubes. *Int. J. Multiphase Flow*, 23(3):551–561, 1996.
- [27] J. M. Chawla. *Wärmeübergang and druckfall in waagerechten röhren bei der strömung von verdampfenden kältemitteln*, chapter Lg1-Lg2. 523. VDI-Forschungsh, 1967.
- [28] I. Y. Chen and K. Yang. Two-phase pressure drop of air-water in small horizontal tubes. *J. Thermophysics Heat Transfer*, 15(4):409–415, 2001.
- [29] I. Y. Chen, K. Yang, Y. Chang, and C. Wang. Two-phase pressure drop of air-water and R-410A in small horizontal tubes. *Int. J. Multiphase Flow*, 27:1293–1299, 2001.

- [30] J. J. J. Chen and P. L. Spedding. An extension of the Lockhart-Martinelli theory of two-phase pressure drop and holdup. *Int. J. Multiphase Flow*, 7:659–675, 1981.
- [31] D. Chisholm. Pressure gradients due to friction during the flow of evaporating two-phase mixtures in smooth tubes and channels. *Int. J. Heat Mass Transfer*, 16:347–358, 1973.
- [32] T. Y. Choi, Y. J. Kim, M. S. Kim, and S. T. Ro. Evaporation heat transfer of R-32, R-134a, R-32/134a and R-32/125/134a inside a horizontal smooth tube. *Int. J. Heat Mass Transfer*, 43:3651–3660, 2000.
- [33] G. Chupin, S. Labesque, P. Laux, and O.-J. Nydal. Air-oil-water pipe flow experiments at low liquid loading. In *Proceedings of the 40th ETPFG Meetings*, Stockholm, Sweeden, 2002.
- [34] A. Cicchitti, C. Lombardi, M. Silvestri, and G. Soldaini R. Zavattarelli. Two-phase cooling experiments - pressure drop, heat transfer and burnout measurements. *Energia Nucleare*, 7(6):407–425, 1960.
- [35] J. G. Collier and J. R. Thome. *Convective boiling and condensation*. Oxford University Press, Oxford, 1984.
- [36] M. K. Cooper. Saturated nucleate pool boiling: A simple correlation. In *1st U.K. National Conference on Heat Transfer, Vol.*, volume 2, pages 785–793, 1984. (I. Chem. E. Symposium Series N^o 86).
- [37] J. M. Delhaye. *Two-phase flows and heat transfer in the process industries*. Hemisphere, New York, 1990.
- [38] A. E. Dukler, Moye Wick III, and R. G. Cleveland. Frictional pressure drop in two-phase flow:b. an approach through similarity analysis. *AIChE Journal*, 10(1):44–51, 1964.
- [39] J. el Hajal, J. R. Thome, and A. Cavallini. Condensation in horizontal tubes, part 1: two-phase flow pattern map. *Int. J. Heat Mass Transfer*, 46:3349–3363, 2003.
- [40] J. el Hajal, J. R. Thome, and A. Cavallini. Condensation in horizontal tubes, part 2: new heat transfer model based on flow regimes. *Int. J. Heat Mass Transfer*, 46:3365–3387, 2003.
- [41] H. F. Ellouze. *Contribution à l'étude de la chute de pression en écoulement diphasique*. PhD thesis, Université Paris-Val de Marne(Paris XII), 1991.
- [42] Z. Fangde and L. Weidong. Interfacial shear stress and friction factor of stratified flow. In G. P. Celata, P. di Marco, and R. K. Shah, editors, *Proceedings of the 2nd International Symposium on Two-Phase Flow Modelling and Experimentation*, volume 2, pages 1263–1268, Rome, Italy, 1999. Edizioni ETS, Pisa.
- [43] L. B. Fore, S.G. Beus, and R. C. Bauer. Interfacial friction in gas-liquid annular flow: analogies to full and transition roughness. *Int. J. Multiphase Flow*, 26:1755–1769, 2000.
- [44] M. Fossa. A simple model to evaluate direct contact heat transfer and flow characteristics in annular two-phase flow. *Int. J. Heat Fluid Flow*, 16:272–279, 1995.
- [45] F. França and R. T. Lahey. The use of drift-flux techniques for the analysis of horizontal two-phase flows. *Int. J. Multiphase Flow*, 18:787–801, 1992.

- [46] L. Friedel. Improved friction drop correlations for horizontal and vertical two-phase pipe flow. In *European Two-phase Flow Group Meeting, paper E2*, Ispra, Italy, 1979.
- [47] L. Friedel. Pressure drop during gas/vapor-liquid flow in pipes. *Int. Chemical Engineering*, 20:352–367, 1980.
- [48] F. Fu and J. F. Klausner. A separated flow model for predicting two-phase pressure drop and evaporative heat transfer for vertical annular flow. *Int. J. Heat Fluid Flow*, 18:541–549, 1997.
- [49] L. Galbiati and P. Andreini. The transition between stratified and annular regimes for horizontal two-phase flow in small diameter tubes. *Int. Comm. Heat Mass Transfer*, 19:185–190, 1992.
- [50] E. N. Ganic and W. M. Rohsenow. On the mechanism of liquid drop deposition in two-phase dispersed flow. *J. Heat Transfer*, 101:288–294, 1979.
- [51] H. Gao, H.-Y. Gu, and L.-J. Guo. Numerical study of stratified oil-water two-phase turbulent flow in a horizontal tube. *Int. J. Heat Mass Transfer*, 46:749–754, 2003.
- [52] E. Grolman and M. H. Fortuin. Gas-liquid flow in slightly inclined pipes. *Chem. Eng. Sci.*, 52:4461–4471, 1997.
- [53] R. Gronnerud. Investigation of liquid hold-up, flow-resistance and heat transfer in circulation type of evaporators, part iv: two-phase flow resistance in boiling refrigerans. In *Annexe 1972-1, Bull. de l'Inst. du Froid*, 1979.
- [54] S. E. Haaland. Simple and explicit formulas for the friction factor in turbulent pipe flow. *J. Fluids Engineering*, 105:89–90, 1983.
- [55] P.J. Hamersma and J. Hart. A pressure drop correlation for gas/liquid pipe flow with a small liquid holdup. *Chem. Eng. Sci.*, 42(5):1187–1196, 1987.
- [56] N. P. Hand, P. L. Speeding, and S. J. Ralph. The effect of surface tension on flow pattern, holdup and pressure drop during horizontal air-water pipe flow at atmospheric conditions. *Chemical Engineering J.*, 48:197–210, 1992.
- [57] T. J. Hanratty and J. M. Engen. Interaction between a turbulent air stream and a moving water surface. *AIChE Journal*, 3:299–279, 1957.
- [58] J. Hart, P. J. Hamersma, and J. M. H. Fortuin. Correlations predicting frictional pressure drop and liquid holdup during horizontal gas-liquid pipe flow with a small liquid holdup. *Int. J. Multiphase Flow*, 15(6):947–964, 1989.
- [59] K. Hashizume. Flow pattern and void fraction of refrigerant two-phase flow in a horizontal pipe. *Bulletin of the JSME*, 26:1597–1602, 1983.
- [60] K. Hashizume. Flow pattern, void fraction and pressure drop of refrigerant two-phase flow in a horizontal pipe - I: Experimental data. *Int. J. Multiphase Flow*, 4(5):399–410, 1983.
- [61] K. Hashizume, H. Ogiwara, and H. Taniguchi. Flow pattern, void fraction and pressure drop of refrigerant two-phase flow in a horizontal pipe - II: Analysis of frictional pressure drop. *Int. J. Multiphase Flow*, 11:643–658, 1985.

- [62] W. H. Henstock and T. J. Hanratty. The interfacial drag and the height of the wall layer in annular flows. *AIChE Journal*, 22:990–1000, 1976.
- [63] G. Hetsroni, D. Mewes, C. Enke, M. Gurevich, and A. Mosyak R. Rozenblit. Heat transfer to two-phase flow in inclined tubes. *Int. J. Multiphase Flow*, 29:173–194, 2003.
- [64] G. F. Hewitt and A. H. Govan. Phenomenological modelling of non-equilibrium flows with phase change. *Int. J. Heat Mass Transfer*, 33:229–242, 1990.
- [65] E. T. Hurlburt and T. A. Newell. Prediction of the circumferential film thickness distribution in horizontal annular gas-liquid flow. *J. Fluids Engineering*, 122:396–402, 2000.
- [66] W. Idsinga, N. Todreas, and R. Bowring. An assessment of two-phase pressure drop correlation for steam-water systems. *Int. J. Multiphase Flow*, 3:401–413, 1977.
- [67] M. Ishii. *Thermo-fluid dynamics theory of two-phase flow*. Eyrolles, Paris, 1975.
- [68] T. Johannessen. A theoretical solution of the Lockhart-Martinelli flow model for calculating two-phase flow pressure and holdup. *Int. J. Heat Mass Transfer*, 15:1443–1449, 1972.
- [69] D. S. Jung, M. McLinden, R. Radermacher, and D. Didion. A study of flow boiling heat transfer with refrigerant mixtures. *Int. J. Heat Mass Transfer*, 32:1751–1764, 1989.
- [70] D. S. Jung and R. Radermacher. Prediction of pressure drop during horizontal annular flow boiling of pure and mixed refrigerants. *Int. J. Heat Mass Transfer*, 32(12):2435–2446, 1989.
- [71] D. Juric and G. Tryggvason. Computations of boiling flows. *Int. J. Multiphase Flow*, 24(3):387–410, 1998.
- [72] S. Kabelac and H.J. de Burg. Flow boiling of ammonia in a plain and a low finned horizontal tube. *Int. J. Refrigeration*, 24:41–50, 2001.
- [73] V. Kadambi. Void fraction and pressure drop in two-phase stratified flow. *Can. J. Chem. Eng.*, 59:584–589, 1981.
- [74] K. G. Kandlikar. Development of a flow boiling map for subcooled and saturated flow boiling of different fluids inside circular tubes. *J. Heat Transfer*, 113:190–200, 1991.
- [75] N. Kattan. *Contribution to the heat transfer analysis of substitute refrigerants in evaporator tubes with smooth or enhanced surfaces*. Thesis n 1498, Swiss Federal Institute of Technology Lausanne, 1996.
- [76] N. Kattan, J. R. Thome, and D. Favrat. Flow boiling in horizontal tubes: Part 1 - development of a diabatic two-phase flow pattern map. *J. Heat Transfer*, 120:140–147, 1998.
- [77] N. Kattan, J. R. Thome, and D. Favrat. Flow boiling in horizontal tubes: Part 2 - new heat transfer data for five refrigerants. *J. Heat Transfer*, 120:148–155, 1998.
- [78] N. Kattan, J. R. Thome, and D. Favrat. Flow boiling in horizontal tubes: Part 3 - development of a new heat transfer model based on flow pattern. *J. Heat Transfer*, 120:156–165, 1998.
- [79] D. Kim and A. J. Ghajar. Heat transfer measurements and correlations for air-water flow of different flow patterns in a horizontal pipe. *Exp. Thermal Fluid Sci.*, 25:659–676, 2002.

- [80] Y. Kim, K. Seo, and J. T. Chung. Evaporation heat transfer characteristics of R-410A in 7 and 9.52 mm smooth/microfin tubes. *Int. J. Refrigeration*, 25:716–730, 2002.
- [81] J. F. Klausner, B. T. Chao, and S. L. Soo. An improved method for simultaneous determination of frictional pressure drop and vapor volume fraction in vertical flow boiling. *Exp. Thermal Fluid Sci.*, 3:404–415, 1990.
- [82] E. Kordyban. Some details of developing slugs in horizontal two-phase flow. *AIChE Journal*, 31(3):802–806, 1985.
- [83] P. G. Kosky. Thin liquid films under simultaneous shear and gravity forces. *Int. J. Heat Mass Transfer*, 14:1220–1224, 1970.
- [84] J. E. Kowalski. Wall and interfacial shear stress in stratified flow in a pipe. *AIChE Journal*, 33(2):274–281, 1987.
- [85] S. S. Kutateladze. On the transition to film boiling under natural convection. *Kotloturbostronie*, 10(3), 1948.
- [86] M. Lallemand, C. Branescu, and P. Haberschill. Coefficients d'échange locaux au cours de l'ébullition du R22 et du R407C dans des tubes horizontaux, lisses ou micro-aileté. *Int. J. Refrigeration*, 24:57–72, 2001.
- [87] J. E. Laurinat, T. J. Hanratty, and J. C. Dallman. Pressure drop and film height measurements for annular gas-liquid flow. *Int. J. Multiphase Flow*, 10:341–356, 1984.
- [88] K.-W. Lee, S.-J. Baik, and T.-S. Ro. An utilization of liquid sublayer dryout mechanism in predicting critical heat flux under low pressure and low velocity conditions in round tubes. *Nuclear Engineering and Design*, 200:69–81, 2000.
- [89] P. Y. Lin and T. J. Hanratty. Detection of slug flow from pressure measurements. *Int. J. Multiphase Flow*, 13:13–21, 1987.
- [90] R. W. Lockhart and R. C. Martinelli. Proposed correlation of data for isothermal two-phase, two-component in pipes. *Chem. Eng. Process*, 45(1):39–48, 1949.
- [91] J. M. Mandhane, G. A. Gregory, and K. Aziz. A flow pattern map for gas-liquid flow in horizontal pipes. *Int. J. Multiphase Flow*, pages 537–553, 1974.
- [92] P. Melin. *Measurements and modelling of convective vaporization for refrigerants in a horizontal tube*. PhD thesis, Chalmers university of technology Göteborg, 1996.
- [93] J. Moreno-Quiben and J. R. Thome. Two-phase pressure drops in horizontal tubes: new results for R-410A and R-134a compared to R-22, paper IIC00. In 21st *IIR International Congress of Refrigeration*, Washington, D.C., USA, 2003.
- [94] H. Mori, S. Yoshida, K. Oshidi, and Y. Kakimoto. Dryout quality and post-dryout heat transfer coefficient in horizontal evaporator tubes. In E. W. P. Hahne, W. Heidermann, and K. Springler, editors, *Proceedings of the 3rd European Thermal Conference*. Edizioni ETS, Pisa, 2000.
- [95] A. Mosyak and G. Hetsroni. Analysis of dryout in horizontal and inclined tubes. *Int. J. Multiphase Flow*, 25:1521–1543, 1999.

- [96] A. A. Mouza, S. V. Paras, and A. J. Karabelas. CFD code application to wavy stratified gas-liquid flow. *Trans IChemE*, 79(Part A):561–568, 2001.
- [97] H. Müller-Steinhagen and K. Heck. A simple friction pressure correlation for two-phase flow in pipes. *Chem. Eng. Process*, 20:297–308, 1986.
- [98] C. H. Newton. *An experimental and numerical study of stratified gas-liquid flow in horizontal pipes*. PhD thesis, University of New South Wales (Australia), 1997.
- [99] C. H. Newton and M. Behnia. Estimation of wall shear stress in horizontal stratified gas-liquid pipe flow. *AIChE Journal*, 42(8):2369–2373, 1996.
- [100] C. H. Newton and M. Behnia. On the use of the stratified momentum balance for the deduction of shear stress in horizontal gas-liquid pipe flow. *Int. J. Multiphase Flow*, 24:1407–1423, 1998.
- [101] C. H. Newton and M. Behnia. Numerical calculation of turbulent stratified gas-liquid pipe flows. *Int. J. Multiphase Flow*, 26:327–337, 2000.
- [102] M. K. Nicholson, K. Aziz, and G. A. Gregory. Intermittent two-phase flow in horizontal pipes: Predictive methods. *Can. J. Chem. Eng.*, 56:653–663, 1978.
- [103] E. Nidegger, J. R. Thome, and D. Favrat. Flow boiling and pressure drop measurements for R-134a/Oil mixtures. part 1: Evaporation in a microfin tube. *HVAC&R Research*, 3(1):39–52, 1997.
- [104] Z. Olujić. Predicting two-phase flow friction loss in horizontal pipes. *Chem. Eng.*, June 24:45–50, 1985.
- [105] M. B. Ould-Didi, N. Kattan, and J. R. Thome. Prediction of two-phase gradients of refrigerants in horizontal tubes. *Int. J. Refrigeration*, 25:935–947, 2002.
- [106] S. V. Paras and A. J. Karabelas. Properties of the liquid layer in horizontal annular flow. *Int. J. Multiphase Flow*, 17:439–454, 1991.
- [107] B. Pierre. Flow resistance with boiling refrigerants - Part 1. *ASHRAE Journal*, 6(9):58–65, 1964.
- [108] W. M. Rohsenow. Post dryout heat transfer prediction. *Int. Comm. Heat Mass Transfer*, 15:559–569, 1988.
- [109] H. Ross, R. Radermacher, and M. di Marzo. Horizontal flow boiling of pure and mixed refrigerants. *Int. J. Heat Mass Transfer*, 30:979–992, 1987.
- [110] S. Z. Rouhani and E. Axelsson. Calculation of void volume fraction in the subcooled and quality boiling regions. *Int. J. Heat Mass Transfer*, 13:383–393, 1970.
- [111] T. W. F. Russel, A. W. Etchells, R. H. Jensen, and P. J. Arruda. Pressure drop and holdup in stratified gas-liquid flow. *AIChE Journal*, 20(4):664–669, 1974.
- [112] J. M. Saiz-Jabardo and E. P. Bandarra-Filho. Convective boiling of halocarbon refrigerants flowing in a horizontal copper tube - an experimental study. *Exp. Thermal Fluid Sci.*, 23:93–104, 2000.

- [113] P. K. Sarma, V. D. Rao, T. Subrahmanyam, S. Kakac, and H. T. Liu. A method to predict two-phase pressure drop using condensation heat transfer data. *Int. J. Therm. Sci.*, 39:184–190, 2000.
- [114] H. Schlichting. *Boundary layer theory*. McGraw-Hill, New York, 1980.
- [115] K. Seo and Y. Kim. Evaporation heat transfer and pressure drop of R-22 in 7 and 9.52 mm smooth/micro-fin tubes. *Int. J. Heat Mass Transfer*, 43:2869–2882, 2000.
- [116] K. Seo, Y. Kim, K.-J. Lee, and Y. Park. An experimental study on convective boiling of R-22 and R-410A in horizontal smooth and micro-fin tubes. *KSME International Journal*, 15(8):1156–1164, 2001.
- [117] M. M. Shah. A new correlation for heat transfer during boiling flow through pipes. *ASHRAE Transaction*, 82(Part 2), 1976.
- [118] O. Shoham and Y. Taitel. Stratified turbulent-turbulent gas-liquid flow in horizontal and inclined pipes. *AIChE Journal*, 30(3):377–385, 1984.
- [119] T. N. Smith and R. W. F. Tait. Interfacial shear stress and momentum transfer in horizontal gas-liquid flow. *Chem. Eng. Sci.*, 21:63–75, 1966.
- [120] H. M. Soliman. On the annular-to-wavy flow pattern transition during condensation inside horizontal tubes. *Int. J. Heat Mass Transfer*, 60:475–481, 1982.
- [121] P. L. Spedding. Prediction in stratified gas-liquid co-current flow in horizontal pipes. *Int. J. Heat Mass Transfer*, 40(8):1923–1935, 1997.
- [122] D. Steiner. *VDI-Wärmeatlas (VDI Heat Atlas)*, chapter Hbb. Verein Deutscher Ingenieure VDI-Gesellschaft Verfahrenstechnik und Chemieingenieurwesen (GCV), Düsseldorf, 1993.
- [123] K. Stephan and M. Abdelsalam. Heat-transfer correlations for natural convection boiling. *Int. J. Heat Mass Transfer*, 23:73–87, 1980.
- [124] N. D. Sylvester and J. P. Brill. Drag reduction in two-phase annular-mist flow of air and water. *AIChE Journal*, 22(3):615–617, 1976.
- [125] Y. Taitel and A. E. Dukler. A model for predicting flow regime transitions in horizontal and near horizontal gas-liquid flow. *AIChE Journal*, 22:47–55, 1976.
- [126] Y. Taitel and A. E. Dukler. A theoretical approach to the Lockhart-Martinelli correlation for stratified flow. *Int. J. Multiphase Flow*, 2:591–595, 1976.
- [127] T. N. Tandon, H. K. Varma, and Gupta C. P. A void fraction model for annular two-phase flow. *Int. J. Heat Mass Transfer*, 28:191–198, 1985.
- [128] John R. Taylor. *An introduction to error analysis. The study of uncertainties in physical measurements*. University Science Books, Sausalito, CA, second edition, 1997.
- [129] J. R. S. Thom. Prediction of pressure drop during forced circulation boiling of water. *Int. J. Heat Mass Transfer*, 7:709–724, 1964.
- [130] J. R. Thome. On recent advances in modelling of two-phase flow and heat transfer. In *Proceedings of the 1st International Conference on Heat Transfer, Fluid Mechanics and Thermodynamics*, Kruger Park, South Africa, 2002.

- [131] J. R. Thome and J. el Hajal. Two-phase flow pattern map for evaporation in horizontal tubes: latest version. In *Proceedings of the 1st International Conference on Heat Transfer, Fluid Mechanics and Thermodynamics*, Kruger Park, South Africa, 2002.
- [132] J. R. Thome and J. El Hajal. Flow boiling heat transfer to carbon dioxide: general prediction method. *Int. J. Refrigeration*, 27:294–301, 2004.
- [133] T. N. Tran, M. Chyu, M. W. Wambsganss, and D. M. France. Two-phase pressure drop of refrigerants during flow boiling in small channels: an experimental investigation and correlation development. *Int. J. Multiphase Flow*, 26:1739–1754, 2000.
- [134] C. Tribbe and H. M. Müller-Steinhagen. An evaluation of the performance of phenomenological models for predicting models for predicting pressure gradient during gas-liquid flow in horizontal pipelines. *Int. J. Multiphase Flow*, 26:1019–1036, 2000.
- [135] C. P. Tso and S. Sugawara. Film thickness prediction in a horizontal annular two-phase flow. *Int. J. Multiphase Flow*, 16:867–884, 1990.
- [136] T. Ursenbacher, L. Wojtan, and J. R. Thome. Interfacial measurements in stratified types of flow. Part I: Measurements for R22 and R-410A. *Int. J. Multiphase Flow*, 30:125–137, 2004.
- [137] VDI. *VDI-Wärmeatlas (VDI Heat Atlas)*. Verein Deutscher Ingenieure VDI-Gesellschaft Verfahrenstechnik und Chemieingenieurwesen (GCV), Düsseldorf, 1993.
- [138] P. K. Vijayan, A. P. Patil, D. S. Pillhwal, D. Saha, and V. Venkat-Raj. An assessment of pressure drop and void fraction correlations with data from two-phase natural circulation loops. *Heat Mass Transfer*, 36:541–548, 2000.
- [139] N. A. Vlachos, S. V. Paras, and A. J. Karabelas. Liquid-to-wall shear stress distribution in stratified/atomization flow. *Int. J. Multiphase Flow*, 23(5):845–863, 1997.
- [140] N. A. Vlachos, S. V. Paras, and A. J. Karabelas. Prediction of holdup, axial pressure gradient and wall shear stress in wavy stratified and stratified/atomization gas/liquid flow. *Int. J. Multiphase Flow*, 25:365–376, 1999.
- [141] G. B. Wallis. Annular two-phase flow. part 1: A simple theory. *J. Basic Engineering*, pages 59–72, 1970.
- [142] M. W. Wambsganss, J. A. Jendrzeczyk, and D. M. France. Two-phase flow patterns and transitions in a small, horizontal, rectangular channel. *Int. J. Multiphase Flow*, 17:327–342, 1991.
- [143] C. Wang and C. Chiang. Two-phase heat transfer characteristics for R-22/R-407C in a 6.5-mm smooth tube. *Int. J. Heat Fluid Flow*, 18:550–558, 1997.
- [144] C. Wang, C. Chiang, and D. Lu. Visual observation of two-phase flow pattern of R-22, R-134a and R-407C in a 6.5-mm smooth tube. *Exp. Thermal Fluid Sci.*, 15:395–405, 1997.
- [145] C. Wang, C. Chiang, and J. Yu. An experimental study of in-tube evaporation of R-22 inside a 6.5-mm smooth tube. *Int. J. Heat Fluid Flow*, 19:259–269, 1998.
- [146] C.-C. Wang, S.-K. Chiang, Y.-J. Chang, and T.-W. Chung. Two-phase flow resistance of refrigerants R-22, R-410A and R-407C in small diameter tubes. *Trans. IChemE*, 79:553–560, 2001.

- [147] C.-C. Wang, J.-G. Yu, S.-P. Lin, and D.-C. Lu. An experimental study of convective boiling of refrigerants R-22 and R-410A. *ASHRAE Trans*, 104:1144–1150, 1998.
- [148] Z. Wang, K. S. Gabriel, and D. L. Manz. The influences of wave height on the interfacial friction in annular gas-liquid flow under normal and microgravity conditions. *Int. J. Multiphase Flow*, 30:1193–1211, 2004.
- [149] J. Weisman, D. Duncan, J. Gibson, and T. Crawford. Effects of fluid properties and pipe diameter on two-phase flow patterns in horizontal lines. *Int. J. Multiphase Flow*, 5:437–462, 1979.
- [150] P. B. Whalley. *Two-phase flow and heat transfer*. Oxford University Press, Oxford, 1996.
- [151] H. Wijaya and M. W. Spatz. Two-phase flow heat transfer and pressure drop characteristics of R-22 and R-32/125. *ASHRAE Trans*, 101:1020–1027, 1995.
- [152] M. J. Wilson, T. A. Newell, J. C. Chato, and C. A. Infante Ferreira. Refrigerant charge, pressure drop, and condensation heat transfer in flattened tubes. *Int. J. Multiphase Flow*, 26:442–451, 2003.
- [153] L. Wojtan. *Experimental and analytical investigation of void fraction and heat transfer during evaporation in horizontal tubes*. Thesis n 2978, Swiss Federal Institute of Technology Lausanne, 2004.
- [154] L. Wojtan, T. Ursenbacher, and J. R. Thome. Interfacial measurements in stratified types of flow. Part II: Measurements for R22 and R-410A. *Int. J. Multiphase Flow*, 30:125–137, 2004.
- [155] L. Wojtan, T. Ursenbacher, and J. R. Thome. Investigation of flow boiling in horizontal tubes: Part I - A new diabatic two-phase flow pattern map. *Int. J. Heat Mass Transfer*, 48:2955–2969, 2005.
- [156] L. Wojtan, T. Ursenbacher, and J. R. Thome. Investigation of flow boiling in horizontal tubes: Part II - Development of a new heat transfer model for stratified-wavy, dryout and mist flow regimes. *Int. J. Heat Mass Transfer*, 48:2970–2985, 2005.
- [157] S. Wongwises, T. Wongchang, and J. Kaewon. A visual study of two-phase flow patterns of HFC-134a and lubricant oil mixtures. *Heat Transfer Eng.*, 23:13–22, 2002.
- [158] C. Yang and C. Shieh. Flow pattern of air-water and two-phase R-134a in small circular tubes. *Int. J. Multiphase Flow*, 27:1163–1177, 2001.
- [159] M. Yu, T. Lin, and C. Tseng. Heat transfer and flow pattern during two-phase flow boiling of R-134a in horizontal smooth and microfin tubes. *Int. J. Refrigeration*, 25:789–798, 2002.
- [160] W. Yu, D. M. France, M. W. Wanbsganss, and J. R. Hull. Two-phase pressure drop, boiling heat transfer and critical heat flux in a small-diameter tube. *Int. J. Multiphase Flow*, 28:927–941, 2002.
- [161] M. Zhang and R. L. Webb. Correlation of two-phase friction for refrigerants in small-diameter tubes. *Exp. Thermal Fluid Sci.*, 25:131–139, 2001.
- [162] O. Zürcher. *Contribution to the heat transfer analysis of natural and substitute refrigerants evaporated in a smooth horizontal tube*. Thesis n 2122, Swiss Federal Institute of Technology Lausanne, 2000.

- [163] O. Zürcher, D. Favrat, and J. R. Thome. Development of a diabatic two-phase flow pattern map for horizontal flow boiling. *Int. J. Heat Mass Transfer*, 45:291–301, 2002.
- [164] O. Zürcher, J. R. Thome, and D. Favrat. Flow boiling and pressure drop measurements for R-134a/Oil mixtures. part 1: Evaporation in a plain tube. *HVAC&R Research*, 3(1):54–64, 1977.
- [165] O. Zürcher, J. R. Thome, and D. Favrat. Evaporation of ammonia in a smooth horizontal tube: heat transfer measurement and predictions. *J. Heat Transfer*, 121:89–101, 1999.
- [166] O. Zürcher, J. R. Thome, and D. Favrat. An onset of nucleate boiling criterion for horizontal flow boiling. *Int. J. Therm. Sci.*, 39:909–918, 2000.

Nomenclature

Latin

Symbol	Description	Units
A	Cross Section Area	m^2
A_L	Cross Section Area of Liquid Phase	m^2
A_{LD}	Non-dimensional Area of Liquid Phase - $[A_L/D]$	-
A_G	Cross Section Area of Vapor Phase	m^2
A_{GD}	Non-dimensional Area of Vapor Phase - $[A_V/D]$	-
C	Empirical Constant	-
c_{pL}	Liquid Specific Heat	J/kgK
c_{pG}	Vapor Specific Heat	J/kgK
c_{pw}	Heating Water Specific Heat	J/kgK
d	Vapor Core Diameter	m
D	Internal Tube Diameter	m
D_{ext}	External Tube Diameter	m
D_h	Hydraulic Diameter	m
f_L	Liquid Friction Factor	-
f_G	Vapor Friction Factor	-
Fr_L	Liquid Froude Number	-
g	Acceleration of Gravity	m/s^2
G	Mass Velocity	kg/m^2s
h_L	Liquid Height in the Tube	m
h_{LD}	Non-dimensional Liquid Height in the Tube - $[h_L/D]$	-
h_L	Liquid Enthalpy	J/kg
h_{LV}	Latent Heat of Vaporisation	J/kg
h_w	Enthalpy of the Heating Water per Unit of Mass	J/kg
j	Total Superficial Velocity	m/s
j_L	Liquid Superficial Velocity	m/s
j_{Lj}	Liquid Drift Flux	m/s
j_{LG}	Liquid Drift Flux Relative to Vapor	m/s
j_G	Vapor Superficial Velocity	m/s
L	Characteristic Length	m
M	Molecular Weight	g/mol
\dot{M}	Total Mass Flow Rate	kg/s
\dot{M}_L	Liquid Mass Flow Rate	kg/s
\dot{M}_G	Liquid Mass Flow Rate	kg/s

\dot{M}_{ref}	Refrigerant Mass Flow Rate	kg/s
P	Pressure	bar
P	Preheater Power	W
P_i	Liquid Interface	m
P_{iD}	Non-dimensional Liquid Interface - $[P_i/D]$	-
P_{local}	Saturation Pressure on the Local Heat Transfer Measurement Position	bar
P_L	Wetted Perimeter	m
P_{LD}	Non-dimensional Wetted Perimeter - $[P_L/D]$	-
P_{sat}	Saturation Pressure	bar
P_G	Dry Perimeter	m
P_{GD}	Non-dimensional Dry Perimeter - $[P_V/D]$	-
q	Heat Flux	W/m^2
q_{crit}	Critical Heat Flux	W/m^2
q_{ext}	External Heat Flux	W/m^2
\dot{Q}_L	Liquid Volumetric Flow Rate	m^3/s
\dot{Q}_G	Vapor Volumetric Flow Rate	m^3/s
R	Internal Tube Radius	m
Re	Reynolds Number	-
Re_H	Homogeneous Reynolds Number	-
Re_L	Reynolds Number in Liquid Phase	-
Re_G	Reynolds Number in Vapor Phase	-
Re_δ	Reynolds Number in Liquid Film	-
t	Time	s
T	Temperature	K
T_{sat}	Saturation Temperature	K
T_{wall}	Wall Temperature	K
u_L	Mean Velocity of Liquid Phase	m/s
u_G	Mean Velocity of Vapor Phase	m/s
We_L	Liquid Weber Number	-
x	Vapor Quality	-
x_{de}	Dryout Completion Quality	-
x_{di}	Dryout Inception Quality	-
x_e	Equilibrium Vapor Quality	-
x_{IA}	Vapor Quality at Intermittent-Annular Flow Transition	-
X_{tt}	Martinelli Parameter	-

Greek

Symbol	Description	Units
δ	Liquid Film Thickness	m
ϵ	Cross-Sectional Void Fraction	-
θ_{dry}	Dry Angle	rad
θ_{strat}	Stratified Angle	rad
μ_L	Dynamic Viscosity of Liquid	$Pa \cdot s$
μ_G	Dynamic Viscosity of Liquid	$Pa \cdot s$
ρ_L	Density of Liquid	kg/m^3
ρ_G	Density of Vapor	kg/m^3
σ	Surface Tension	N/m
τ	Shear stress	N/m^2

Curriculum Vitae

PERSONAL DATA

Name: **Jesús MORENO QUIBÉN**

Date of Birth: 08.12.1970

Birthplace: Madrid - Spain

Nationality: Spanish

EDUCATION

Engineering Diploma in Aeronautics. Universidad Politécnica de Madrid, Spain.

DEA "Dynamique des fluides et des transferts", Université Pierre et Marie Curie, Paris VI, France.

CAREER

CEMAGREF, Génie des procédés frigorifiques (GPAN), Anthony, France

GROUPE DANONE, Centre International de Recherche Daniel Carasso (Danone Vitapole), Le Plessis Robinson, France

EPFL, École Polytechnique Fédérale de Lausanne, Laboratoire de Transfert de Chaleur et de Masse (LTCM), Lausanne, Switzerland.